

AD-A161 251

THEORETICAL STUDY OF SINGLE AND MULTIPLE SCATTERING BY
CYLINDERS(U) PANAMETRICS INC WALTHAM MASS
N E PEDERSEN ET AL. APR 85 CRDC-CR-85014

1/1

UNCLASSIFIED

DARK11-83-C-0044

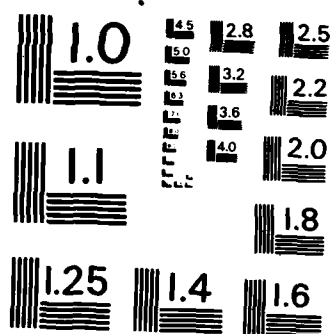
F/G 20/8

NL

END

FORM 1

1000



MICROCOPY RESOLUTION TEST CHART
NATIONAL BUREAU OF STANDARDS-1963-A

AD-A161 251

①

CRDC-CR-85014

**FINAL REPORT ON THEORETICAL STUDY
OF SINGLE AND MULTIPLE SCATTERING
BY CYLINDERS**

by **Norman E. Pedersen
Jeanne C. Pedersen
Peter C. Waterman**
PANAMETRICS, INC.

Waltham, Massachusetts 02154

ORIGINAL FILE COPY

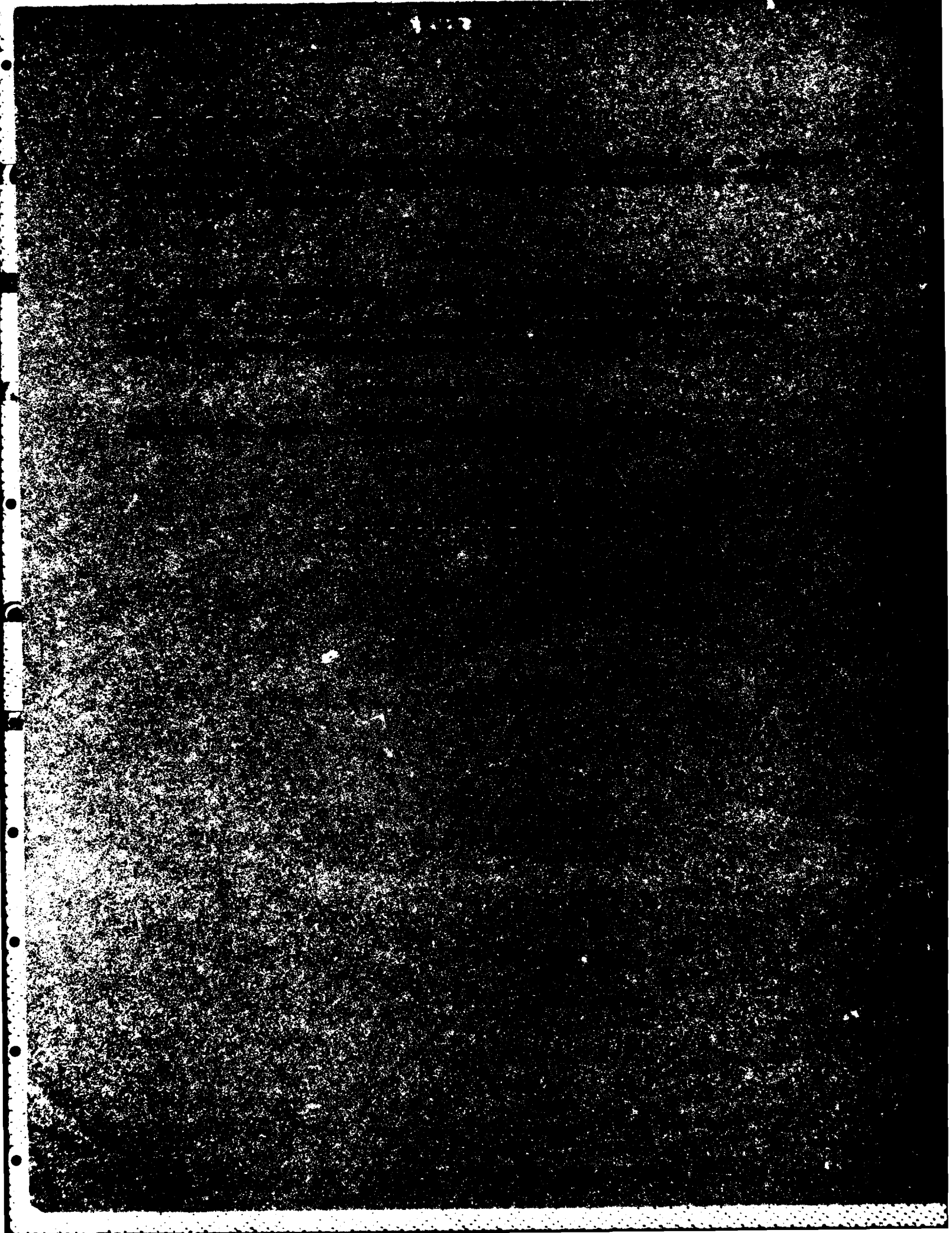
DTIC
ELECTE
NOV 14 1985
B

April 1986

**US Army Armament, Munitions & Chemical Command
Aberdeen Proving Ground, Maryland 21010-5423**

DISTRIBUTION STATEMENT
Approved for public release
Distribution Unlimited

85 523 281



UNCLASSIFIED

SECURITY CLASSIFICATION OF THIS PAGE

REPORT DOCUMENTATION PAGE				
1a REPORT SECURITY CLASSIFICATION UNCLASSIFIED		1b. RESTRICTIVE MARKINGS		
2a SECURITY CLASSIFICATION AUTHORITY		3 DISTRIBUTION/AVAILABILITY OF REPORT Approved for public release; distribution unlimited.		
2b DECLASSIFICATION/DOWNGRADING SCHEDULE				
4 PERFORMING ORGANIZATION REPORT NUMBER(S) CR-85014		5 MONITORING ORGANIZATION REPORT NUMBER(S)		
6a NAME OF PERFORMING ORGANIZATION Panametrics, Inc.		6b OFFICE SYMBOL (If applicable)		7a. NAME OF MONITORING ORGANIZATION
6c ADDRESS (City, State, and ZIP Code) 221 Crescent Street Waltham, Massachusetts		7b ADDRESS (City, State, and ZIP Code)		
8a. NAME OF FUNDING/SPONSORING ORGANIZATION US Army Chemical R & D Center		8b. OFFICE SYMBOL (If applicable) SMCCR-RSP-B		9. PROCUREMENT INSTRUMENT IDENTIFICATION NUMBER DAAK 11-83-C-0044
8c ADDRESS (City, State, and ZIP Code) Aberdeen Proving Ground, MD 21010-5423		10 SOURCE OF FUNDING NUMBERS		
		PROGRAM ELEMENT NO.	PROJECT NO.	TASK NO. WORK UNIT ACCESSION NO.
11 TITLE (Include Security Classification) Final Report on Theoretical Study of Single and Multiple Scattering by Cylinders				
12 PERSONAL AUTHOR(S) Pedersen, Norman E; Pedersen, Jeanne C.; and Waterman, Peter C.				
13a TYPE OF REPORT Contract		13b TIME COVERED FROM May 83 to May 84		14 DATE OF REPORT (Year, Month, Day) 1985 April
15. PAGE COUNT 90				
16 SUPPLEMENTARY NOTATION COR: Robert H. Frickel, SMCCR-RSP-B, (301) 671-3854				
17 COSATI CODES			18 SUBJECT TERMS (Continue on reverse if necessary and identify by block number) Electromagnetic scattering, Radiative transfer, Conductive fibers, Particle clouds	
FIELD	GROUP	SUB-GROUP		
15	02			
19 ABSTRACT (Continue on reverse if necessary and identify by block number) Closed form analytic results are obtained for the calculation of the electromagnetic differential and total scattering, absorption, and extinction cross sections of arbitrarily oriented conductive fibers. An extensive computer program has been developed for the computation of these quantities. The results agree with expectations for arbitrary conductivity, arbitrary length-to-wavelength ratio and radius-to-wavelength ratio less than 0.3. Two minor exceptions are noted and discussed. The albedo of the particle is computed as are the appropriately averaged differential scattering cross sections. These quantities serve as inputs to a Radiative Transfer computer program which was developed concurrently to calculate and plot the angular distributions of reflected and transmitted radiation from large aggregates of the particles.				
20 DISTRIBUTION/AVAILABILITY OF ABSTRACT <input checked="" type="checkbox"/> UNCLASSIFIED/UNLIMITED <input type="checkbox"/> SAME AS RPT. <input type="checkbox"/> DTIC USERS			21. ABSTRACT SECURITY CLASSIFICATION UNCLASSIFIED	
22a NAME OF RESPONSIBLE INDIVIDUAL Brenda C. Eckstein			22b TELEPHONE (Include Area Code) (301) 671-2914	
			22c. OFFICE SYMBOL SMCCR-SPS-IR	

DD FORM 1473, 84 MAR

83 APR edition may be used until exhausted.

All other editions are obsolete.

SECURITY CLASSIFICATION OF THIS PAGE

UNCLASSIFIED

85 5 28 281

PREFACE

The work described in this report was authorized under Contract No. DAAK 11-83-C-0044. This work was started in May 1983 and completed in May 1984.

The use of trade names in this report does not constitute an official endorsement or approval of the use of such commercial hardware or software. This report may not be cited for purposes of advertisement.

Reproduction of this document in whole or in part is prohibited except with permission of the Commander, US Army Chemical Research and Development Center, ATTN: SMCCR-SPS-IR, Aberdeen Proving Ground, Maryland 21010-5423. However, the Defense Technical Information Center and the National Technical Information Service are authorized to reproduce the document for United States government purposes.

This document has been approved for release to the general public.

RE: Classified References, Distribution Unlimited.
Delete the classified references on Page 89 per Mr. Timothy Hampton, Army Chemical R & D Ctr., Attn: SMCCR-SPS-IR

Accession	
NTIS	
DTIC	
Doc	
Dist	
By	
Dist	
Availability	
Dist	
Special	
A-1	



CONTENTS

	<u>Page</u>
1. INTRODUCTION AND SUMMARY	7
2. ELECTROMAGNETIC PROPERTIES OF CONDUCTIVE FIBERS	8
2.1 Basic Theory	8
3. RESULTS	18
3.1 Differential Scattering Cross Section	19
3.1.1 Behavior as a Function of kh	19
3.1.2 Behavior as a Function of θ_i	24
3.2 Backscatter Cross Sections	27
3.2.1 Radar Cross Section vs. Aspect Angle	27
3.2.2 Backscatter Cross Section vs. kh	30
3.3 Very Large Values of kh	39
3.3.1 Averaged Extinction, Absorption, and Scattering Cross Sections vs. Wavelength	51
3.4 Discussion	56
4. RADIATIVE TRANSFER IN CONDUCTIVE FIBER CLOUDS	61
4.1 Basic Theory	61
4.2 The Phase Function	64
4.3 Orientation Averages	67
4.4 The Thin-layer Limit	70
4.5 Numerical Results	73
REFERENCES	89

FINAL REPORT ON THEORETICAL STUDY
OF SINGLE AND MULTIPLE SCATTERING BY CYLINDERS

1. INTRODUCTION AND SUMMARY

In this report we present theoretical results obtained in the subject contract in the areas of single scattering and absorption of electromagnetic radiation by arbitrarily oriented conductive fibers, and in radiative transfer by large aggregates of such fibers.

It has been determined that, in the case of single scattering and absorption, the theory in its present form is capable of producing reliable results over a very wide range of length-to-wavelength ratio. An asymptotic expression is given for the backscatter cross section in the large length-to-wavelength ratio limit. In the small (Rayleigh) limit, it is shown that a previous theory by two of the authors is in agreement with the more complex present theory. Two classes of cases have been identified in which the present theory is in error. In practical computations, these cases can be easily avoided without substantial loss of information.

The detailed differential scattering cross sections have been appropriately averaged for input to the Radiative Transfer computer program. Representative results are presented in this report. The program has been tested in various limits including isotropic scattering over a wide range of optical depths. These results were found to be in excellent agreement with published values.

2. ELECTROMAGNETIC PROPERTIES OF CONDUCTIVE FIBERS

Basic Theory.

This theory is based upon a variational procedure first set forth by Tai for perfectly conducting wires,¹ and later extended to the case of finite conductivity by Cassedy and Fainberg, who, however, considered only broadside incidence.² In the present theory, scattering, absorption, extinction, and radar cross sections are calculated for arbitrary angles of incidence. The results can then be averaged over all angles of incidence to obtain results for a cloud of randomly oriented particles.

Consider a plane electromagnetic wave incident upon a cylindrical wire of finite conductivity at arbitrary angle of incidence, θ_i , and arbitrary polarization angle, ψ , as shown in Fig. 1. Assuming the wire is sufficiently thin for the current to be radially symmetric, one may consider the current as a current filament $I(z)$ along the axis. Since the wire is assumed to be thin, only the component of the electric field parallel to the axis will stimulate a response, and the integral equation for the boundary condition at the cylinder surface may be written

$$E_0 \sin \theta_i \cos \psi e^{jkz \cos \theta_i} = I(z)Z + \frac{1}{2\pi} \int_0^{2\pi} \frac{j\eta k}{4\pi} \int_{-h}^h I(z') \left(1 + \frac{\partial^2}{k^2 \partial z'^2} \right) \frac{e^{-jkR}}{R} dz' d\phi' \quad (1)$$

Here, Z is the skin impedance per unit length of the cylinder, relating H_θ to E_z , and is given by³

$$Z = \frac{g}{2\pi a(\sigma + j\omega\epsilon)} \left(\frac{I_0(ga)}{I_1(ga)} \right) \quad (2)$$

where

$$g^2 = \omega^2 [(\mu_0 \epsilon_0 \cos^2 \theta_i - \mu\epsilon) + \frac{j\mu\sigma}{\omega}] \quad (3)$$

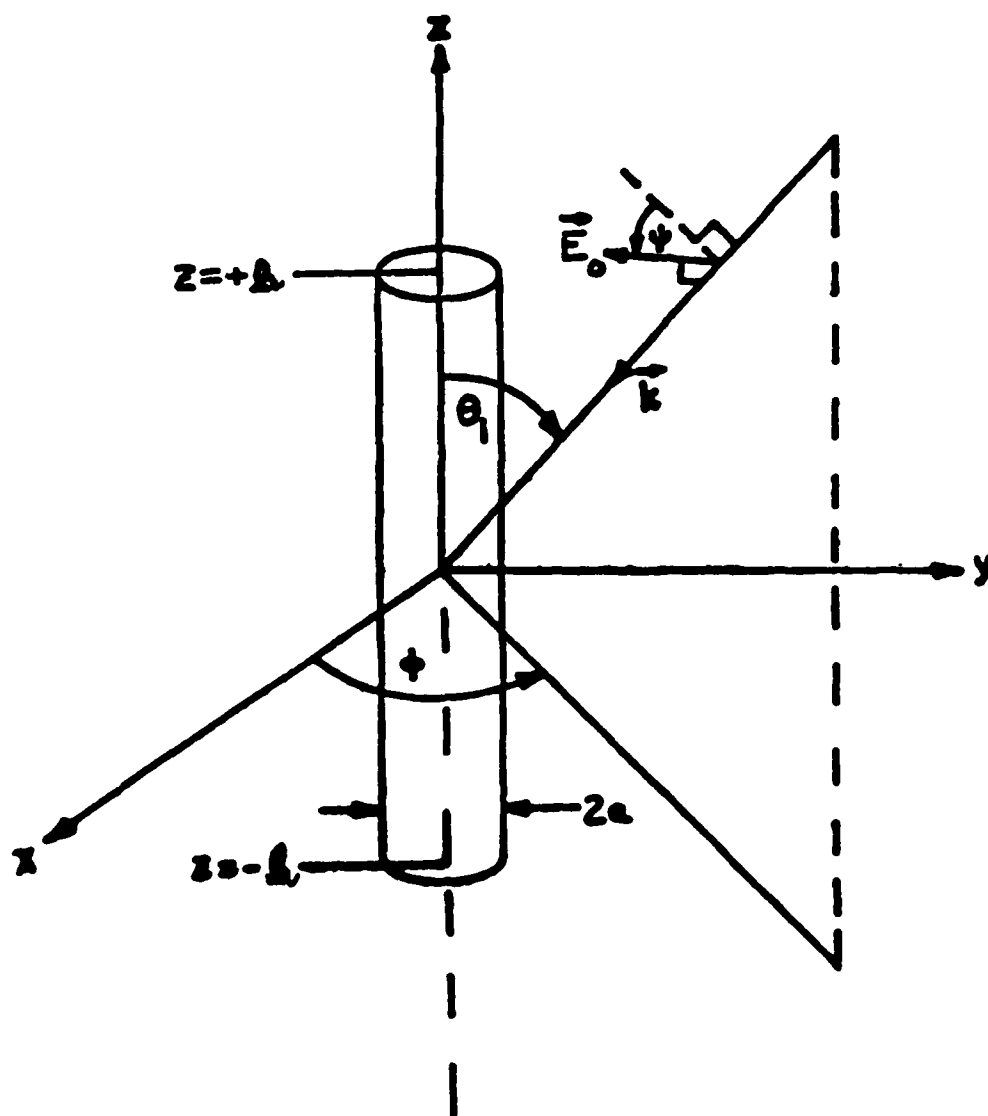


Figure 1. Geometry of the Cylindrical Wire With Respect to the Propagation Vector k , and the Electric Field Vector, E . θ_1 is the Angle Between k and the z Axis; ψ is the Angle E Makes With the k - z Plane.

$I_0(ga)$ and $I_1(ga)$ are modified Bessel functions. It may be noted that the real part of g^2 may become important in the visible region. In Eq. (1)

$\eta = \mu_0/\epsilon_0$ is the characteristic impedance of free space, and

$$R = \sqrt{(z-z')^2 + 4a^2 \sin^2 \left(\frac{\phi - \phi'}{2} \right)}$$

A stationary homogeneous functional expression can now be constructed for the current in terms of the backscattered amplitude S , giving

$$\frac{1}{S} = \frac{\frac{k}{2\pi} \int_0^{2\pi} d\phi \int_{-h}^h \int_{-h}^h I(z)I(z') \left(1 + \frac{\partial^2}{k^2 \partial z'^2} \right) \frac{e^{-jkR}}{R} dz' dz - \frac{4\pi jZ}{\eta} \int_{-h}^h I^2(z) dz}{\left[k \sin \theta_i \int_{-h}^h I(z) e^{jkz \cos \theta_i} dz \right]^2} \quad (4)$$

For the current function we employ a series of harmonic terms, i.e.,

$$I(z) = I_0 \sum_{n=1}^N \left\{ A_n f_{cn}(z) + B_n f_{sn}(z) \right\} \quad (5)$$

Here

$$f_{cn}(z) = \cos nkz \cos nqx - \cos nx \cos nqkz \quad (6)$$

and

$$f_{sn}(z) = \sin nkz \sin nqx - \sin nx \sin nqkz, \quad (7)$$

where $q = \cos \theta_i$ and $x = kh$, h being the cylinder half-length. This current function is summed over the number of terms appropriate for the ratio of cylinder length to wavelength of interest, generally $N \gtrsim 2h/\lambda$. For $n = 1$, the current function becomes identical to that used originally by Tai¹ and Pedersen⁴. Note that both f_{cn} (the even functions) and f_{sn} (the odd functions) vanish at $z = \pm h$, which is appropriate if the current is to be zero at the ends of the fiber.

When the current function is substituted into Eq. 4, the following expression results:

$$\begin{aligned} \frac{1}{S} = & \sum_{n=1}^N \left\{ A_n^2 (\gamma_{cn} - \lambda_{cn}) + A_n B_n (\gamma_{csn} - \lambda_{csn}) + B_n^2 (\gamma_{sn} - \lambda_{sn}) \right. \\ & + \sum_{\substack{m=1 \\ m \neq n}}^N \left[A_n A_m (\gamma_{cnm} - \lambda_{cnm}) + A_n B_m (\gamma_{cnsn} - \lambda_{cnsn}) + A_m B_n (\gamma_{snm} - \lambda_{snm}) \right. \\ & \left. \left. + B_n B_m (\gamma_{snm} - \lambda_{snm}) \right] \right\} / \left[\sum_{n=1}^N (A_n g_{cn} + B_n g_{sn}) \right]^2. \end{aligned} \quad (8)$$

Here the terminology of g 's, λ 's, and γ 's follows the previous terminology of Tai¹, Cassedy and Fainberg², and Pedersen⁴ and is as follows:

$$g_c = k \sin \theta_i \int_{-h}^h f_c(z) e^{jkz \cos \theta_i} dz \quad (9)$$

$$g_s = k \sin \theta_i \int_{-h}^h f_s(z) e^{jkz \cos \theta_i} dz \quad (10)$$

$$\lambda_c = \frac{4\pi j Z}{\eta} \int_{-h}^h f_c^2(z) dz \quad (11)$$

$$\lambda_s = \frac{4\pi j Z}{\eta} \int_{-h}^h f_s^2(z) dz \quad (12)$$

$$\lambda_{cnm} = \frac{4\pi j Z}{\eta} \int_{-h}^h f_{cn}(z) f_{cm}(z) dz \quad (13)$$

$$\lambda_{snm} = \frac{4\pi j Z}{\eta} \int_{-h}^h f_{sn}(z) f_{sm}(z) dz \quad (14)$$

$$\lambda_{cnsn} = \frac{4\pi j Z}{\eta} \int_{-h}^h f_{cn}(z) f_{sn}(z) dz \quad (15)$$

$$\gamma_c = \frac{k}{2\pi} \int_0^{2\pi} d\phi \int_{-h}^h \int_{-h}^h f_c(z) f_c(z') \left(1 + \frac{1}{k^2} \frac{\partial^2}{\partial z'^2}\right) \frac{e^{-jkR}}{R} dz dz' \quad (16)$$

$$\gamma_s = \frac{k}{2\pi} \int_0^{2\pi} d\phi \int_{-h}^h \int_{-h}^h f_s(z) f_s(z') \left(1 + \frac{1}{k^2} \frac{\partial^2}{\partial z'^2}\right) \frac{e^{-jkR}}{R} dz dz' \quad (17)$$

$$\gamma_{cnm} = \frac{k}{2\pi} \int_0^{2\pi} d\phi \int_{-h}^h \int_{-h}^h f_{cn}(z) f_{cm}(z') \left(1 + \frac{1}{k^2} \frac{\partial^2}{\partial z'^2}\right) \frac{e^{-jkR}}{R} dz dz' \quad (18)$$

$$\gamma_{snm} = \frac{k}{2\pi} \int_0^{2\pi} d\phi \int_{-h}^h \int_{-h}^h f_{sn}(z) f_{sm}(z') \left(1 + \frac{1}{k^2} \frac{\partial^2}{\partial z'^2}\right) \frac{e^{-jkR}}{R} dz dz' \quad (19)$$

$$\gamma_{cmsn} = \frac{k}{2\pi} \int_0^{2\pi} d\phi \int_{-h}^h \int_{-h}^h f_{cm}(z) f_{sn}(z') \left(1 + \frac{1}{k^2} \frac{\partial^2}{\partial z'^2}\right) \frac{e^{-jkR}}{R} dz dz' \quad (20)$$

In the preceding equations, $f_{cn}(z)$ and $f_{sn}(z)$ are given by Eqs. (6) and (7).

Either by odd function considerations or by more elaborate mathematical arguments it can be shown that the integrals of Eqs. (15) and (20) are identically zero. The remaining integrals have been evaluated in closed form, and the results listed in an earlier report.⁴

After simplification, Eq. (8) becomes

$$\frac{1}{S} = \sum_{n=1}^N \left\{ A_n^2 (\gamma_{cn} - \lambda_{cn}) + B_n^2 (\gamma_{sn} - \lambda_{sn}) + \sum_{\substack{m=1 \\ m \neq n}}^N \left[A_n A_m (\gamma_{cnm} - \lambda_{cnm}) + B_n B_m (\gamma_{snm} - \lambda_{snm}) \right] \right\} / \left[\sum_{n=1}^N (A_n^2 g_{cn} + B_n^2 g_{sn}) \right]^2 \quad (21)$$

By the variational technique, the constants A_n and B_n may now be evaluated by setting

$$\frac{\partial}{\partial A_n} \left(\frac{1}{S} \right) = 0 \quad (22)$$

and

$$\frac{\partial}{\partial B_n} \left(\frac{1}{S} \right) = 0 \quad (23)$$

Equation (22) then yields

$$\begin{aligned} \sum_{n=1}^N \left\{ (A_n g_{cn} + B_n g_{sn}) \left[(\gamma_{cn} - \lambda_{cn}) + \sum_{\substack{m=1 \\ m \neq n}}^N A_m (\gamma_{cnm} - \lambda_{cnm}) \right] \right. \\ \left. - 2g_{cn} \left[A_n (\gamma_{cn} - \lambda_{cn}) + B_n (\gamma_{sn} - \lambda_{sn}) + \sum_{\substack{m=1 \\ m \neq n}}^N (A_n A_m (\gamma_{cnm} - \lambda_{cnm}) \right. \right. \right. \\ \left. \left. \left. + B_n B_m (\gamma_{snm} - \lambda_{snm}) \right) \right] \right\} = 0 \end{aligned} \quad (24)$$

while Equation (23) yields

$$\begin{aligned} \sum_{n=1}^N \left\{ (A_n g_{cn} + B_n g_{sn}) \left[(\gamma_{sn} - \lambda_{sn}) + \sum_{\substack{m=1 \\ m \neq n}}^N B_m (\gamma_{snm} - \lambda_{snm}) \right] \right. \\ \left. - 2g_{sn} \left[A_n (\gamma_{cn} - \lambda_{cn}) + B_n (\gamma_{sn} - \lambda_{sn}) + \sum_{\substack{m=1 \\ m \neq n}}^N (A_n A_m (\gamma_{cnm} - \lambda_{cnm}) \right. \right. \right. \\ \left. \left. \left. + B_n B_m (\gamma_{snm} - \lambda_{snm}) \right) \right] \right\} = 0 \end{aligned} \quad (25)$$

Equations (24) and (25) are non-linear and, therefore, it is extremely difficult to solve for the A_n 's and B_n 's. To avoid the non-linearity of Eqs. (24) and (25), the following procedure was used. By multiplying each term in Eq. (1) by

$$\int_{-h}^h f_{sm}(z) dz,$$

where $f_{cm}(z) dz$, is given by Eq. (6), we obtain

$$\left(\frac{E_o \cos \psi}{I_o} \right) g_{cm} = \frac{jnk}{4\pi} \sum_{n=1}^N A_n (\gamma_{cnm} - \lambda_{cnm}) \quad (26)$$

Similarly, by multiplying each term in Eq. (1) by

$$\int_{-h}^h f_{cm}(z) dz,$$

where $f_{sm}(z)$ is given by equation (7), we obtain

$$\left(\frac{E_o \cos \psi}{I_o} \right) g_{sm} = \frac{jnk}{4\pi} \sum_{n=1}^N B_n (\gamma_{snm} - \lambda_{snm}) \quad (27)$$

Since g_{cm} is real and g_{sm} is imaginary, while γ_{cnm} , γ_{snm} , λ_{cnm} , and λ_{snm} are complex, Eqs. (26) and (27) can be rewritten in the following set of four linear equations.

$$\begin{aligned} - \left(\frac{4\pi E_o \cos \psi}{nk I_o} \right) g_{cm} = & \sum_{n=1}^N \{ \text{Re}(A_n) \cdot \text{Im}(\gamma_{cnm} - \lambda_{cnm}) \\ & + \text{Im}(A_n) \cdot \text{Re}(\gamma_{cnm} - \lambda_{cnm}) \} \end{aligned} \quad (28)$$

$$0 = \sum_{n=1}^N [\text{Re}(A_n) \cdot \text{Re}(\gamma_{cnm} - \lambda_{cnm}) - \text{Im}(A_n) \cdot \text{Im}(\gamma_{cnm} - \lambda_{cnm})] \quad (29)$$

$$\begin{aligned} \left(\frac{4\pi E_o \cos \psi}{nk I_o} \right) |g_{sm}| = & \sum_{n=1}^N [\text{Re}(B_n) \cdot \text{Re}(\gamma_{snm} - \lambda_{snm}) \\ & - \text{Im}(B_n) \cdot \text{Im}(\gamma_{snm} - \lambda_{snm})] \end{aligned} \quad (30)$$

and

$$0 = \sum_{n=1}^N [\text{Re}(B_n) \cdot \text{Im}(\gamma_{snm} - \lambda_{snm}) - \text{Im}(B_n) \cdot \text{Re}(\gamma_{snm} - \lambda_{snm})] \quad (31)$$

If Eq. (5) accurately represents the current in the cylinder, then for a given length cylinder, there should be a value of N for which the values of the A_n 's and B_n 's converge as more terms are taken. Eqs. (28-31) were programmed for broadside incidence, but showed no convergence for even the smallest values of cylinder length. It was, therefore, concluded that the series formulation (Eq. 5) is not an appropriate form for the current function.

Next, a single value of n was chosen so that $n = \text{Integer } (kh + 1)$. Curves for differential cross section and back-scatter cross section were computed and plotted for large values of kh . These graphs showed an unrealistic number of resonances in the differential cross-section and the back-scatter graph did not agree with existing data. It was, therefore, decided to re-examine the simpler current function of Tai where $n = 1$, using the impedance Eq. (2).

When $n = 1$, Eq. (5) becomes

$$I = I_0 [f_c(z) + A f_s(z)]$$

where

$$f_c(z) = \cos kz \cos qx - \cos x \cos qkz$$

and

$$f_s(z) = \sin kz \sin qx - \sin x \sin qkz .$$

By means of the variational technique, A is determined to be

$$A = \frac{g_s (\gamma_c - \lambda_c)}{g_c (\gamma_s - \lambda_s)} \quad (35)$$

where g_c , g_s , λ_c , λ_s , γ_c and γ_s are given by Eqs. (9), (10), (11), (12), (16) and (17), respectively with $n = 1$. Having determined A , the general far field scattered amplitude can be written as

$$\begin{aligned}
S(\theta, \theta_i) = & 2\sqrt{1-p^2} \left\{ \frac{g_c}{(\gamma_c - \lambda_c)} \left[\frac{\cos q x}{(1 - p^2)} (\sin x \cos px - p \cos x \sin px) \right. \right. \\
& - \left. \frac{\cos x}{(q^2 - p^2)} (q \sin q x \cos px - p \cos x \sin px) \right\} \\
& + j \frac{g_s}{(\gamma_s - \lambda_s)} \left\{ \frac{\sin qx}{(1 - p^2)} (p \sin x \cos px - \cos x \sin px) \right. \\
& - \left. \frac{\sin x}{(q^2 - p^2)} (p \sin qx \cos px - q \cos qx \sin px) \right\} \quad (36)
\end{aligned}$$

where $p = \cos \theta$, θ being the scattering angle.

By definition, the differential scattering cross section is then given as

$$\begin{aligned}
\sigma(\theta, \theta_i) &= R_o^2 \left| \frac{E_{S0}}{E_o} \right|^2 \\
&= \frac{1}{k^2} \left| S(\theta, \theta_i) \right|^2. \quad (37)
\end{aligned}$$

The total scattering cross section

$$\sigma_s = \frac{2\pi}{k^2} \int_0^\pi \left| S(\theta, \theta_i) \right|^2 \sin \theta d\theta. \quad (38)$$

The extinction cross section is defined by the well-known forward amplitude theorem as

$$\sigma_s = \frac{4\pi}{k^2} \operatorname{Im} [S(\pi - \theta_i, \theta_i)] \quad (39)$$

The absorption cross section is just the rms power absorbed in the scatterer divided by the rms intensity of the incident beam. The rms power absorbed in the wire is given by

$$P_a = \operatorname{Re}(Z) \int_{-h}^h |I(z)|^2 dz$$

and the rms intensity of the θ component of the incident beam is

$$I_\theta = \frac{E_o^2}{2\eta}$$

so that the absorption cross section is given by

$$\sigma_a = \frac{2\eta \operatorname{Re}(Z)}{E_o^2} \int_{-h}^h |I(z)|^2 dz. \quad (40)$$

Finally, the radar cross section is defined to be

$$\begin{aligned} \sigma_{\text{RCS}} &= 4\pi \sigma(\theta_i, \theta_i) \\ &= \frac{4\pi}{k^2} |S(\theta_i, \theta_i)|^2 \end{aligned} \quad (41)$$

Equations (37-41) are for polarization in the k - Z plane, e.g. $\psi = 0^\circ$.

The results achieved by using the above equations with $n = 1$ will be discussed in the following section. It appears at this time that this theory may be valid for kh values much larger than 50.

3. RESULTS

As discussed in the preceding section, the use of a Fourier series representation (Eqs. 5, 6, 7) for the current function resulted in the lack of convergence of the series. Considerable effort was expended in the analysis and this result was, of course, disappointing.

After having determined that the above non-convergence property exists, it was decided that the $n = 1$ term of the current function, e.g., Eqs. (32), (33), and (34), would be utilized in conjunction with the surface impedance function of Wait given by Eq. (2). These expressions were substituted in Eq. (4), and the variational technique, Eq. (22), with $B_n = A$ was utilized to obtain the differential scattering, orientation averaged extinction, scattering, and absorption cross sections, as well as the radar cross section.

The objective of this analysis was to determine the range of parameters over which the simplified current function could be utilized. Questions to be answered were:

- (a) Over what range of kh is the theory useful?
- (b) In the limit of very large kh , do the differential scattering patterns give reasonable results?
- (c) Assuming that the theory is well behaved in the $kh \gg 1$ limit, can one obtain simplified asymptotic expressions for the various cross sections?
- (d) How do these asymptotic expressions compare with those which can be obtained from infinite length cylinder calculations?
- (e) Do the results agree with Rayleigh theory in the appropriate limit?

In the remainder of this Section, we present results which demonstrate good asymptotic behavior in the large kh limit, as well as good quantitative agreement with published experimental data and with Rayleigh theory.

3.1 Differential Scattering Cross Section.

In this sub-section we present computed curves of differential scattering cross section per square wavelength (σ_{diff}/λ^2) as a function of scattering angle θ . It is important to note (see Fig. 1) that the scattering angle is measured with respect to the cylinder axis, as is the angle of incidence θ_i . In all cases, the electric field is in the plane of the incident k vector and the cylinder axis.

In Figs. 2 through 9, the incident wavelength is 3.14 mm and the cylinder radius is 3.0 micron ($ka = 6 \times 10^{-3}$). The electrical conductivity is 3×10^4 mho/m. These parameters are representative of graphite fibers illuminated by a 3 mm plane wave.

3.1.1 Behavior as a Function of kh .

Figures 2, 3, 4 and 5 show the behavior of the scattering pattern for three values of kh , where h = half length. In Fig. 2, $kh = 1$. This particle should, therefore, scatter like a simple dipole and we see from the figure that this is indeed so. Note that, even though $\theta_i = 30^\circ$, the scattering displays a single broad lobe which is symmetric and has a maximum at 90° , which is perpendicular to the axis.

In Fig. 3, the length has been increased from 1 mm to 5 mm, corresponding to $kh = 5$. We see that, in this case, the scattering pattern is more complicated. We still see a little bit of the symmetric (dipole-like) scattering at 90° . This is in the intermediate range of kh . The pattern is largely symmetric, with the major lobe appearing in the vicinity of $180^\circ - \theta_i = 150^\circ$.

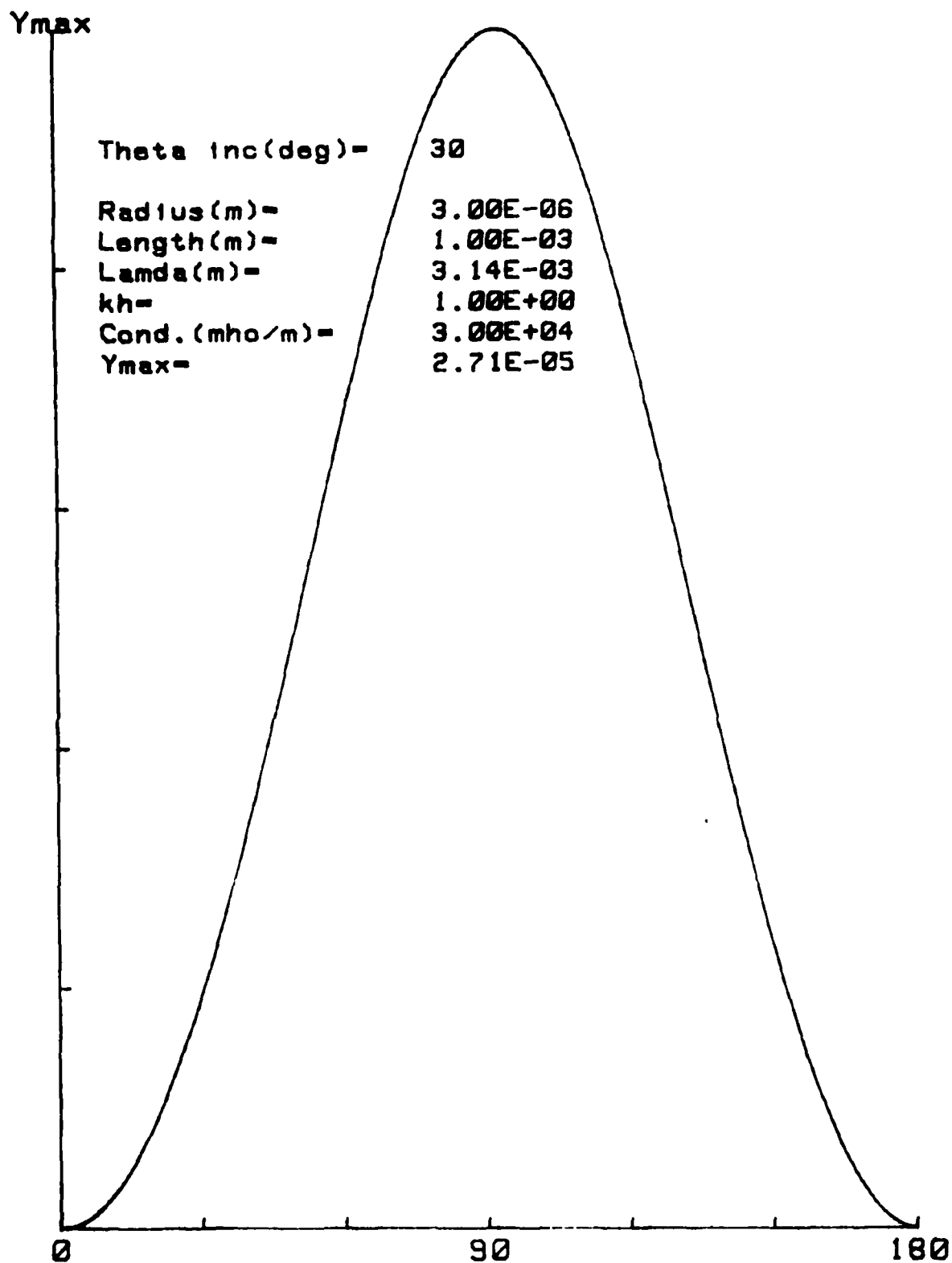


Figure 2. Differential Cross Section/ Lamda^2 for $\theta_i = 30^\circ$;
 $kh = 1$

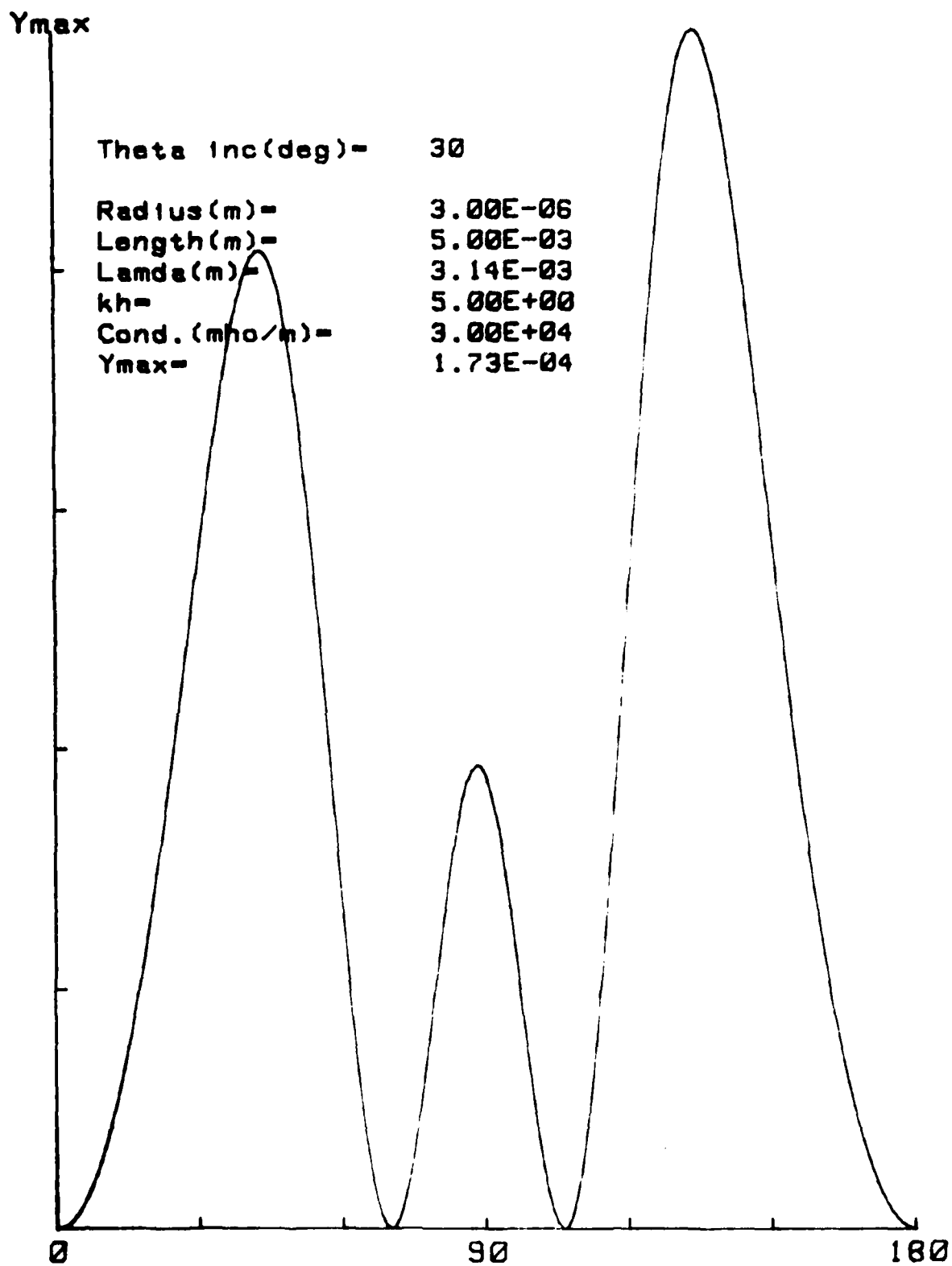


Figure 3. Differential Cross Section/Lambda² for $\theta_i = 30^\circ$;
kh = 5

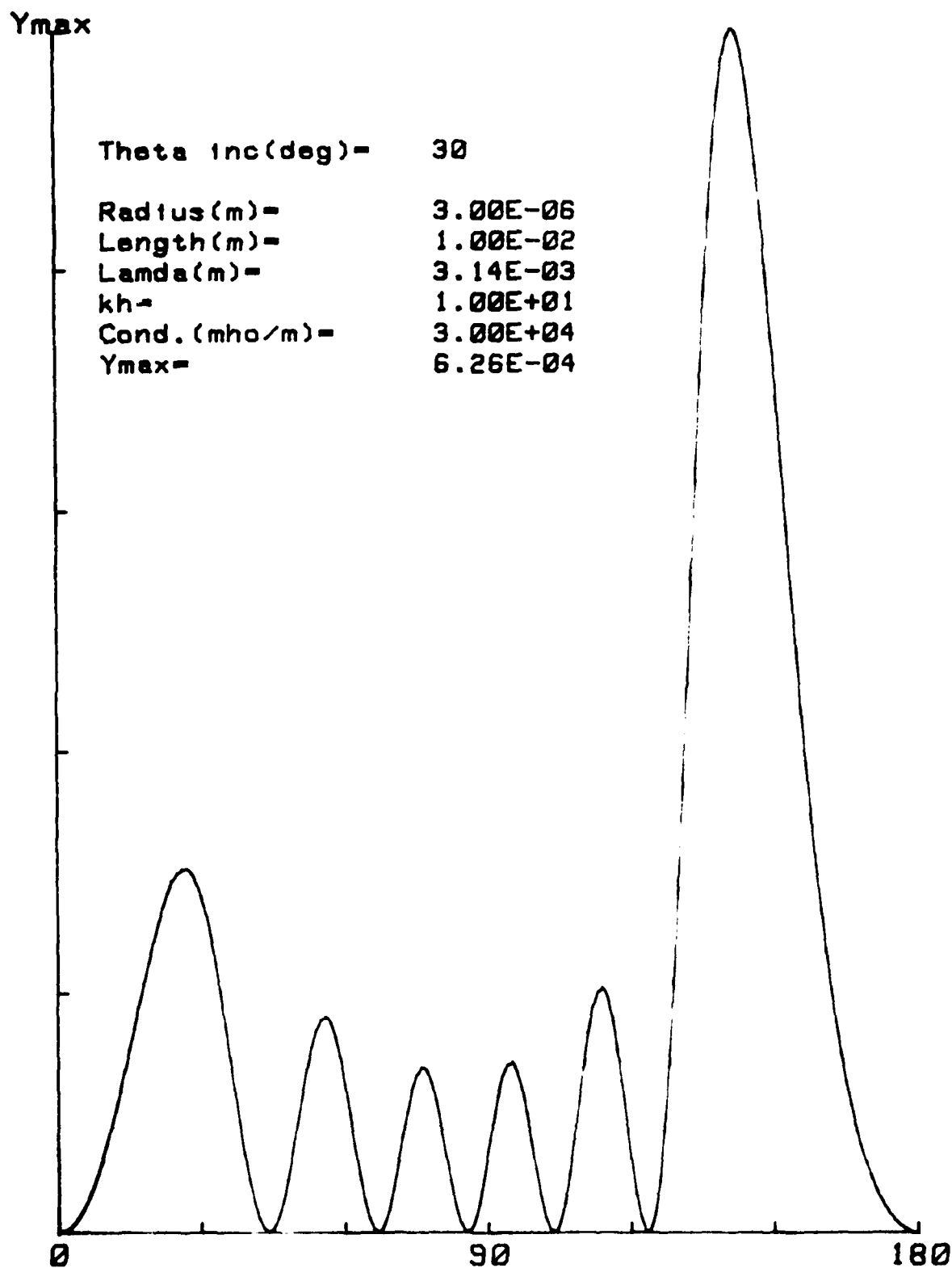


Figure 4. Differential Cross Section/ λ^2 for $\theta_i = 30^\circ$;
 $kh = 10$

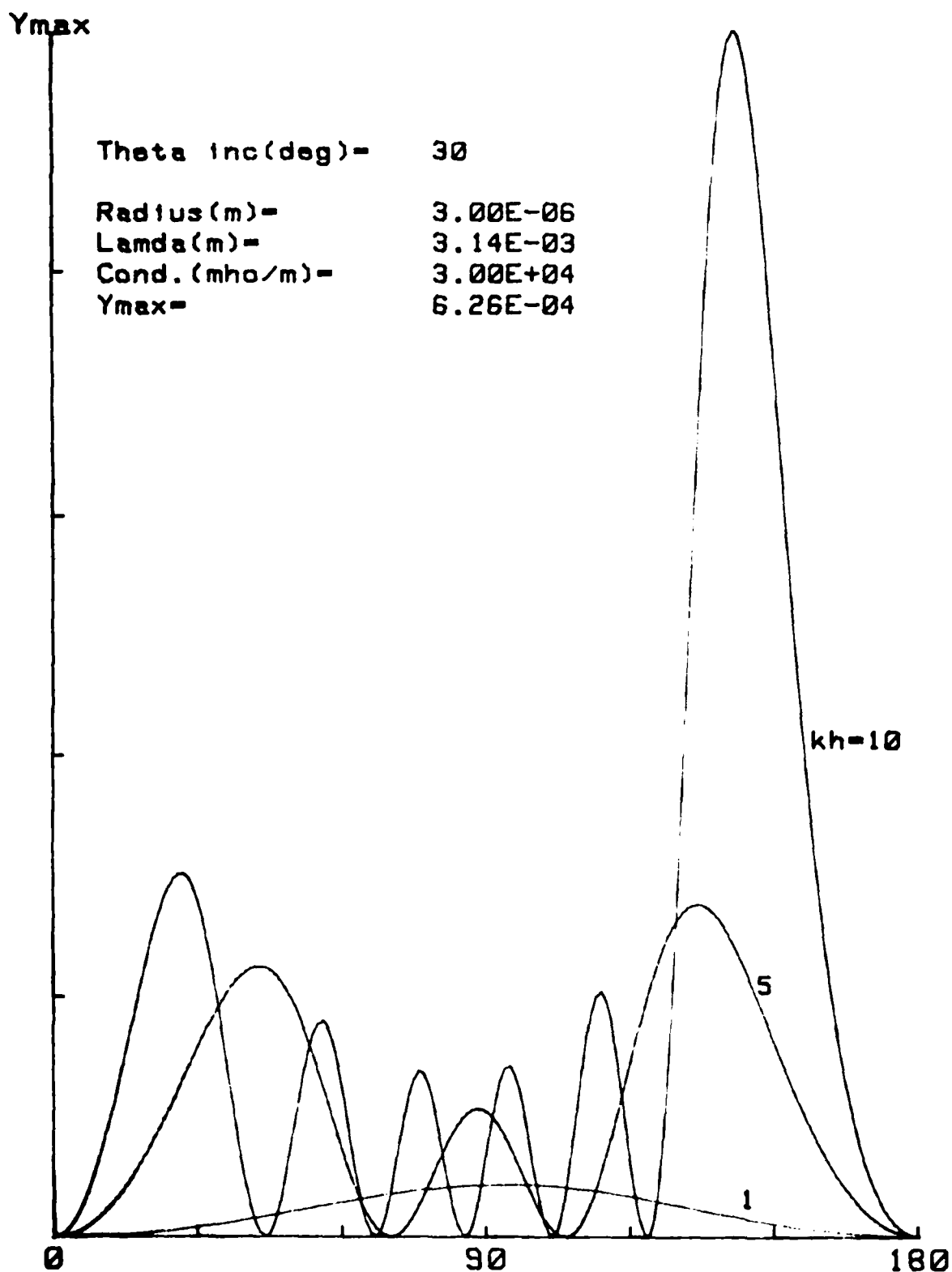


Figure 5. Composite Differential Cross Section/ λ^2 for $kh = 1, 5, 10$ and $\theta_i = 30^\circ$

Note that, in the case of $kh \gg 1$, the scattering amplitude is constant in the axisymmetric cones whose included half angle is θ , the differential scattering angle of the figures. Therefore, the differential scattering cross section at $\theta = 180^\circ - \theta_i$ is the same as that at $\theta = 180^\circ + \theta_i$. But, this latter scattering angle is the direction of the incident k vector, and therefore, is the forward scattering direction. It is well known that, for large kh , we should expect to find a major lobe in the forward direction. Therefore, the lobe at $\theta \approx 150^\circ$ qualitatively agrees with what we would intuitively expect for a moderately large value of kh and small ka .

If we next increase the length so that $kh = 10$ (a value well into the $kh \gg 1$ region), we see in Fig. 4 that the major lobe of Fig. 3 develops into a much more pronounced peak in the vicinity of $\theta \approx 150^\circ$. This shows that the forward ($\theta = 180^\circ + \theta_i$) and specular ($\theta = 180^\circ - \theta_i$) scattering patterns are fairly well developed.

Figure 5 is a composite of Figs. 2, 3, and 4, with all data shown in correct numerical scale. It is interesting to note that the peak for $kh = 10$ is closer to 150° than that for $kh = 5$, which is in agreement with our expectations.

3.1.2 Behavior as a Function of θ_i .

In the next set of Figs. (6 through 9), we fix kh at a value of $kh = 5$ and choose three angles of incidence: $\theta_i = 30^\circ$, 60° , and 90° .

The scattering pattern of Fig. 6, for which $\theta_i = 30^\circ$, is that of Fig. 3 and is repeated for continuity. We see in Fig. 7 that, when θ_i is increased to 60° , the major lobe shifts to $\theta \approx 180^\circ - 60^\circ = 120^\circ$, which is just what we should expect.

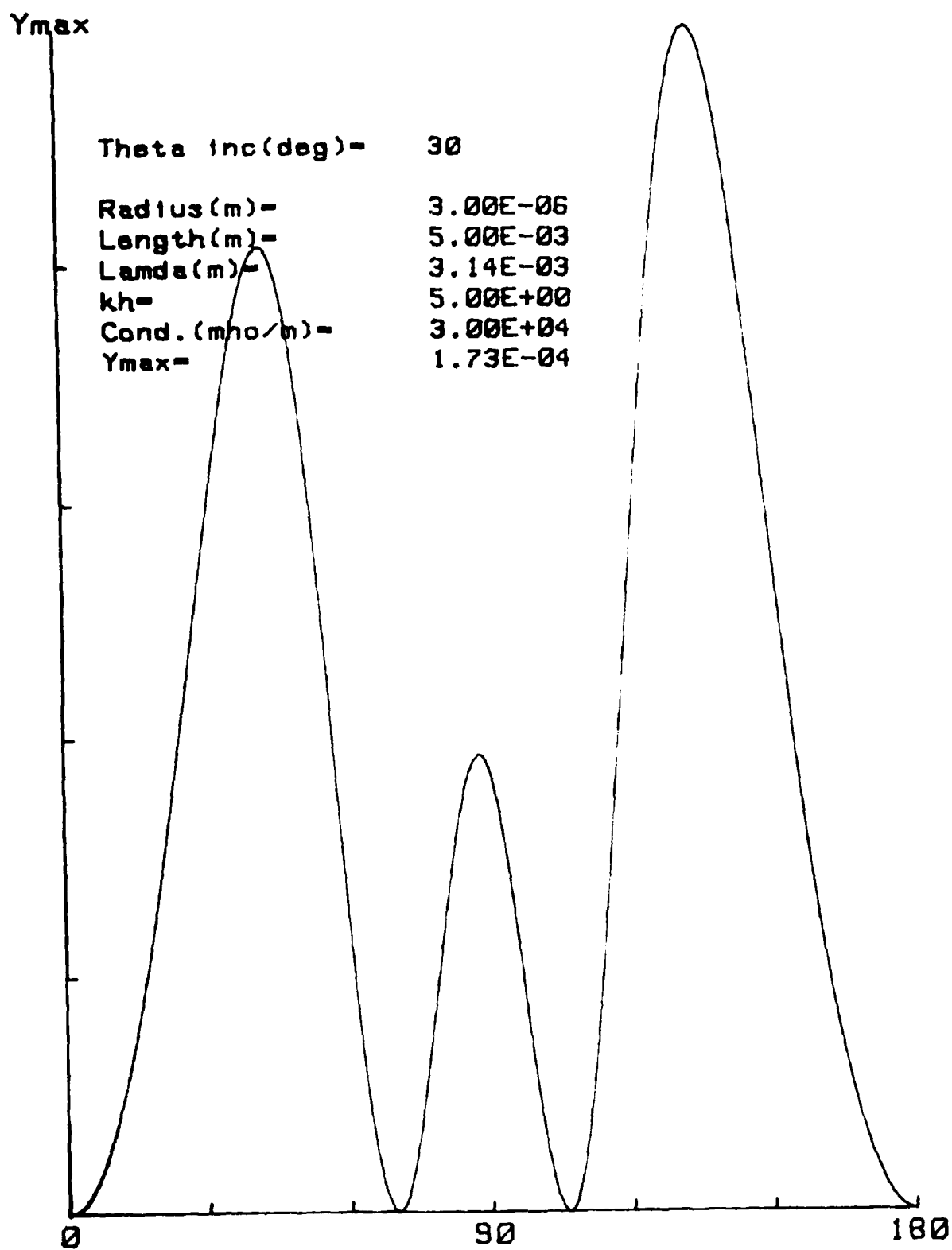


Figure 6. Differential Cross Section/Lambda² for kh = 5; $\theta_i = 30^\circ$

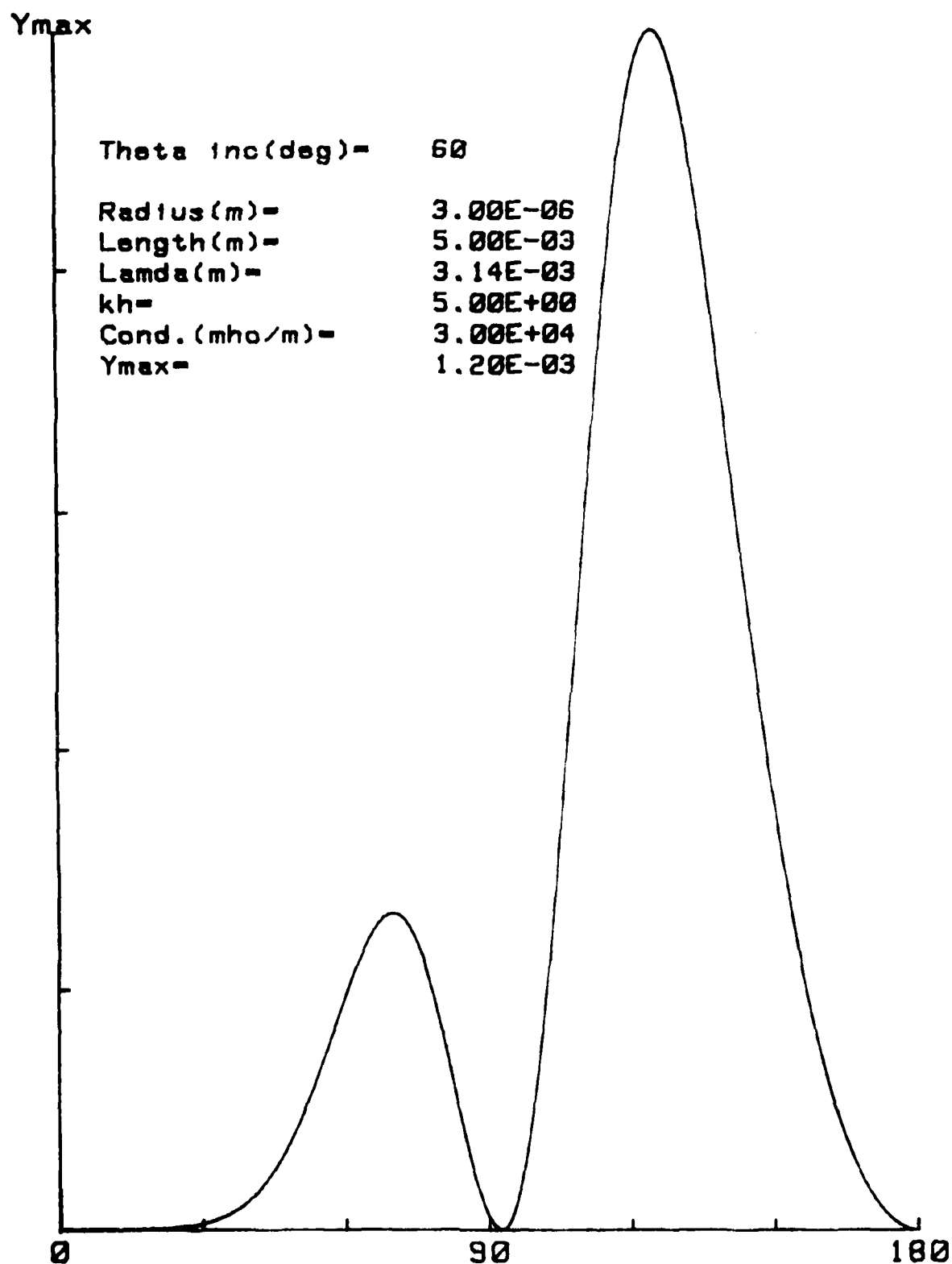


Figure 7. Differential Cross Section/ Lambda^2 for $kh = 5$; $\theta_i = 60^\circ$

At $\theta_i = 90^\circ$ (Fig. 8), we have broadside incidence and the major lobe has shifted to 90° as expected. The pattern is symmetrical about 90° as it should be.

A composite of the preceding three curves is shown in Fig. 9, which demonstrates how significantly the magnitudes of the scattering cross sections differ as a function of angle of incidence.

3.2 Backscatter Cross Sections.

We have made a number of comparisons between the results of the present theory and available measurements. The data presented in this section are limited to moderate values of $kh \leq 10$. It is unfortunate that more experimental data are not available. In particular, we have found no experimental data for lossy cylinders. Available experimental data with which we can compare appears to be limited to the backscatter cross sections of perfectly conducting, but thin ($ka < 1$) wires. Notwithstanding, considerable insight can be gained in the foregoing comparisons.

3.2.1 Radar Cross Section vs. Aspect Angle.

In this sub-section we compare the results of the present theory with experimental data taken at Lockheed Georgia⁵ for tungsten wires in the resonance region. The measurement frequency was 9.375 GHz. Wire diameters ranged from 1 to 3 mils. The skin depth of tungsten is 0.04 mils at this frequency and we can, therefore, consider the conductivity to be infinite for Figs. 10 through 16. In these Figures, the solid curves are our theoretical results and the dotted curves are experimental data. These Figures are plots of backscatter cross section per square wavelength vs. aspect angle with the E vector and the cylinder axis in the rotational plane. Note that 90° and 270° represent broadside incidence, while 0° and 180° represent end-on incidence.

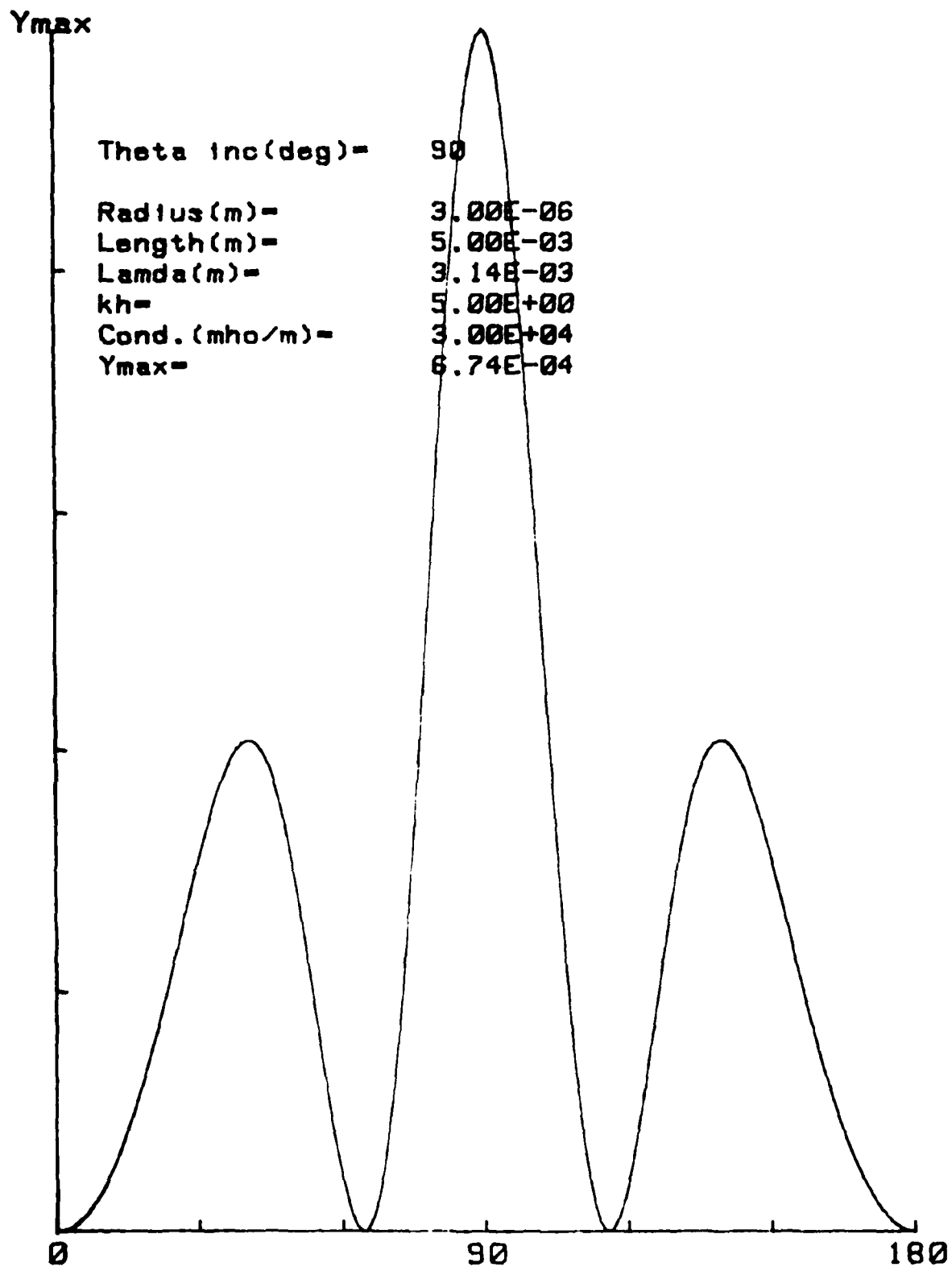


Figure 8. Differential Cross Section/Lambda² for kh = 5; $\theta_i = 90^\circ$

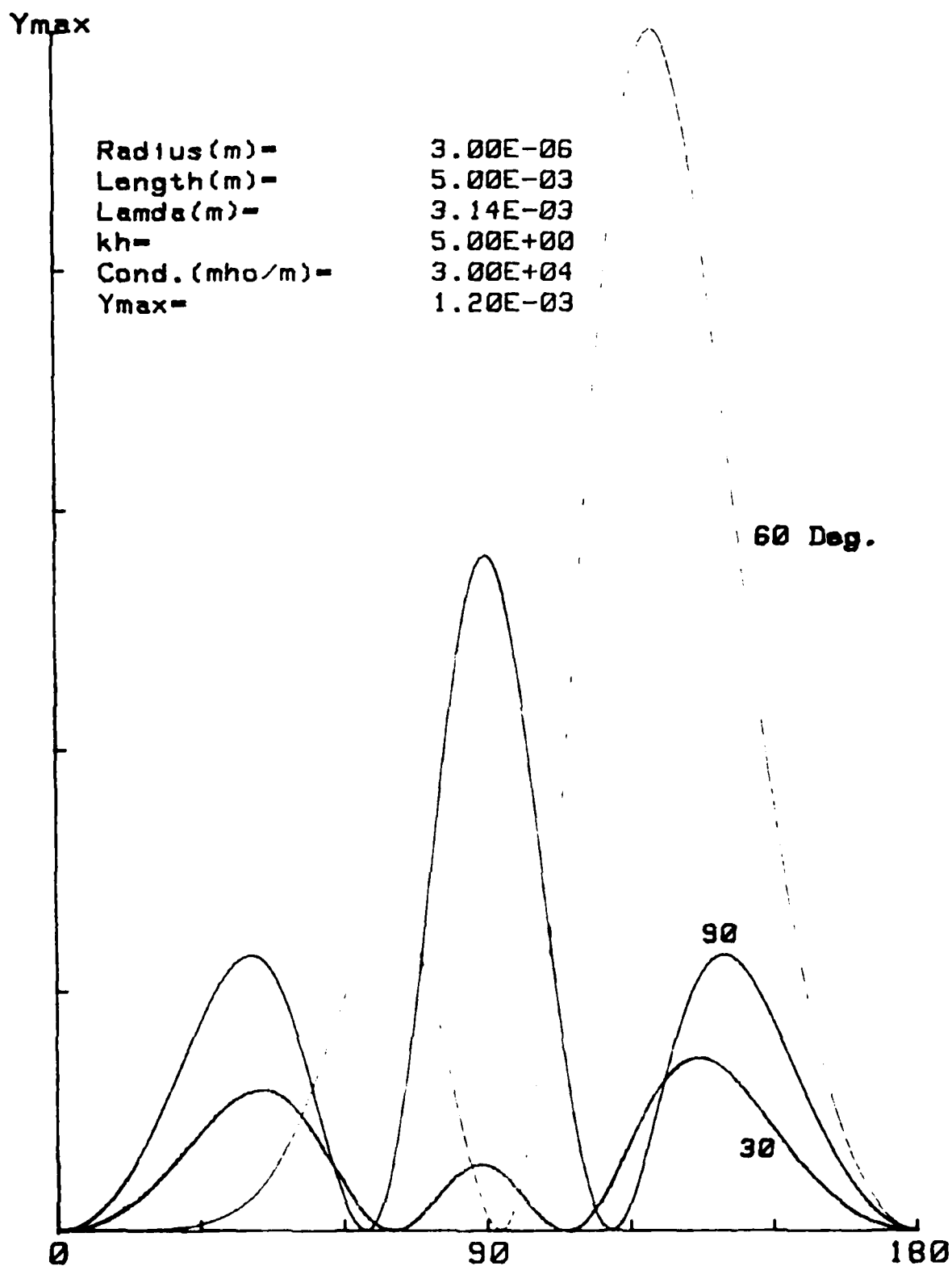


Figure 9. Composite Differential Cross Section/Lambda² for $\theta_i = 30^\circ, 60^\circ, \text{ and } 90^\circ$ and $kh = 5$

Figure 10 corresponds to the onset of the first (\sim half wavelength) resonance. Note that the angular symmetry of the data is off by 10 to 15 degrees. If this were corrected, reasonably good quantitative agreement would be observed.

Figure 11 corresponds to the first resonance ($\ell/\lambda = 0.480$) and we find excellent agreement between theory and experiment. Figure 12 ($\ell/\lambda = 0.496$) shows good experimental symmetry and agreement within 10%. In Fig. 13, in which $\ell/\lambda = 0.525$, the agreement is better than 10% when corrections are made for experimental asymmetry.

Note in Fig. 14, for which $\ell/\lambda = 0.854$ the broadside (90°) peak observed in Figs. 11 through 13, has split and the RCS is reduced. Although the features of the theory vs. experiment agree, the quantitative agreement is only within $\sim 25\%$ to 30% in Fig. 14.

Figures 15 and 16 correspond to $\ell/\lambda = 0.929$ and $\ell/\lambda = 1.051$, respectively. In Fig. 15, the experimental amplitude asymmetry is about 12%, while the agreement between theory and experiment are within about 18%. In Fig. 16, a new maximum has formed at 90° and 270° . The entire pattern is reduced and only moderate (20 to 25%) theoretical experimental agreement is observed.

3.2.2 Backscatter Cross Section vs. kh .

In this sub-section, we first compare the results of the present theory with some early experimental measurements on highly conducting wires by As and Schmitt^{6,7} with the results of the present theory. Figure 17, the experimentally observed backscatter cross section per square wavelength is plotted as a function of kh for three values of ka . Note that an error exists in this Figure. The solid line ($ka = 0.132$) and the dotted line ($ka = 0.026$) were obviously inadvertently interchanged in the

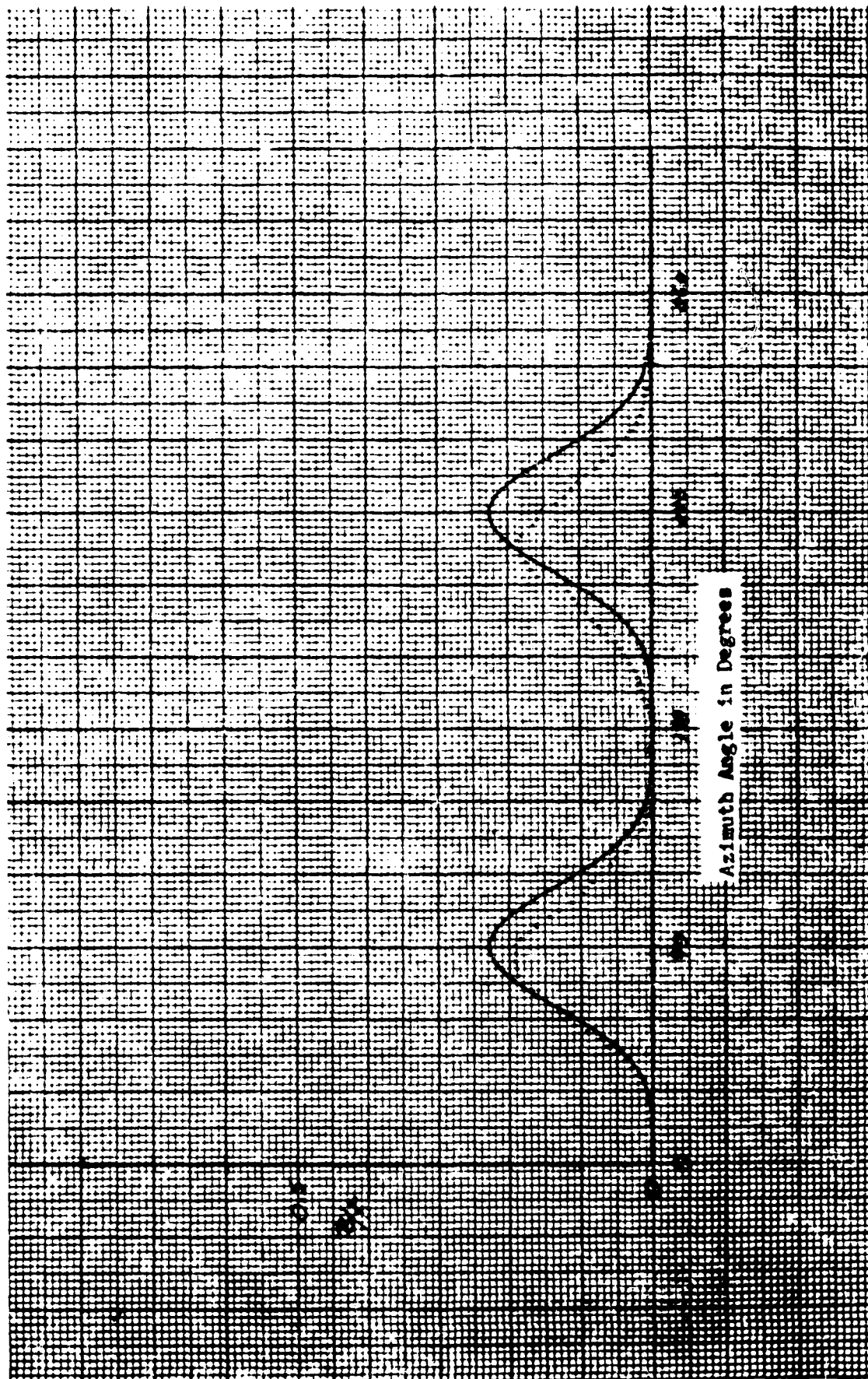


Figure 10. Radar Cross Section/Lambda² of a Tungsten Wire as a Function of Angle of Incidence, θ_i , for $\ell/\lambda = 0.437$ and $\ell/d = 500$

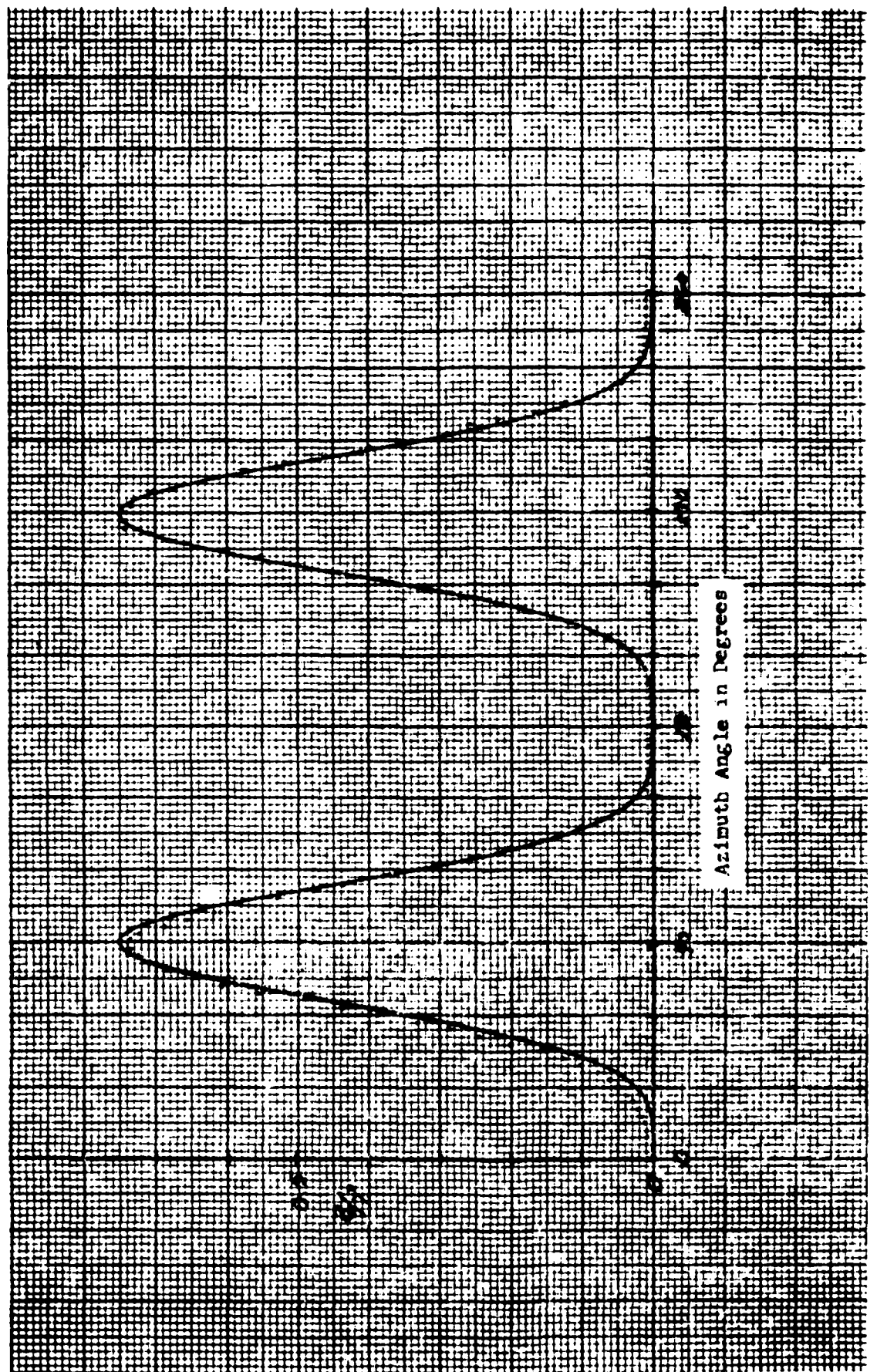


Figure 11. Radar Cross Section/ λ^2 of a Tungsten Wire as a Function of Angle of Incidence, θ_i , for $\ell/\lambda = 0.480$ and $\ell/d = 605$

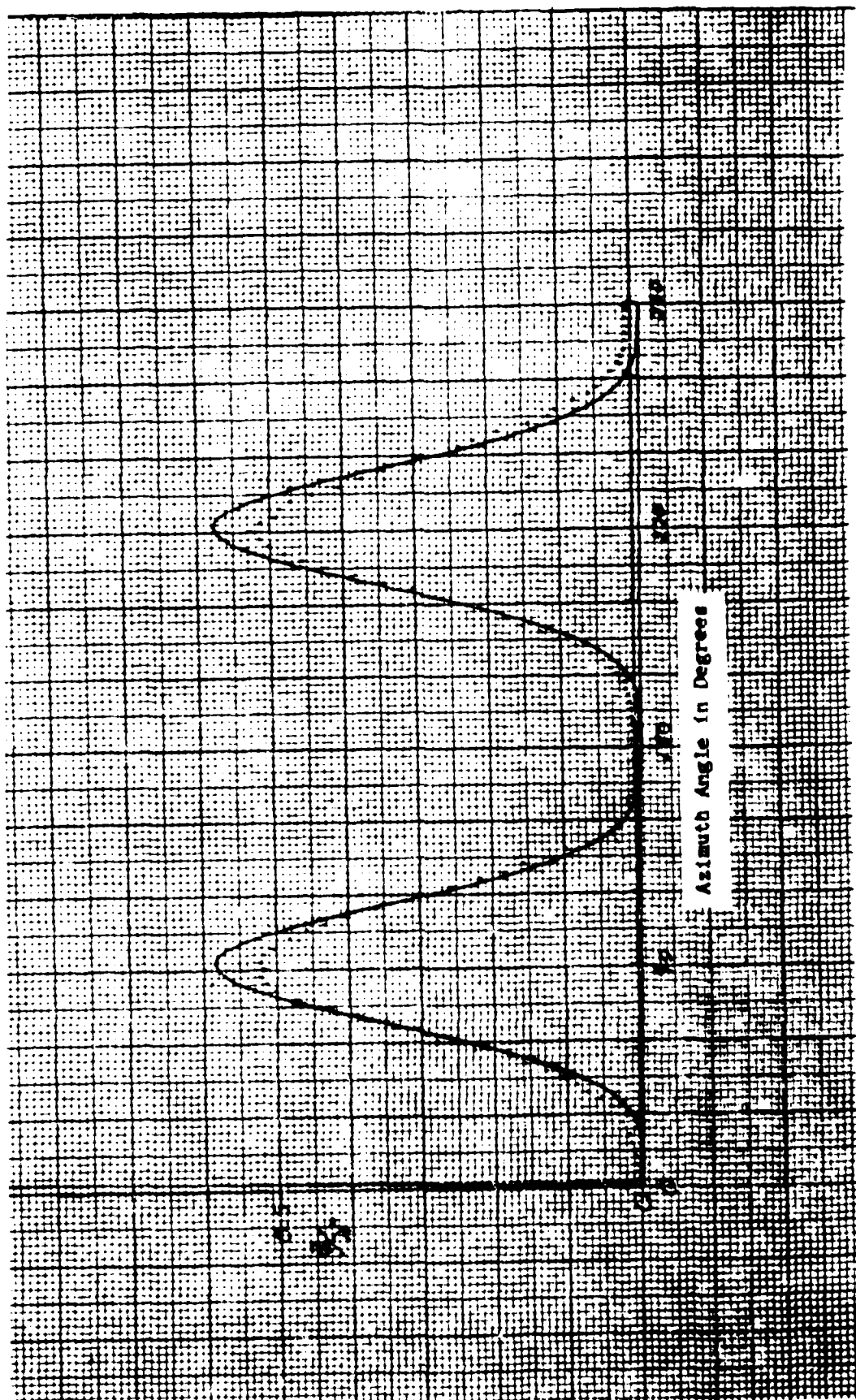


Figure 12. Radar Cross Section/Lambda² of a Tungsten Wire as a Function of Angle of Incidence, θ_i for $\ell/\lambda = 0.480$ and $\ell/d = 500$

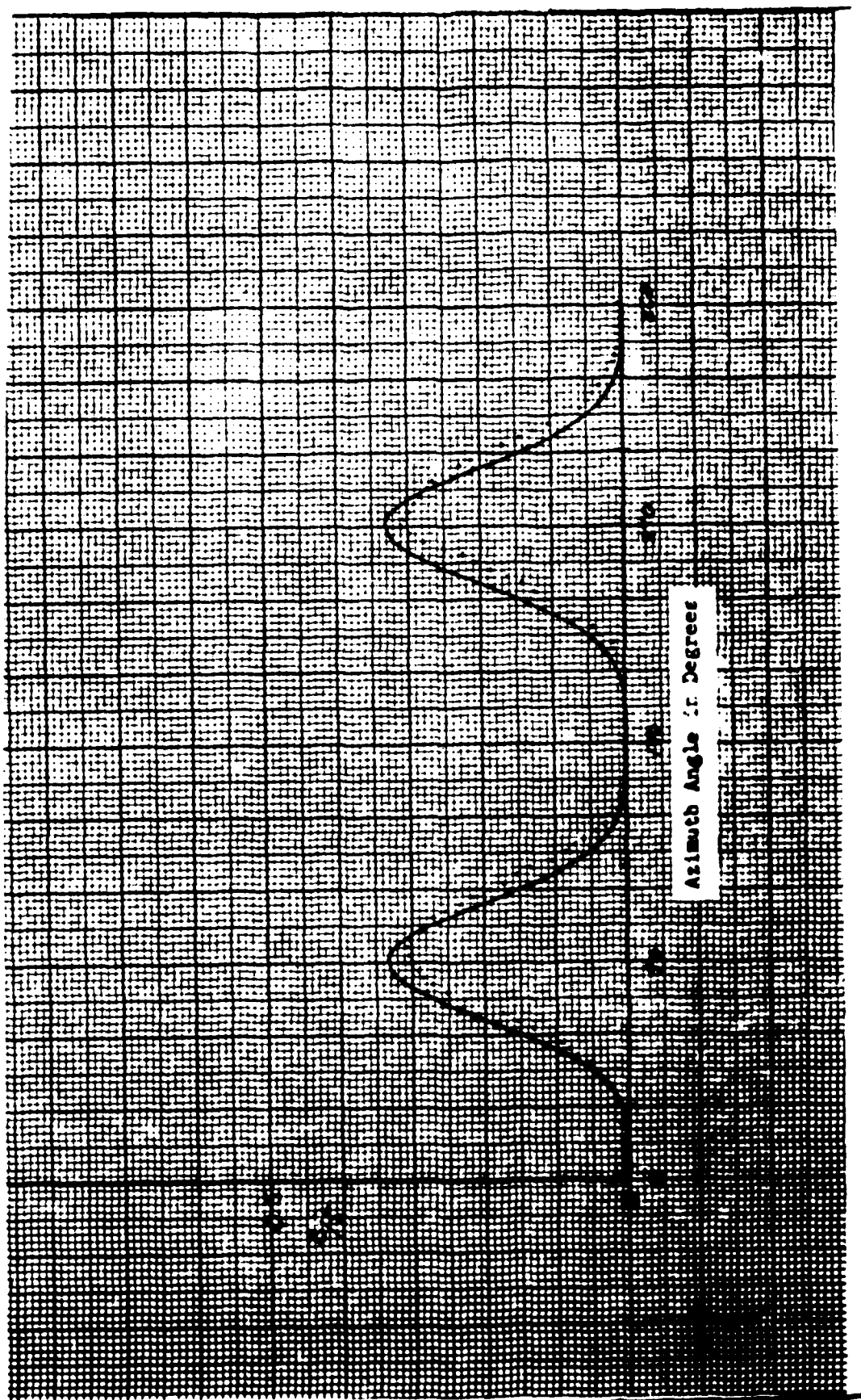


Figure 13. Radar Cross Section/ λ^2 of a Tungsten Wire as a Function of Angle of Incidence, θ_i , for $l/\lambda = 0.525$ and $l/d = 660$

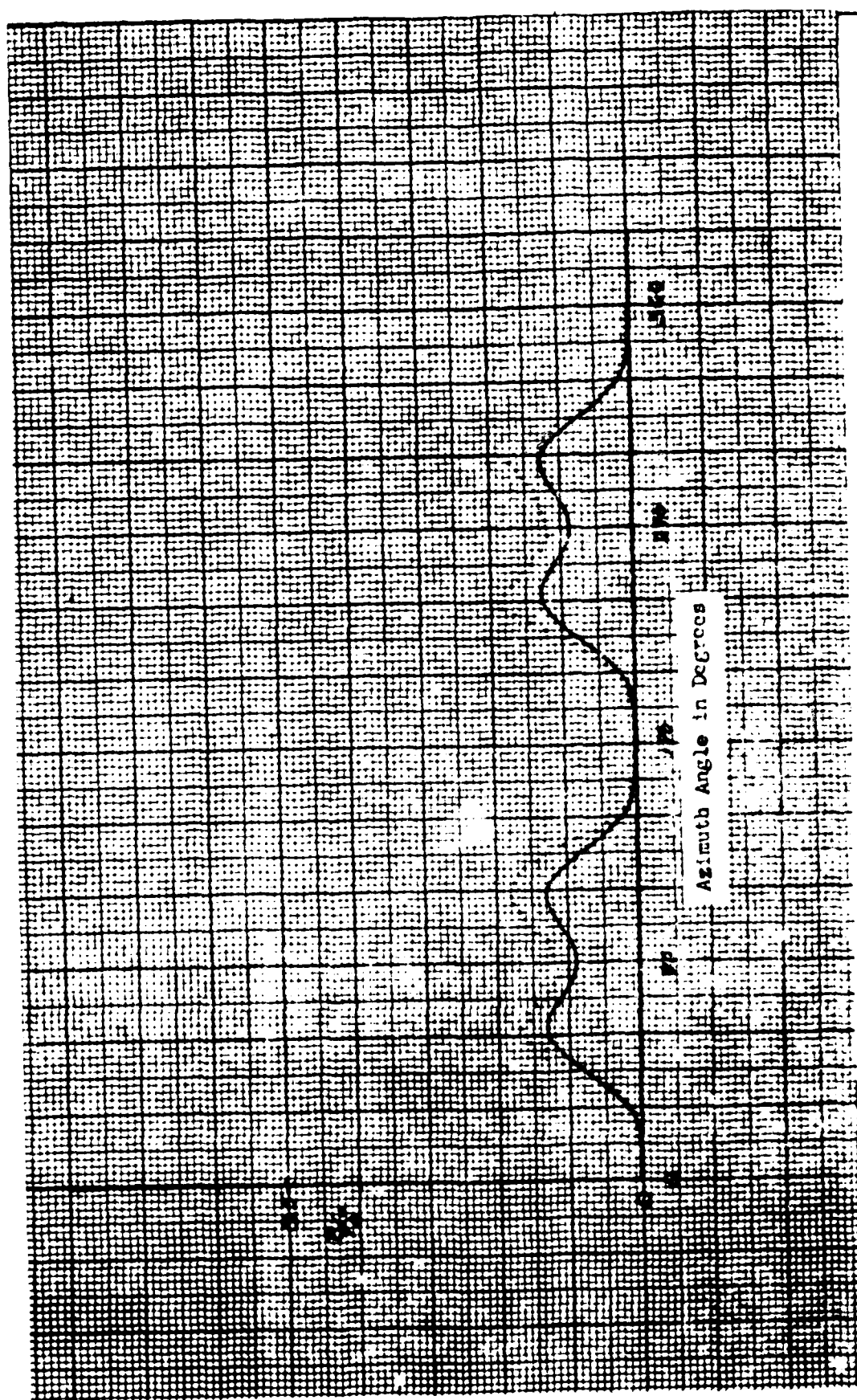


Figure 14. Radar Cross Section/ λ^2 of a Tungsten Wire as a Function of Angle of Incidence, θ_i , for $\ell/\lambda = 0.854$ and $\ell/d = 717$

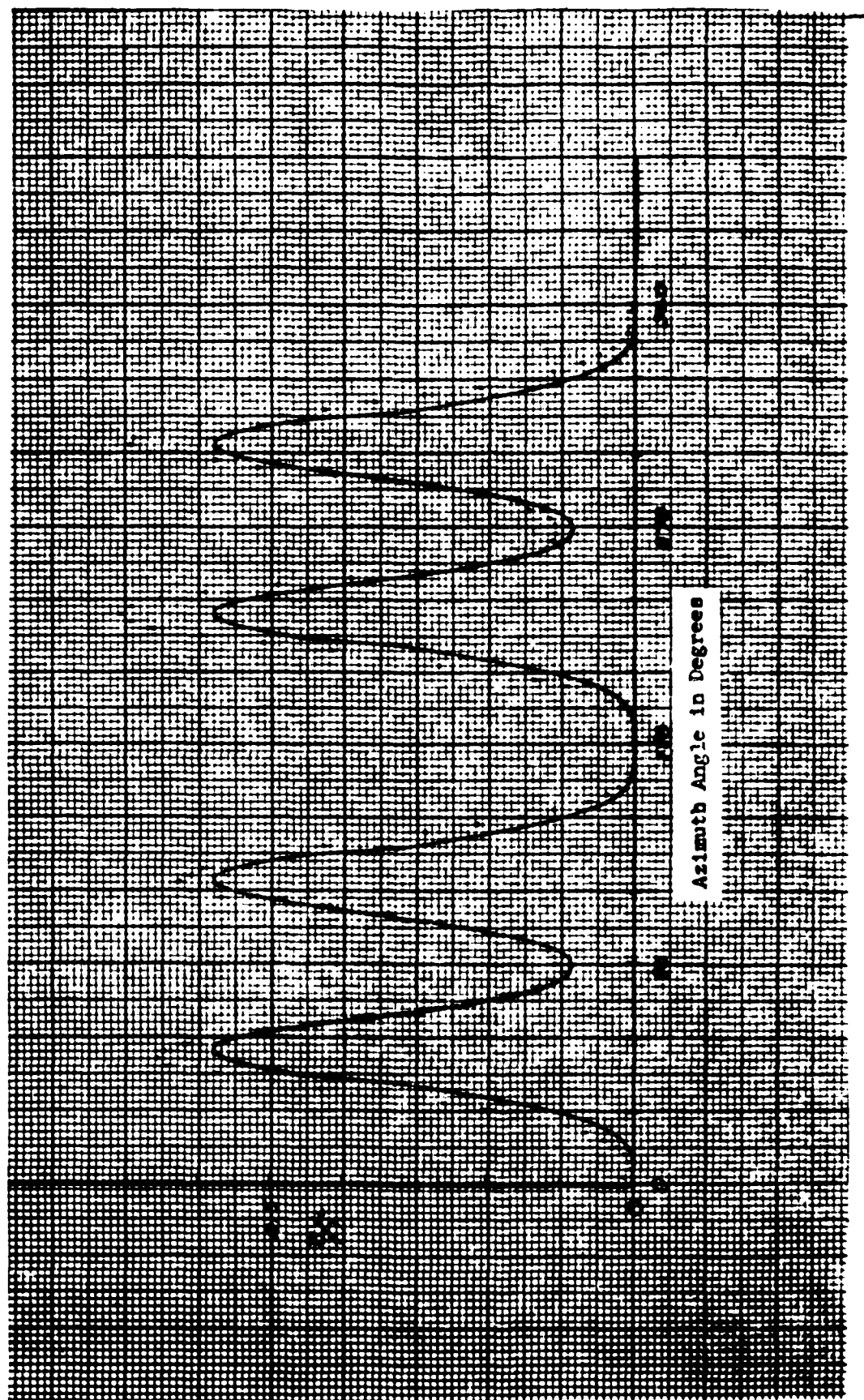


Figure 15. Radar Cross Section/ Lambda^2 of a Tungsten Wire as a Function of Angle of Incidence, θ_i , for $\ell/\lambda = 0.929$ and $\ell/d = 780$

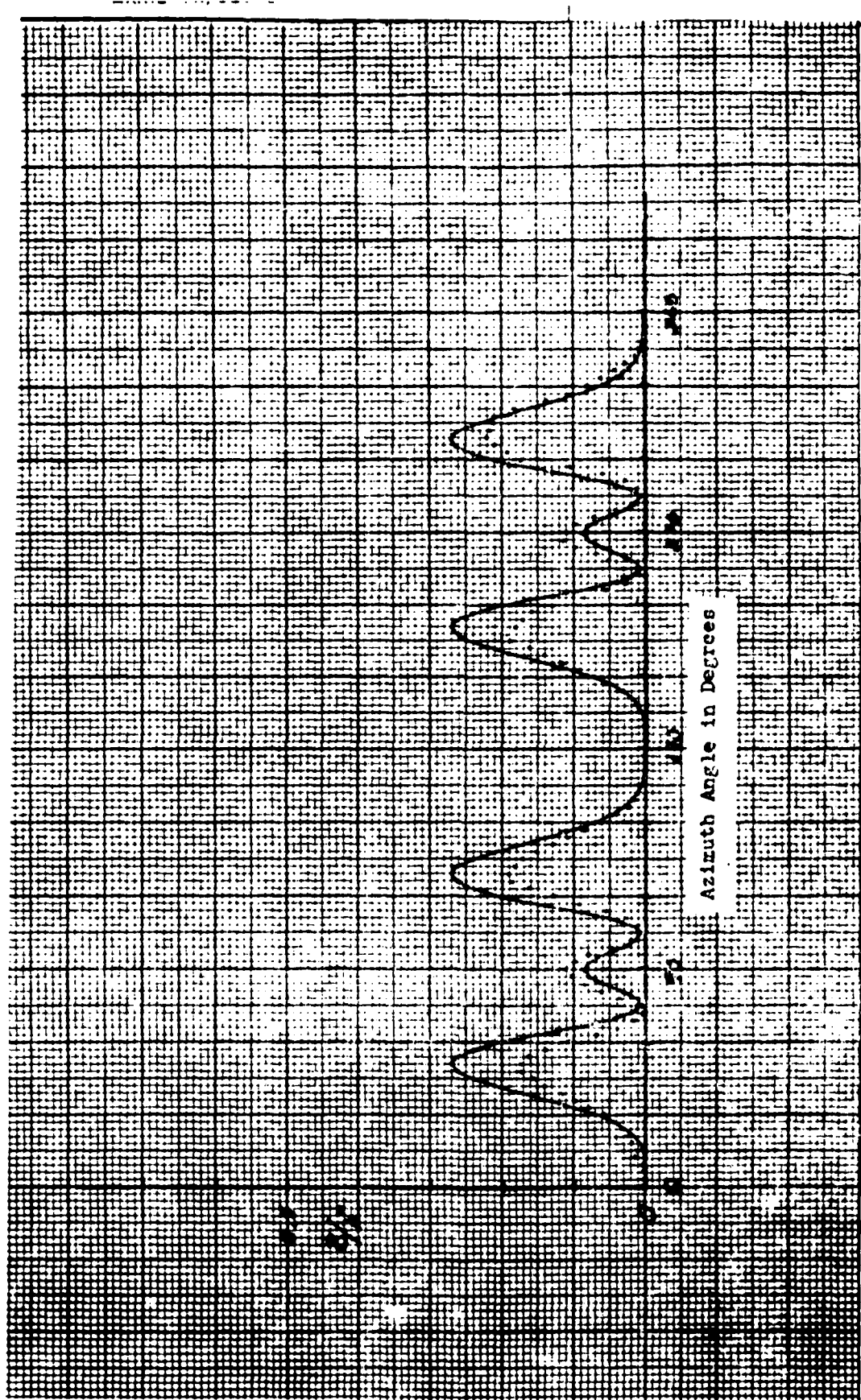


Figure 16. Radar Cross Section/ λ^2 of a Tungsten Wire as a Function of Angle of Incidence, θ_i , for $\ell/\lambda = 1.051$ and $\ell/d = 884$

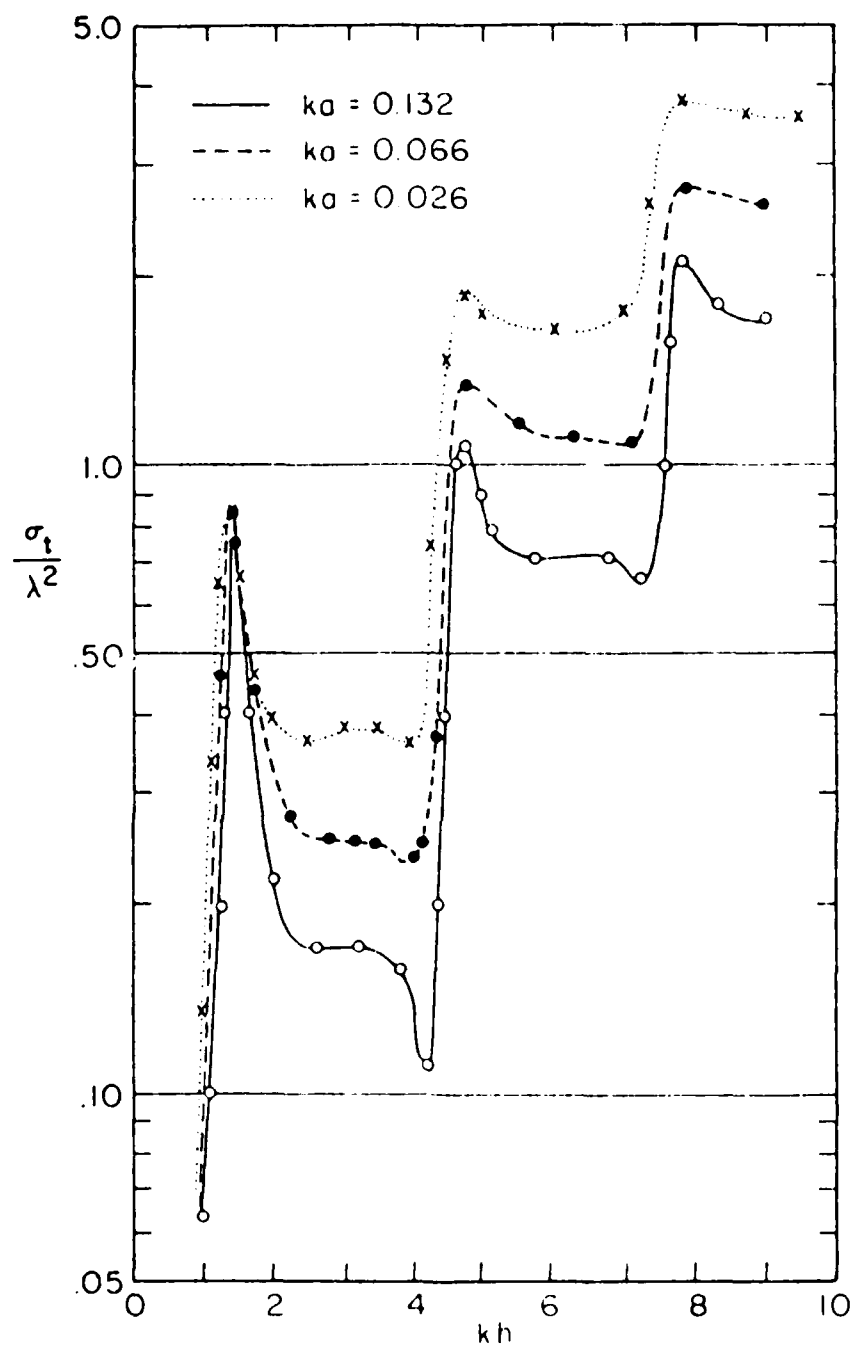


Figure 17. Experimentally Measured Backscatter Cross Section/
 Lambda^2 for Infinitely Conducting Cylinders at
 Broadside Incidence as a Function of kh .^{7,8}

original paper by As and Schmitt and the error was reproduced in King and Wu.

Figure 18 shows the results of the present theory for the same parameters as those of Fig. 17. Note that, except for the deep minima of Fig. 18, excellent quantitative agreement is demonstrated. The existence of these minima will be discussed in Section 3.5.

Figure 19 shows the behavior of the backscatter cross section vs. kh for four electrical conductivity values ranging from 100 mho/m to infinity. Note that (a) as we would expect, the backscatter cross sections decrease with decreasing conductivity, (b) the plateaus degenerate to simple maxima, and (c) the three very deep minima persist even for small values of electrical conductivity.

3.3 Very Large Values of kh .

We next investigate the behavior of the theory when kh becomes very large. The purposes of this are (a) to test the stability of our solutions in the very large kh range, (b) to determine, if possible, asymptotic expressions for the cross sections, and (c) to see if the solutions appear to be reasonable on physical grounds.

In Figures 20 and 21, which are analogous to Fig. 17, we have plotted (linear plot) backscatter cross section per square wavelength vs. kh over the range $0.25 \leq kh \leq 100$. In Fig. 20, $ka = 10^{-4}$ and in Fig. 21, $ka = 10^{-3}$. We find that

- (a) the backscatter cross section appears to be well behaved in the very large kh regime
- (b) The minima of Fig. 17 persist to at least $kh = 100$.

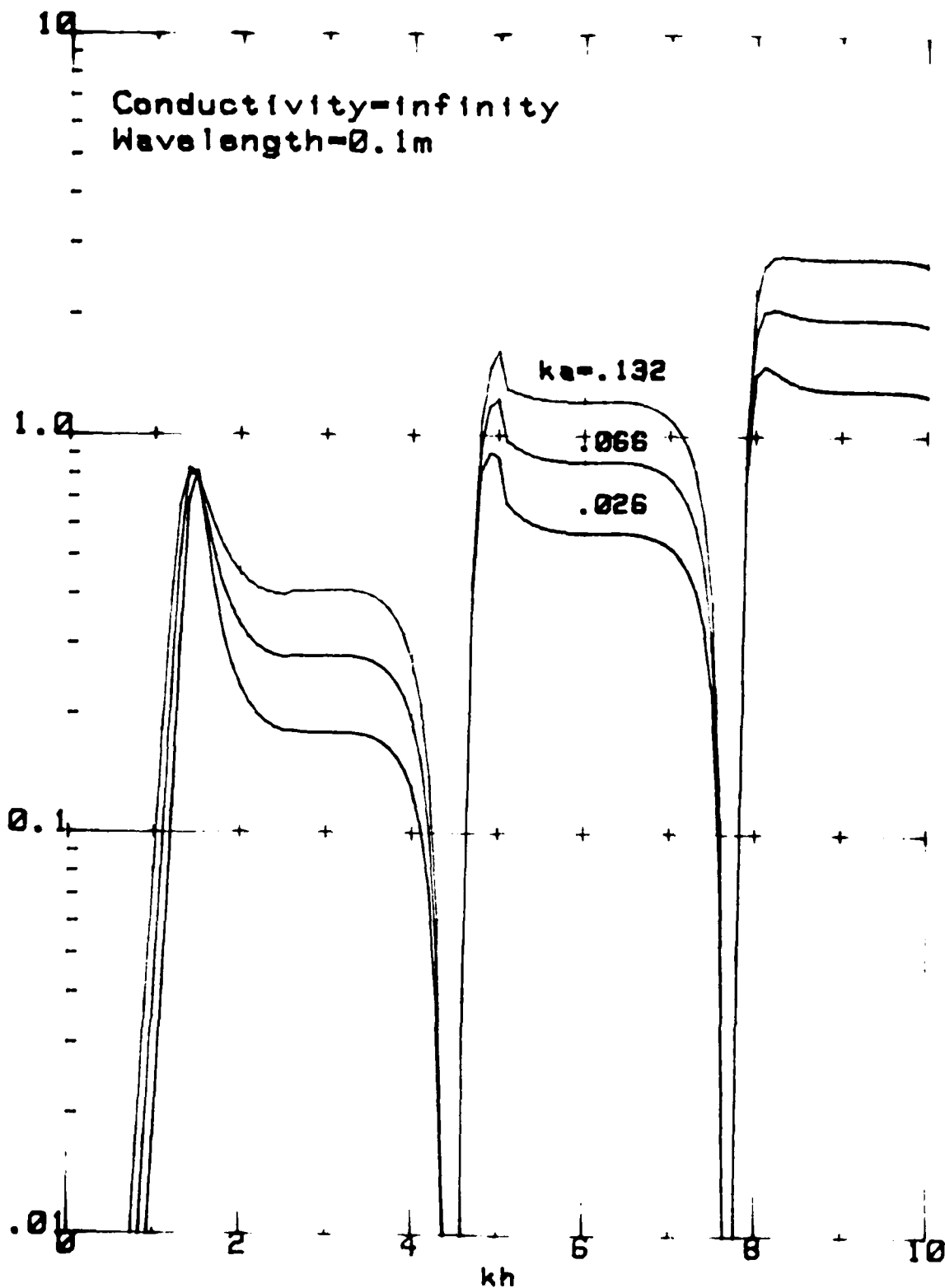


Figure 18. Calculated Backscatter Cross Section/ λ^2 for Infinitely Conducting Cylinders at Broadside Incidence as a Function of kh , $kh \leq 10$

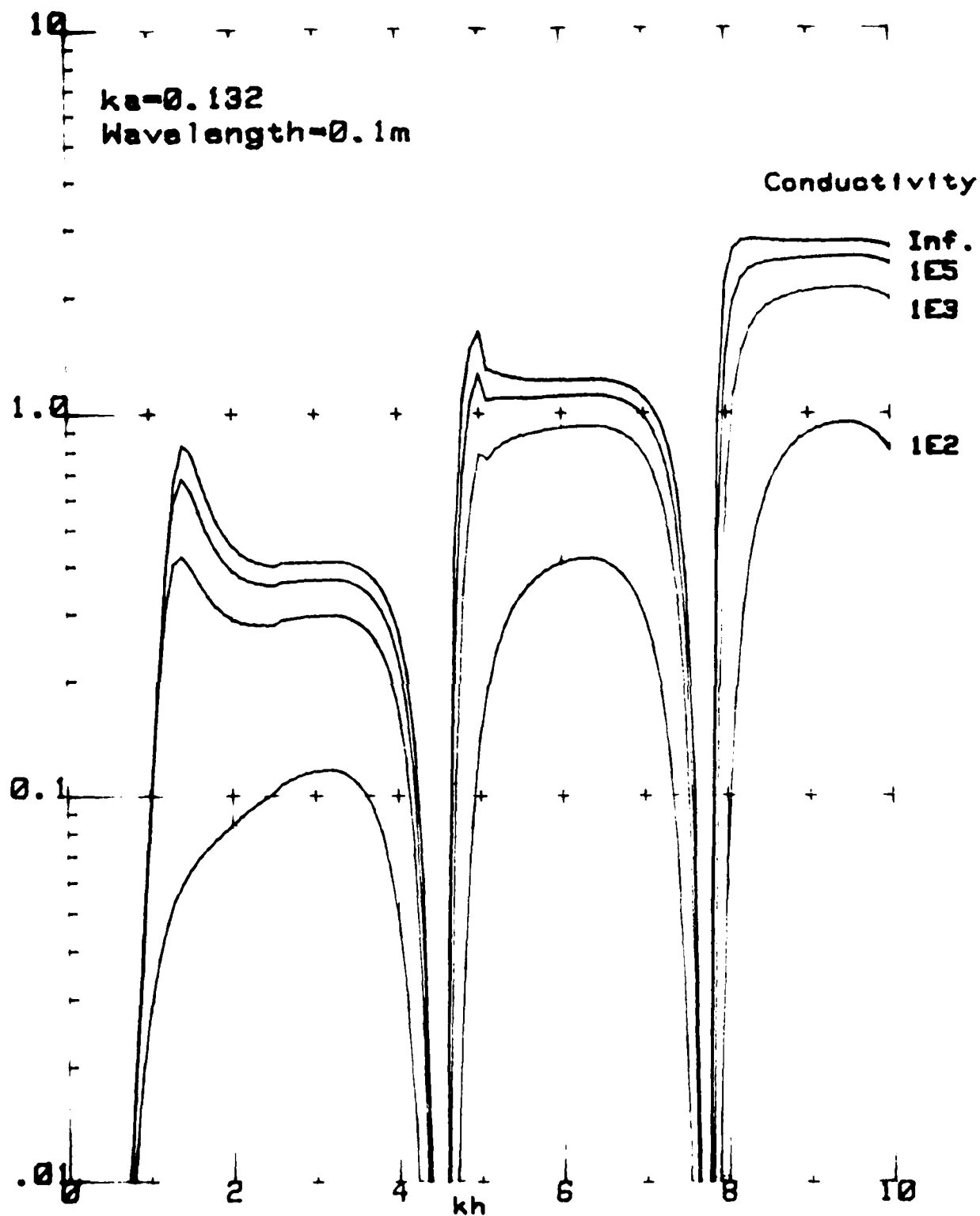


Figure 19. Calculated Backscatter Cross Section/ λ^2 for Resistive Cylinders at Broadside Incidence as a Function of kh , $kh \leq 10$

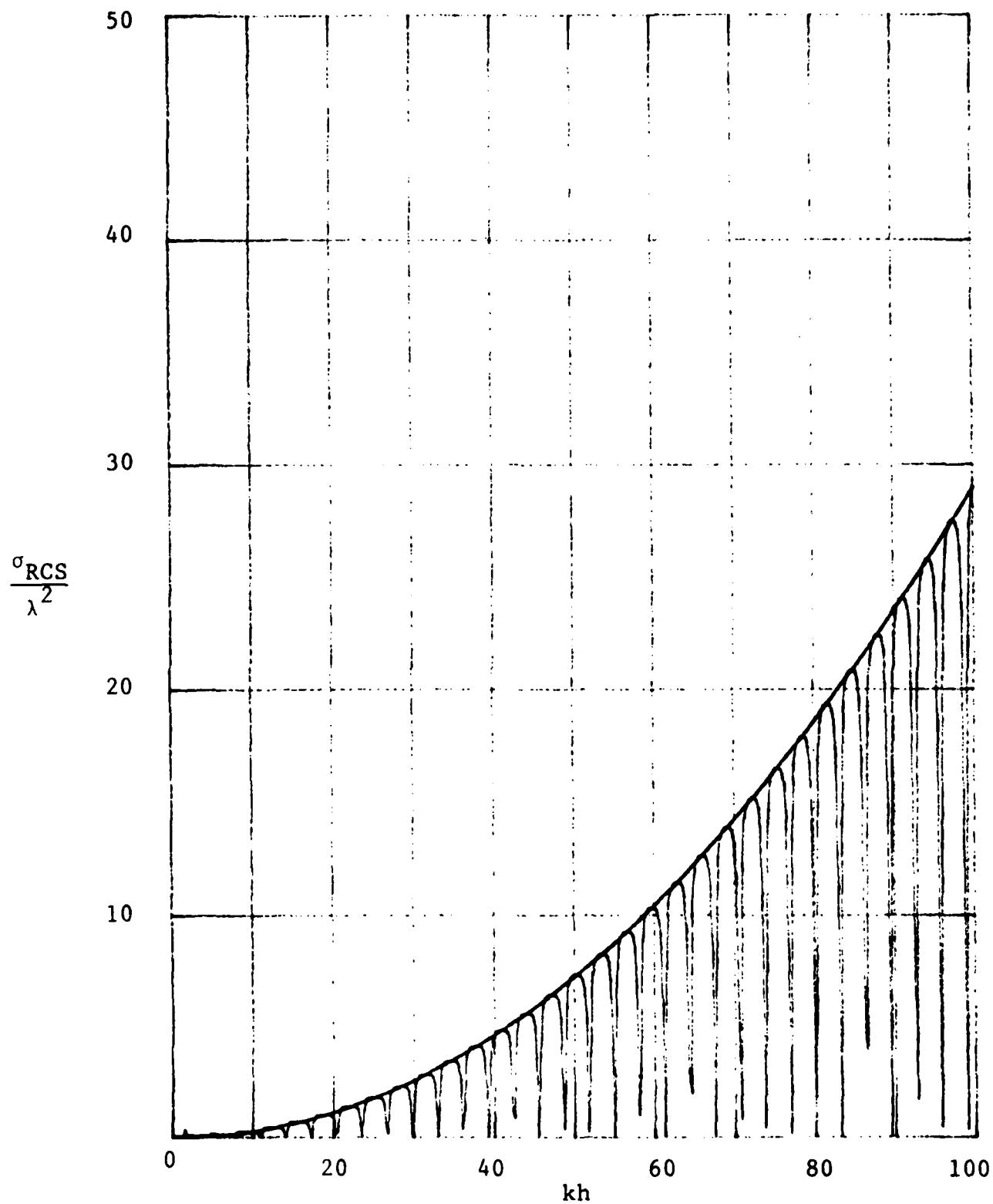


Figure 20. Calculated Backscatter Cross Section/ λ^2 for Infinitely Conducting Cylinders at Broadside Incidence as a Function of kh , $kh \leq 100$ and $ka = 10^{-4}$

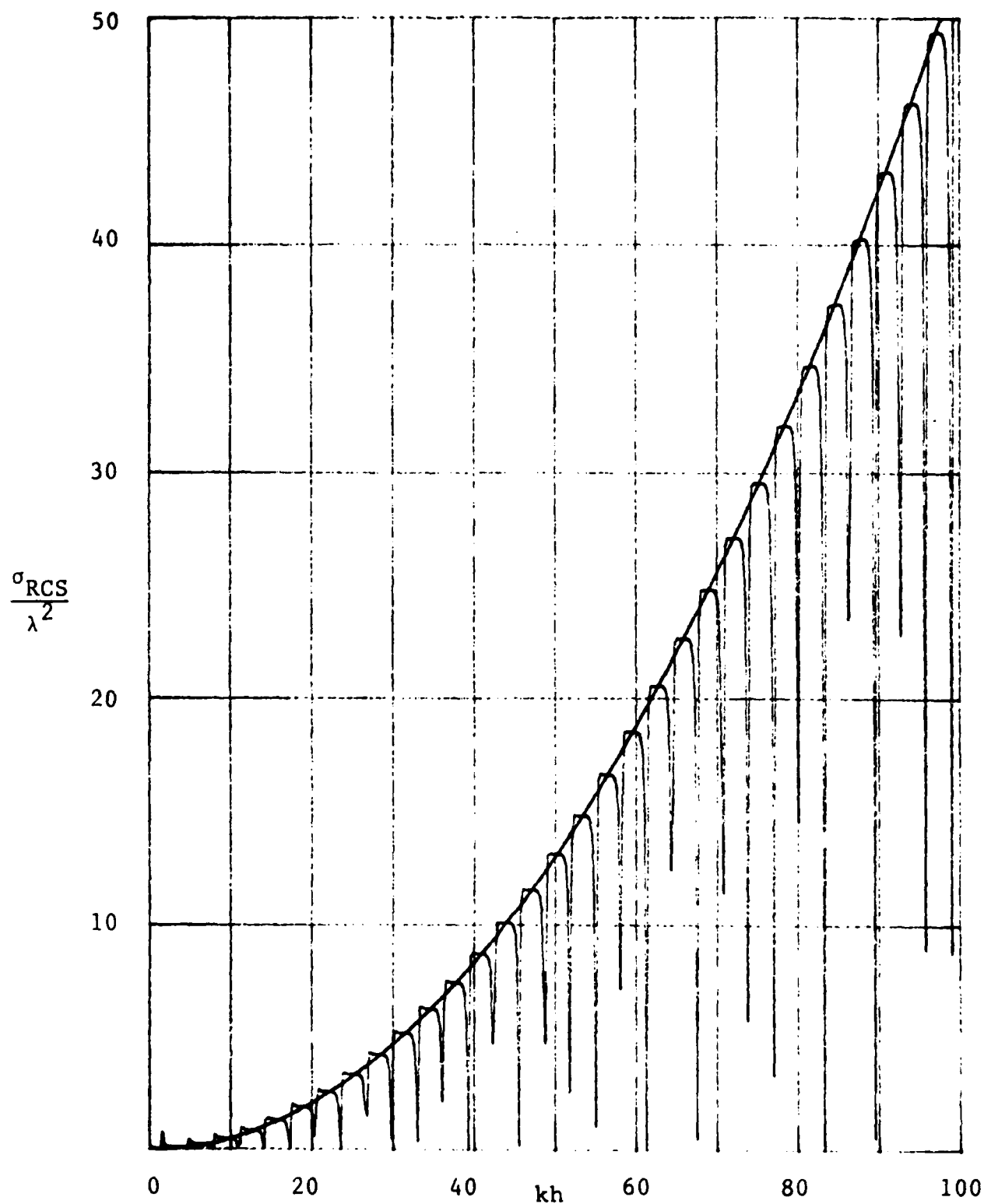


Figure 21. Calculated Backscatter Cross Section/ λ^2 for Infinitely Conducting Cylinders at Broadside Incidence as a Function of kh , $kh \leq 100$ and $ka = 10^{-3}$

An analysis of Figs. 20 and 21 gives the following asymptotic relationship:

$$\frac{\sigma_{\text{RCS}}}{\lambda^2} = \frac{1}{4} \left(\frac{kh}{\ln(ka)} \right)^2 \quad (42)$$

Another test of the theory is to observe the behavior of the differential scattering cross section in the very large kh limit. The results of these computations are given below.

Figures 22, 23, 24 and 25 show the behavior of the differential scattering cross section per square wavelength for various values of kh . The cylinder orientation is broadside, with E parallel to the cylinder axis. These values are $kh = 10, 15, 25$ and 100 . Note that, as kh is increased, (a) the width of the central maximum decreases, (b) the lobe structure becomes compressed, and (c) unexpected minor lobes appear near 0° and 180° .

Except for (c) above, the curves of Figs. 22 through 25 appear very normal and well behaved. Also, we have shown that the main lobe structure agrees exactly with the usual $(\sin 2kh/2kh)^2$ representation.

Figures 26 and 27 represent an interesting and unanticipated result. First, note that the angle of incidence is 40° (or 50° off broadside). In Fig. 26 the total length ($2h$) of the cylinder is an odd multiple of a quarter wavelength. Specifically, the total length, $\ell = 2h$, is given by $\ell = 103.5 (\lambda/2)$. Although points are computed for only every degree of scattering angle, it can be seen that the scattering pattern is well behaved, with a large peak in the forward direction*.

*As was pointed out earlier in this report, the scattering is the same at the angle $180^\circ + \theta_i$ as at $180^\circ - \theta_i$. Therefore, the large peak at $180^\circ - \theta_i$ can be interpreted as forward scattering as well as scattering at $180^\circ - \theta_i$.

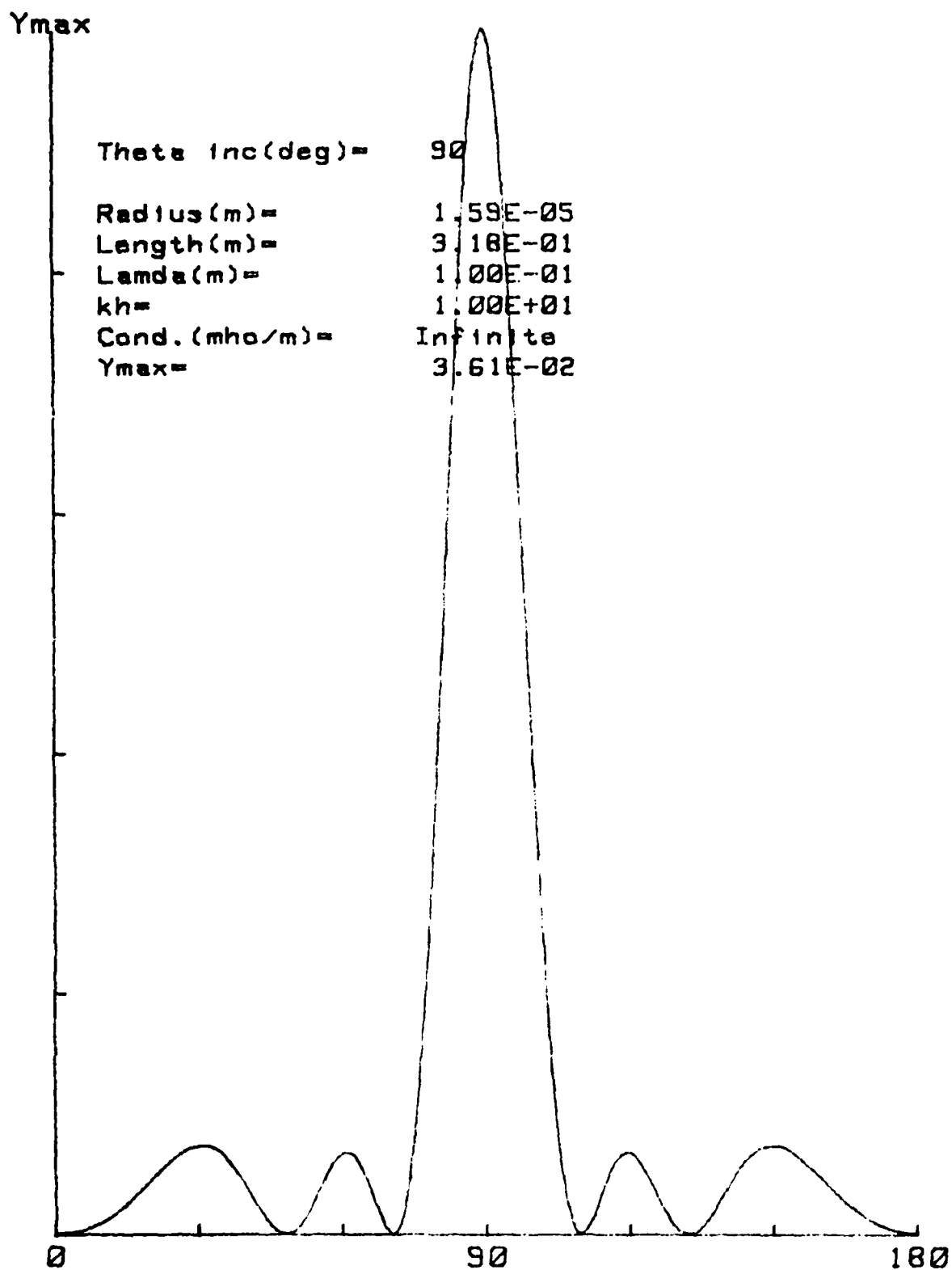


Figure 22. Differential Cross Section/ Lambda^2 for an Infinitely Conducting Cylinder, Broadside Incidence and $kh = 10$

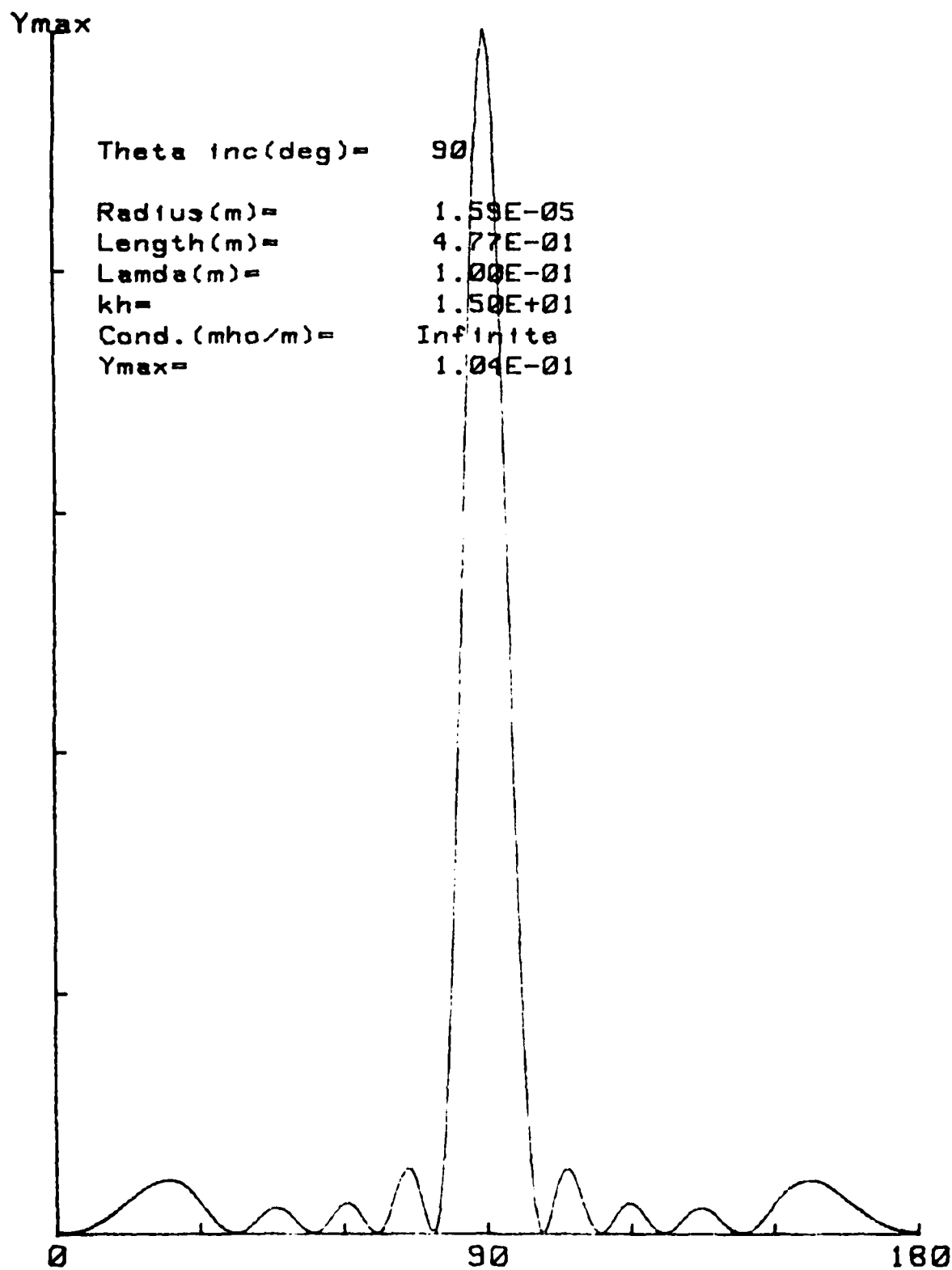


Figure 23. Differential Cross Section/ λ^2 for an Infinitely Conducting Cylinder, Broadside Incidence and $kh = 15$

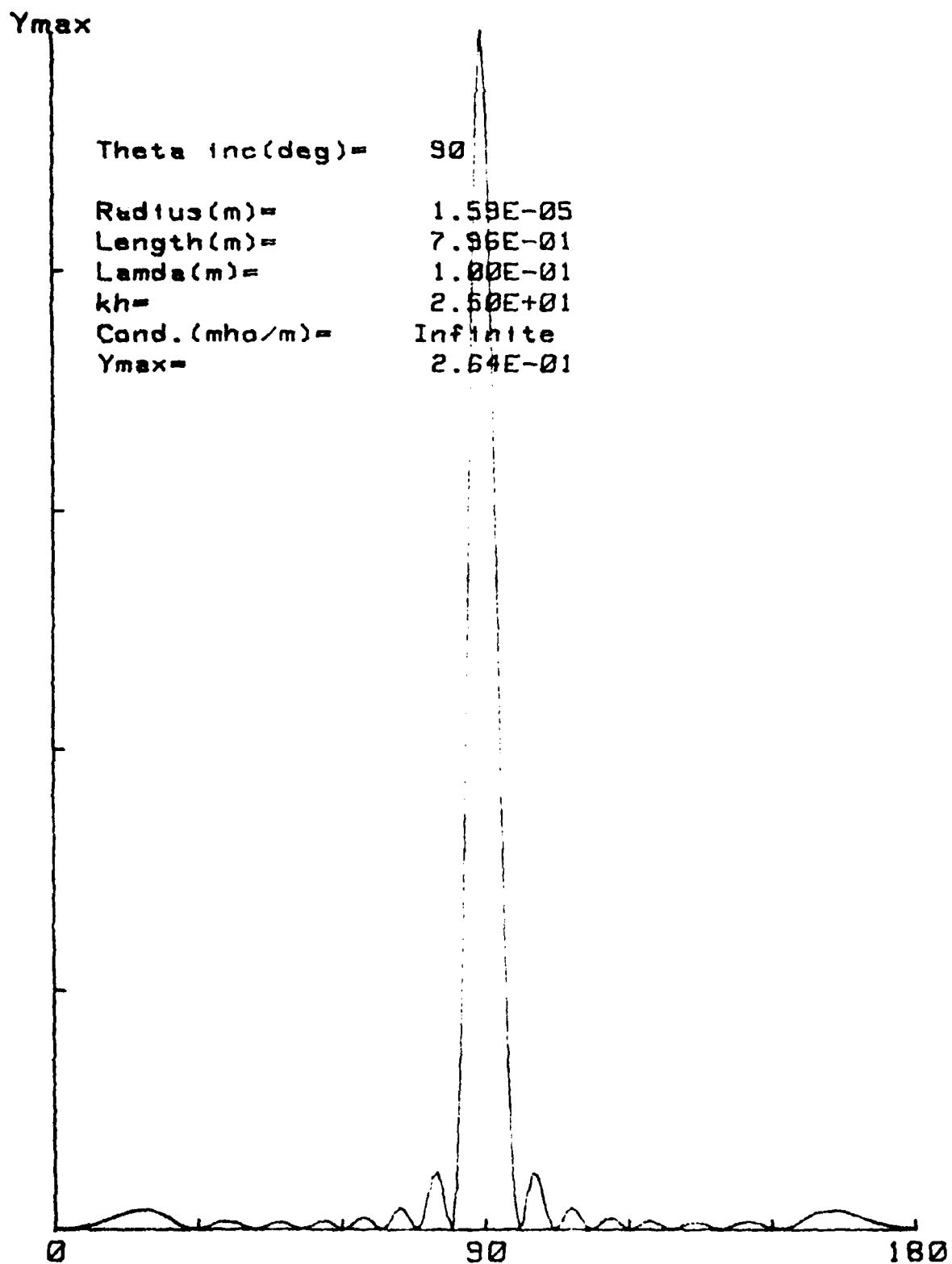


Figure 24. Differential Cross Section/ λ^2 for an Infinitely Conducting Cylinder, Broadside Incidence and $kh = 25$

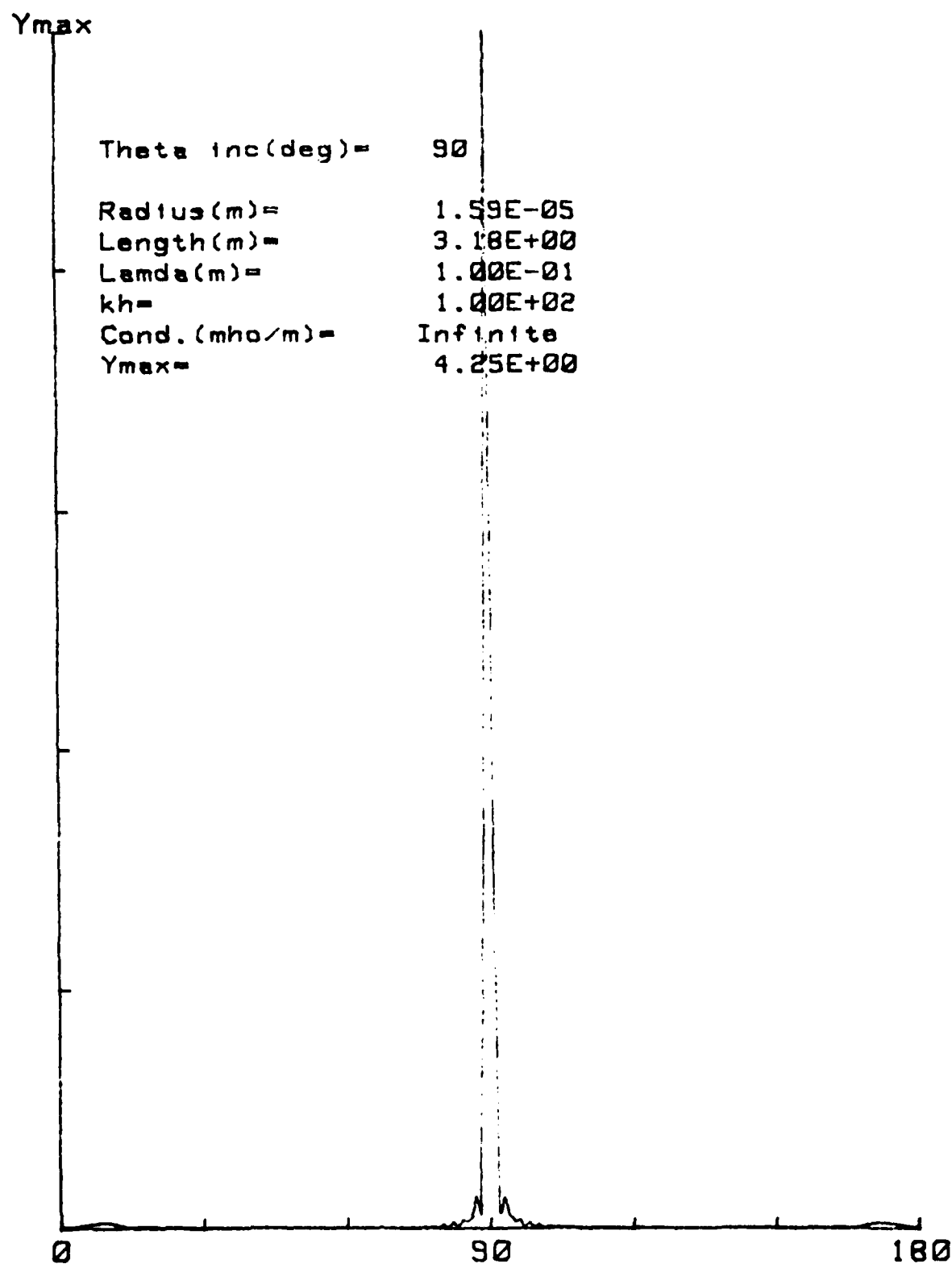


Figure 25. Differential Cross Section/ λ^2 for an Infinitely Conducting Cylinder, Broadside Incidence and $kh = 100$

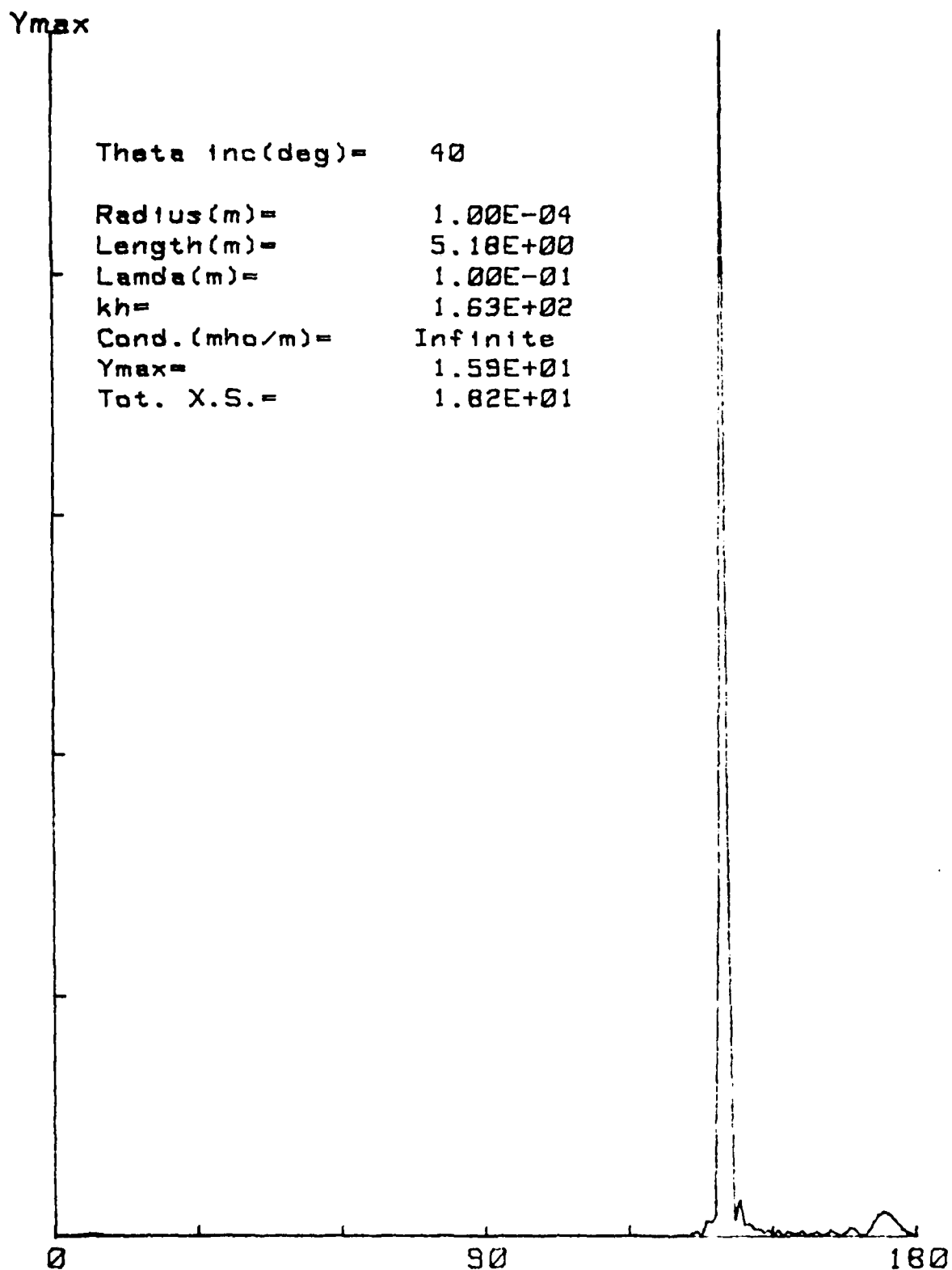


Figure 26. Differential Cross Section/Lambda² for an Infinitely Conducting Cylinder with $\theta_i = 40^\circ$ and $kh = 163$

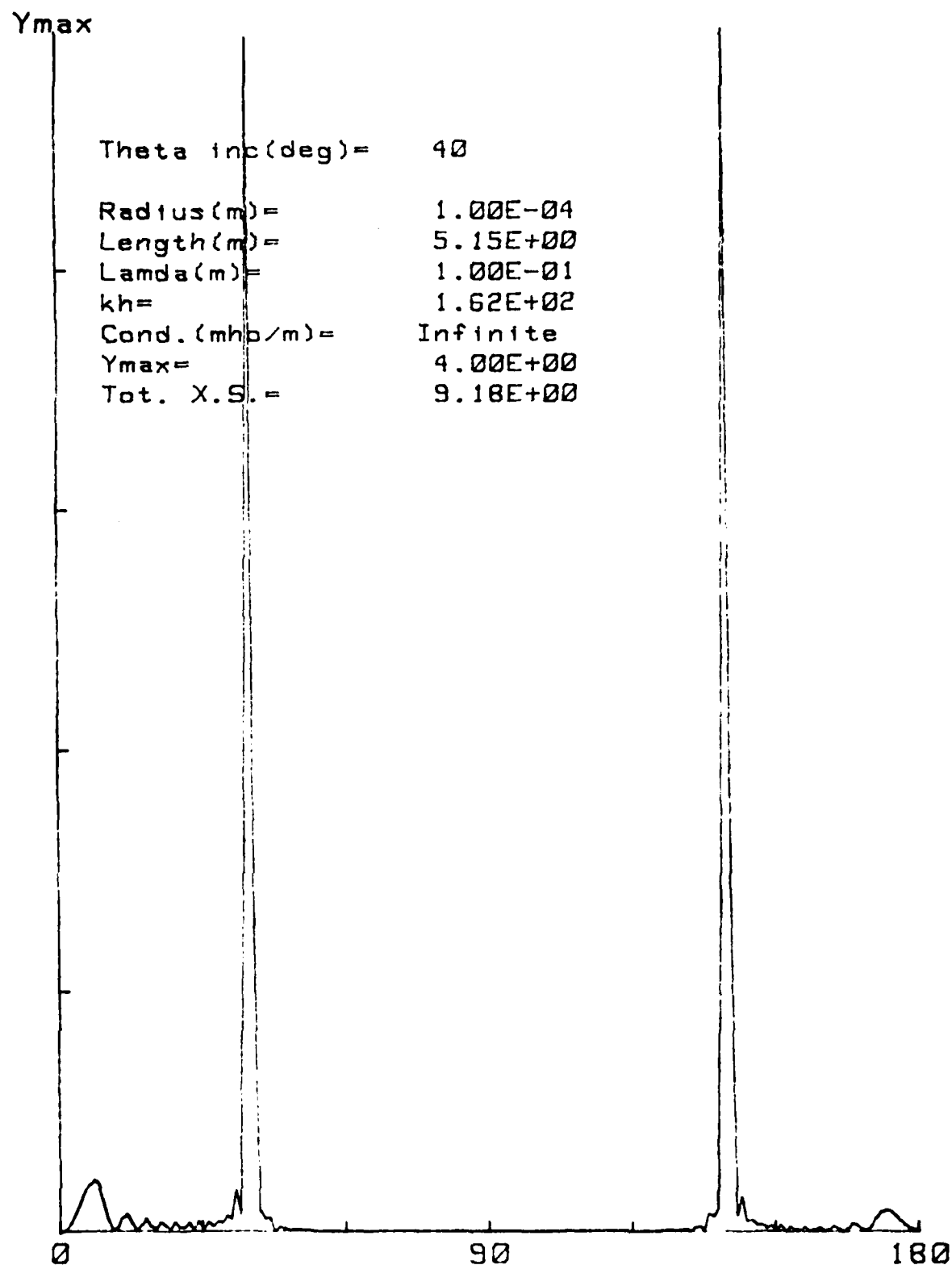


Figure 27. Differential Cross Section/Lambda² for an Infinitely Conducting Cylinder with $\theta_i = 40^\circ$ and $kh = 162$

This behavior of the scattering pattern is typical of nearly all of the $kh \gg 1$ scattering patterns which we have plotted. We have, however, found an exception to this behavior. It occurs within a very narrow range of kh when the total length is approximately equal to any (even or odd) multiple of a half wavelength. When such multiples occur, i.e., $\ell = 2h = N\lambda/2$ when $N \gg 1$, we find a large peak (equal to the forward scattering peak) in precisely the backscattering direction $\theta = \theta_i$.

This behavior occurs for all angles of incidence for which we have made computations. An example of this is shown in Fig. 28. This anomalous behavior occurs for less than 5% of the cylinder lengths if we continuously vary cylinder length ($\theta_i \neq 90^\circ$ and $kh \gg 1$) and observe the scattering in the backscattering ($\theta = \theta_i$) direction. A further discussion of this anomaly will be given in Section 4.

3.3.1 Averaged Extinction, Absorption, and Scattering Cross Sections vs. Wavelength.

In the case of transmission of electromagnetic radiation into clouds of randomly oriented conductive fibers, one is interested in the orientation averaged values of the extinction, absorption, and scattering cross sections. In particular, the cross section per unit volume of the particle is of importance. We have developed a computer program for the calculation of the above cross sections as a function of the wavelength of the incident radiation. The fixed parameters in the calculation are fiber radius, length, and conductivity. One hundred and twelve such sets of plots have been produced using the impedance of Eq. (2) and the current function given in Eqs. (32), (33) and (34). These plots are being forwarded to Dr. Jay Embury at C.S.L.

As examples of the above mentioned plots, Figs. 28, 29, and 30 predict the spectral characteristics of thin graphite fibers in the spectral range $0.1 \text{ micron} \leq \lambda \leq 100 \text{ microns}$. The fixed

PLOTS OF ELECTROMAGNETIC CROSS SECTIONS VS WAVELENGTH (ONS)

Filed 8, 24

$I = 4, J = 2, N = 2$

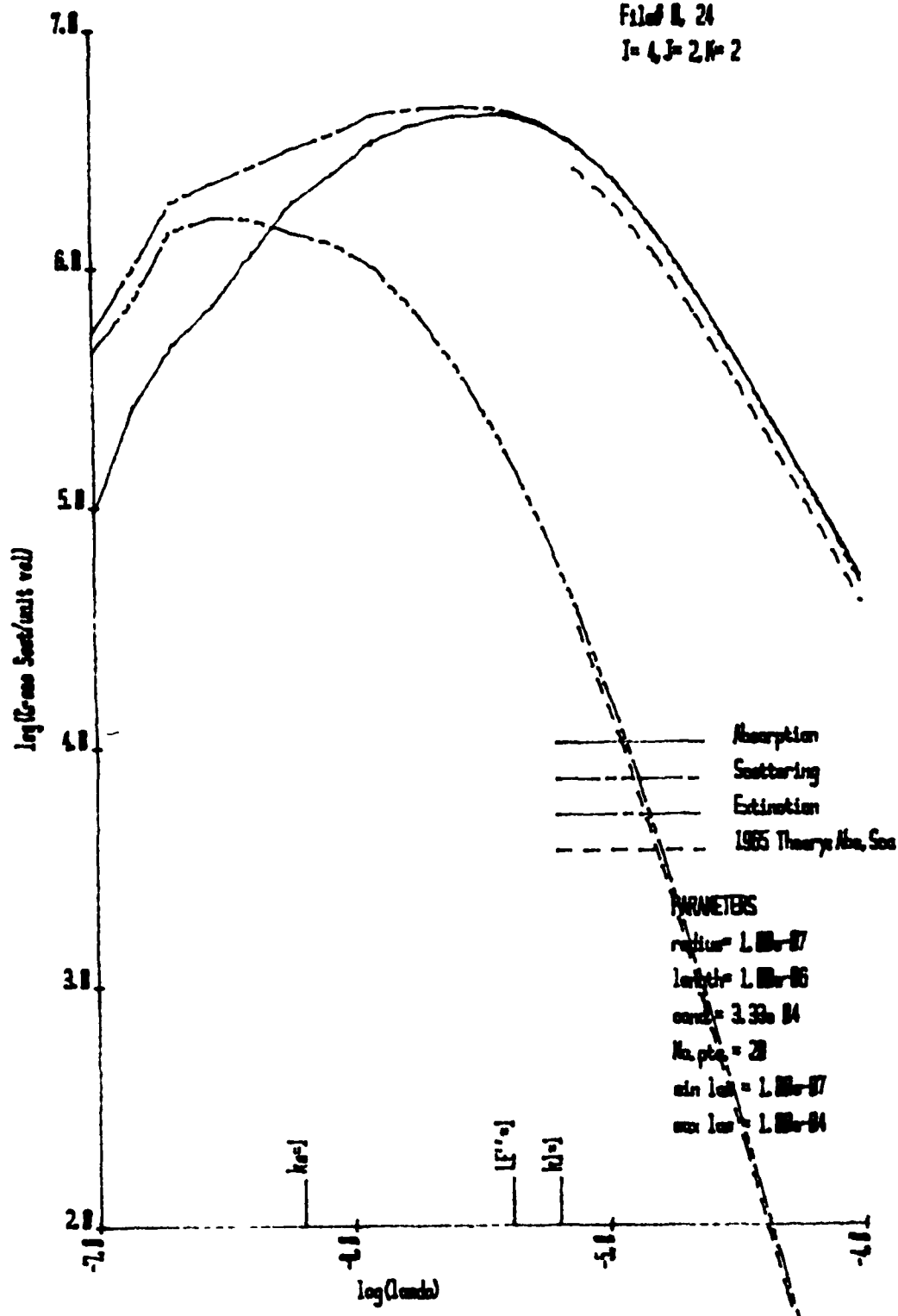


Figure 28. Orientation Averaged Electromagnetic Cross Section/
 Lambda^2 Versus Wavelength for a Cylinder 1×10^{-5}
Meters in Length

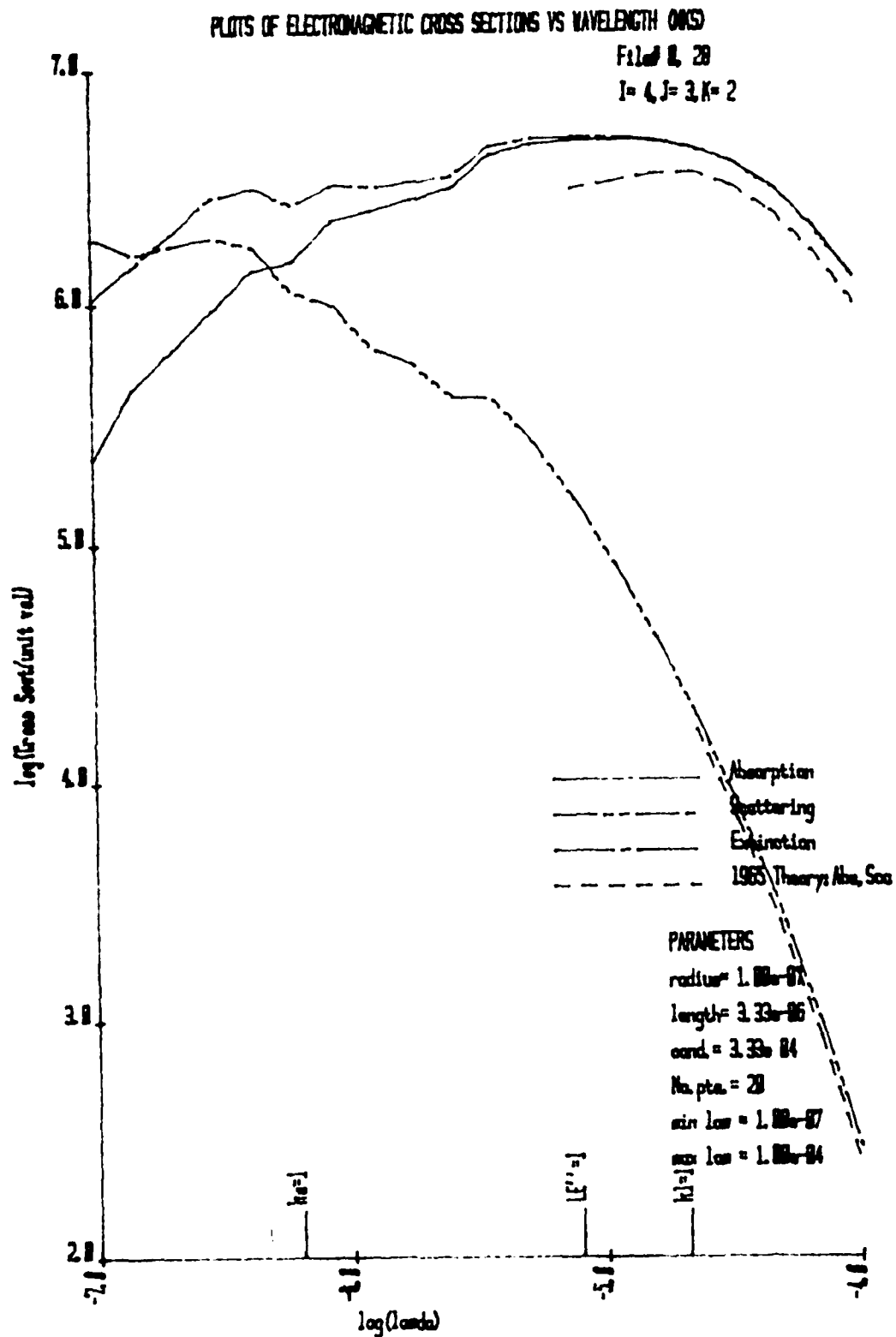


Figure 29. Orientation Averaged Electromagnetic Cross Sections/
 Lambda^2 Versus Wavelength for a Cylinder 3.33×10^{-6}
Meters in Length

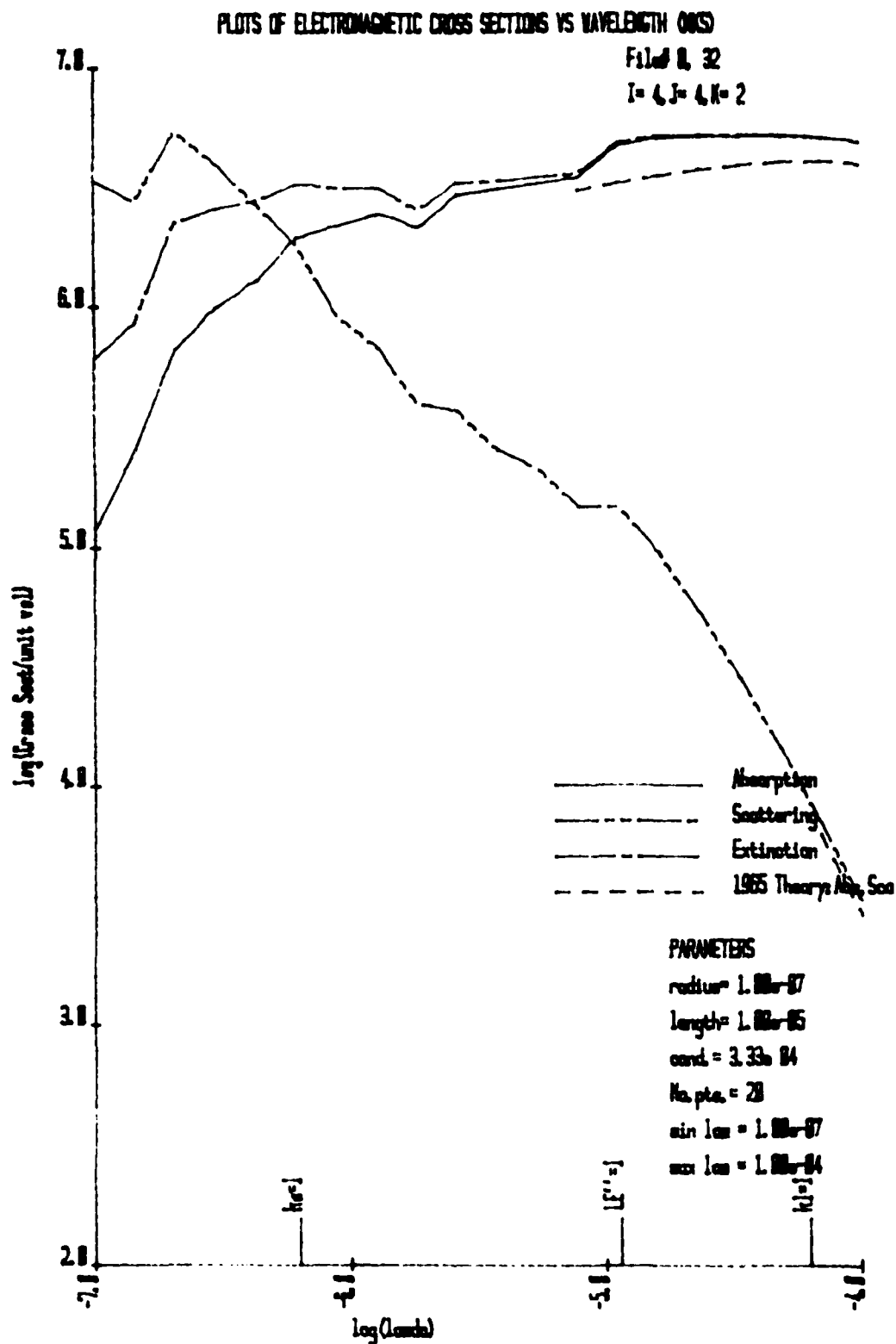


Figure 30. Orientation Averaged Electromagnetic Cross Sections/
 Lambda^2 Versus Wavelength for a Cylinder 1×10^{-6}
 Meters in Length

parameters are radius = 0.1μ , conductivity = 3.3×10^4 mho/m, and total length = 1μ , 3.3μ , and 10μ for Figs. 28, 29, and 30, respectively. The dashed lines correspond to scattering and absorption in the Rayleigh limit. Note that the various electromagnetic cross sections are averaged over particle orientation. It should also be noted that the orientation averaged scattering and absorption cross sections are computed by averaging these over all aspect angles and (in the case of scattering) all scattering angles, as shown by Eqs. (38) and (40). However, the extinction cross sections are computed using the Forward Amplitude theorem Eq. (39). At any wavelength, the sum of the scattering and absorption cross sections should, of course, be equal to the extinction cross section. Since the extinction cross section is computed by independent means, a good check on the theory is to determine whether or not the equality $\bar{\sigma}_{\text{abs}} + \bar{\sigma}_{\text{sca}} = \bar{\sigma}_{\text{ext}}$ prevails. Indeed, it can be seen by inspection of the three figures that the equality does exist throughout all but the shortest wavelength range of these.

The purpose of including three figures is to demonstrate the behavior of the cross sections as the fiber length is increased from one micron to ten microns. In Fig. 28, we see that the absorption cross section becomes maximum at about $\lambda = 10 \mu$ and is more than two orders of magnitude higher than the scattering cross section for wavelengths longer than 10μ .

In Fig. 29, the length has been increased from 1μ to 3.3μ and we see that the absorption reaches its maximum at $\lambda = 20$ to 30 microns and the scattering cross section is greater than that of Fig. 28.

Figure 30 shows the behavior when the total length is increased to 10 microns. Here, we see that the absorption (and extinction) are fairly constant over the range $1 \mu \leq \lambda \leq 100 \mu$.

The above Figures show that, increasing the length of the fiber from $1\ \mu$ to $10\ \mu$ has improved the absorptive (and extinction) properties of the fiber at the longer infrared wavelengths. It is also seen that, as fiber length is increased, the ratio of scattering to absorption cross sections increases (as we should expect).

It is important to note that the numerical integrations for $\bar{\sigma}_{sca}$ and $\bar{\sigma}_{abs}$ were carried out in 5° increments in both θ and θ_i . This rather coarse increment was necessary because of computer memory limitations. As kh becomes larger, the scattering patterns become more peaked, and the finer the angular integration increment should be. The use of a 5° increment is probably the reason for the inequality of $\bar{\sigma}_{sca} + \bar{\sigma}_{abs} = \bar{\sigma}_{ext}$. This tentative conclusion is reinforced by noting that the exact specular peak at $\theta = \pi - \theta_i$ is always included in the angular integration of the differential scattering cross sections, and it is therefore, weighted more strongly as the width of the peak approaches the angular integration increment. We plan to compute a limited number of plots similar to those of Figs. (28), (29), and (30) using 1° increments, and to compare the short wavelength behavior with that of Figures 28, 29, and 30.

Finally, it is interesting to note that, in the long wavelength limit, previous results^{8,9} based on Rayleigh scattering and absorption (dashed line) are in close agreement with those of the present theory.

3.4 Discussion.

The primary purpose of our theoretical work on scattering and absorption by cylinders has been to include ohmic losses in the historic formalism developed by Tai¹, Cassedy and Fainberg², and others. The reason for this has been to provide a useful procedure for the computation of scattering, absorption, and extinction cross sections for lossy fibers. It turns out that

essentially all of the available experimental data with which we can compare the theoretical results involves wires having a conductivity so high that, for all practical purposes, it is infinite. This is why a large portion of the data presented in this report involve infinitely conducting fibers.

The details of the various scattering patterns which we have investigated obviously depend to a very high degree upon the current function. The absorptive properties, of course, also depend upon the current function. We believe that good behavior of the scattering patterns in a given regime justifies the use of the present current function in that regime for the calculation of absorption as well as scattering. To say this in another way, a careful analysis of the scattering predictions of the theory is a powerful tool in determining where the use of the present theory is acceptable and where it is not. In addition, as mentioned in Section 3.2.3, the conservation of energy criterion ($\bar{\sigma}_{sca} + \bar{\sigma}_{abs} = \bar{\sigma}_{ext}$) also serves as an important validation tool.

With regard to the data which we have included in the preceding pages, we have the following specific comments:

- (1) The features of the differential scattering data of Sections 3.1.1 and 3.1.2 (Figs. 2 through 9) appear to be as one would expect, with the forward scattering lobe becoming more pronounced as $kh \rightarrow 10$. A somewhat disturbing feature of these data is the presence of rather larger lobes near 0° and 180° (end-on) than we expected to find. We have found, however, that, as ka is made extremely small, these lobes become smaller.
- (2) The data on backscatter cross sections is very instructive. Our predictions agree very well with the Lockheed measurements over the (rather small) range of $0.480 \leq \ell/\lambda \leq 1.051$ in Section 3.2.1 (Figs. 10 through 16).

The quantitative and qualitative details of the theory vs. measurements are in good agreement.

In Section 3.2.1 very good agreement is demonstrated between theory and experiment for the three ka values of Figs. 17 and 18. However, note that the deep minima appearing in Fig. 18 are definitely incorrect. These zeros in the backscatter cross section occur for arbitrarily small ka values, and therefore, signify zero values of $S(0)$, the forward scattering amplitude. This, in turn, forces the conclusion that the total cross section is zero at these values of kh , which cannot be.

The above problem can be directly traced to the current function of Eqs. (32), (33), and (34). If we integrate the current function over the length of the wire and set the integral equal to zero (e.g. net current = 0), we find that the relation $\tan(kh) = kh$ obtains. We have done parametric plots of this equation and find that the zeros of Fig. 18 occur precisely at the values of kh which satisfy the above transcendental equation. We should note that, in re-reading Tai's paper,¹ we found that he had discovered the same problem and produced the same transcendental equation. This is a definite limitation of the theory. Aside from this, we seem to be in good agreement with experiment. Therefore, taking this reservation into account, the theoretical backscatter data for various finite values of conductivity (Fig. 19) have high credibility.

- (3) In the case of very large values of kh , we see that the minima mentioned above persist out to at least $kh = 100$ (Section 3.3, Figs. 20 and 21), and predictions in the near vicinity of $\tan(kh) = kh$ should be disregarded. Aside from this, we find that the theory is

well behaved for extremely large values of kh for broadside scattering. An asymptotic expression for the broadside backscatter cross section vs kh was derived and is given by Eq. (35).

The calculations of differential scattering cross section vs scattering angle plotted in Figs. 26 and 27 are very well behaved and produce exactly the narrow forward scattering lobe which we expected. However, we have determined (as discussed in Section 3.3) that, within a very narrow range of ℓ/λ , a large backscatter peak occurs at all values of $\ell/\lambda = N$, where N is any large integer. Since this behavior is essentially independent of the angle of incidence, we conclude that it is incorrect and reflects a limitation of the simple current function which we are using.

- (4) The computations plotted in Figs. 32, 33, and 34 (Section 3.4) provide an example of the use of the theory which we have developed. In order to obtain accurate results in the larger kh range, we must obviously use finer angular increments in the integrations to obtain the total scattering cross sections. We have realized this for some time and are taking steps to obtain higher computational speed and more needed computer memory. It is particularly interesting to note the good agreement in the Rayleigh region between the early calculations of Pedersen and the present theory.

It is recognized that realistic calculations in the infrared and visible portions of the spectrum require the use of established optical constants (complex refractive index) and appropriate modification thereof in the very thin limit of particle radius.

In conclusion, we have found surprisingly good agreement between the theoretical predictions and available experimental data. The calculations are well behaved out to very large values of kh where we find no onset of instability. Two limitations of the theory were identified. These occupy only a very small fraction of the kh values in any given kh range and such kh values can be avoided in future computations without serious limitations of the overall information which one can obtain. We believe that theory as it now stands is, with these specific restrictions, applicable to many problems of more than passive interest to DoD.

4. RADIATIVE TRANSFER IN CONDUCTIVE FIBER CLOUDS

4.1 Basic Theory.

The purpose of the radiative transfer portion of the program is two-fold. First, we are developing a simple, efficient computer program to handle the numerical computation of radiative transfer in slabs for a wide range of scattering/absorbing particle parameters, and for quite general particles. Second, we are integrating the RT program with a computer program that treats the scattering and absorption specifically by lossy conductive fibers, in order to determine the overall electromagnetic behavior of such configurations.

The basic RT theory has been described earlier.^{10,11} Essentially, we are using the van de Hulst doubling method with a Taylor series representation for the starting (thin-layer) values of the transmission and reflection matrices, including up to fourth-power terms in the optical depth. This innovative treatment of starting values enables us to avoid the cumulative error build-up incurred when one begins with infinitesimal starting layer thicknesses.

In brief, the theory runs as follows. In order to interpret the transmission and reflection matrices, which are the basic quantities computed, consider Fig. 31. The layer of optical depth x contains a cloud of randomly oriented and positioned fibers (or other scattering particles). Radiation is incident from outside the layer, and we characterize the right-going and left-going parts at any point in the layer by u and v , respectively. The spatial direction variable has been discretized, so that more specifically u is an N -component column vector giving the angular distribution of radiation into the right hemisphere, and similarly for v . Now $u(0)$ represents radiation incident on the front face of the layer, giving rise to transmitted intensity

$$u(x) = T u(0) \quad (43)$$

and reflected intensity

$$v(0) = R u(0), \quad (44)$$

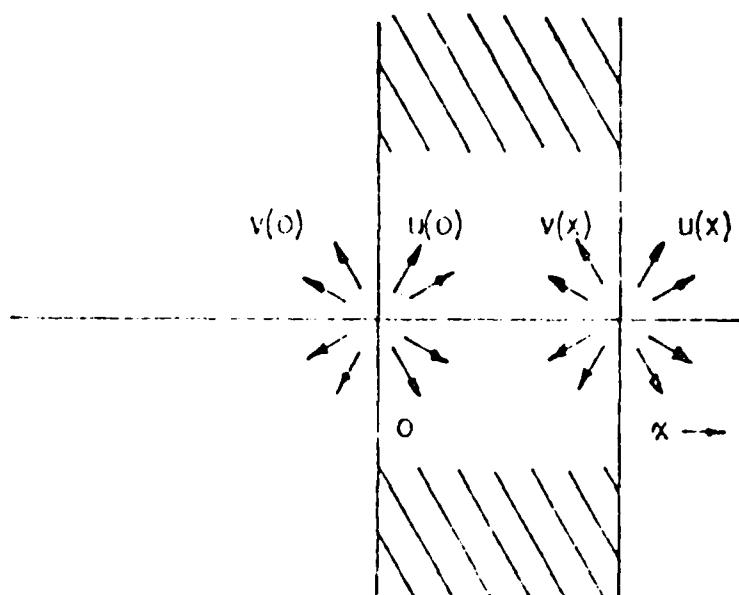


Figure 31. Discretized Right-Going (u) and Left-Going (v) Radiation.

both of which can be computed once the transmission and reflection matrices T and R are known.

One begins by evaluating T and R numerically for a layer very thin compared with optical depth, i.e., $x \ll 1$, using the formulas

$$\begin{aligned}
 T \approx & 1 - Q_1 x + (1/2!) (Q_1^2 + Q_2^2) x^2 \\
 & - (1/3!) (Q_1^3 + Q_2 Q_1 Q_2 + 2 Q_1 Q_2^2 + 2 Q_2^2 Q_1) x^3 \\
 & + (1/4!) (Q_1^4 + Q_2 Q_1^2 Q_2 + 3 Q_1^2 Q_2^2 + 3 Q_2^2 Q_1^2 \\
 & + 3 Q_1 Q_2 Q_1 Q_2 + 3 Q_2 Q_1 Q_2 Q_1 + 5 Q_2^4 + 5 Q_1 Q_2^2 Q_1) x^4, \quad (45)
 \end{aligned}$$

$$\begin{aligned}
 R \approx & Q_2 x - (1/2!) (Q_1 Q_2 + Q_2 Q_1) x^2 \\
 & + (1/3!) (Q_1^2 Q_2 + Q_2 Q_1^2 + 2 Q_2^3 + 2 Q_1 Q_2 Q_1) x^3 \\
 & - (1/4!) (Q_1^3 Q_2 + Q_2 Q_1^3 + 3 Q_1 Q_2 Q_1^2 + 3 Q_1^2 Q_2 Q_1 \\
 & + 3 Q_2 Q_1 Q_2^2 + 3 Q_2^2 Q_1 Q_2 + 5 Q_1 Q_2^3 + 5 Q_2^3 Q_1) x^4. \quad (46)
 \end{aligned}$$

These equations give a particularly compact method for obtaining T and R to high accuracy; the scattering behavior of the fibers themselves enters in the determination of the quantities Q_1 and Q_2 , which are defined explicitly in terms of the single fiber scattering pattern.¹⁰

Having obtained T and R for the thin layer, the corresponding values for layers of arbitrary optical depth are now computed by successive applications of the doubling equations. Writing $T_2 = T(2x)$, $R_2 = R(2x)$, one has

$$T_2 = T (1 - R^2)^{-1} T, \quad (47)$$

$$R_2 = R + TR (1 - R^2)^{-1} T. \quad (48)$$

There are thus one matrix inversion and several multiplications required at each stage of doubling. The starting layer thickness should be chosen judiciously in order to optimize the accuracy of the computation; note that the smaller the initial choice for x , the more accurate will be the starting values for T and R from Eqs. (45) and (46) but, on the other hand, the more repetitions of the doubling equations that will be required, with attendant loss of precision, in order to attain a given optical depth. Numerical trials have been carried out which ensure that we work with near-optimum starting depths.

For the discretization of the radiative transfer equation we have employed the extended Simpson's 3/8 rule, which can be derived without difficulty from the ordinary 3/8 rule available in the literature.¹² As the extended rule is not too well known, we state it here:

$$\begin{aligned} \int_a^b dz f(z) = (3h/8) & \left[f(z_0) + 3 f(z_1) + 3 f(z_2) \right. \\ & \left. + 2 f(z_3) + 3 f(z_4) + \cdots + f(z_{3s}) \right] + R_{3s}. \end{aligned} \quad (49)$$

The range of integration is divided into $3s$ intervals each of width h , where $h = (a-b)/3s$, and we choose s odd, so that $3s = 3, 9, 15, 21, \dots$. The remainder term can be estimated by

$$R_{3s} = -(h^4/80) [f^{(iii)}(b) - f^{(iii)}(a)] \quad (50)$$

in terms of the third derivatives of the integrand at the end points.

In the present application, z is identified with $\mu = \cos \theta$, where θ is the angle formed by the radiation flux with the forward direction (x axis in Fig. 31). Thus, T and R will determine radiation patterns over the discrete set of directions having uniform increments in $\cos \theta$. The extended $3/8$ rule enables us to avoid the equatorial direction $\theta = \pi/2$, which can cause numerical difficulties. It also permits us to readily adjust the grid spacing in $\cos \theta$, something which is not possible with the more commonly employed Gaussian quadrature, because of the complexity of determining weighting coefficients and ordinates in the latter.

4.2 The Phase Function.

The basic single-particle inputs needed to the RT computer program are the albedo

$$\alpha = \frac{\text{scattering cross-section}}{\text{extinction cross-section}} \quad (51)$$

and the phase function $p_0(\mu, \mu')$, obtained by simply integrating the scattered power $p(\mu, \theta, \mu', \theta')$ over all azimuths θ, θ' . Here $\mu = \cos \theta$ and θ are the angles of incidence, and $\mu' = \cos \theta', \theta'$ the angles of observation.

There are two ways of proceeding, depending on whether or not analytical expressions are available for the phase function. The two simplest analytical cases are¹³

$$P_0(\mu, \mu') = 1 \quad (\text{Isotropic}) \quad (52)$$

and

$$P_0(\mu, \mu') = \frac{3}{4} [1 + \mu^2 \mu'^2 + \frac{1}{2} (1 - \mu^2)(1 - \mu'^2)], \quad (\text{Rayleigh Sphere}) \quad (53)$$

$$P_0(\mu, \mu') = \frac{3}{4} [1 + \mu^2 \mu'^2 + \frac{1}{2} (1 - \mu^2)(1 - \mu'^2)], \text{ (Rayleigh Sphere)} \quad (53)$$

the latter being appropriate for small conducting spheres with unpolarized incident radiation. These cases are useful for verifying the validity and accuracy of the computer program; numerical results are readily available for them in the literature.

In the absence of analytical expressions the phase function must be handled in tabular form. Following Ishimaru,¹³ this is done as follows. For inputs we employ the single-scatterer intensities $S(\mu_i)$ evaluated at $(3s + 1)$ equally-spaced points in μ . The reflection and transmission matrices R and T will each have dimensions $(3s + 1)/2 \times (3s + 1)/2$. Note that $S(\mu)$ represents the scattered intensity averaged over all scatterer orientations, for incidence in the direction $\mu = \mu_1 = 1$ (the forward direction).

The phase function can now be determined from

$$P_0(\mu, \mu') = \sum_{m=0}^M W_m P_m(\mu) P_m(\mu') \quad , \quad (54)$$

in terms of the Legendre polynomials P_m . The latter are determined in standard fashion using a recursion sub-routine based on the formulas

$$\begin{aligned} P_0 &= 1 \\ P_1 &= \mu \quad , \end{aligned}$$

and

$$P_{m+1}(\mu) = \left(\frac{1}{m+1} \right) \left[(2m+1)\mu P_m(\mu) - m P_{m-1}(\mu) \right] \quad . \quad (55)$$

The constants W_m are given by

$$W_m = \left(\frac{2}{2m+1} \right) \int_{-1}^{+1} d\mu P_m(\mu) S(\mu) \quad , \quad (56)$$

and the summation of Eq. (54) is terminated when the W_m become negligible. The integral of Eq. (56) is approximated using Simpson's 3/8 rule, Eq. (49), with grid spacing $h = 2/3s$.

The doubling method can now be applied to obtain the reflection and transmission matrices for layers of any desired optical length. In order to obtain physical results, matrix elements must then be weighted appropriately to allow for the specific quadrature rule employed. If we define normalizing constants

$$c(n) \equiv (a_n \mu_n)^{\frac{1}{2}}, \quad n = 1, 2, \dots, \frac{1}{2}(3s+1), \quad (57)$$

where the a_n are the 3/8-rule weighting coefficients, then the net fluxes reflected in the back hemisphere, or transmitted in the forward hemisphere, are given respectively by

$$\begin{aligned} \bar{R} &= \frac{1}{c(1)} \sum_{n=1}^{\frac{1}{2}(3s+1)} R(n,1) c(n) \\ \bar{T} &= \frac{1}{c(1)} \sum_{n=1}^{\frac{1}{2}(3s+1)} T(n,1) c(n) . \end{aligned} \quad (58)$$

These equations are for radiation incident normally on the slab, which explains why only the first columns of R and T are needed. For isotropically incident radiation, all elements of R and T would come into play. For the angular intensity patterns, on the other hand, one has

$$\begin{aligned} \hat{R}(n) &= R(n,1)/2 c(1)c(n) , \\ \hat{T}(n) &= T(n,1)/2 c(1)c(n) , \quad n = 1, 2, \dots, \frac{1}{2}(3s+1) . \end{aligned} \quad (59)$$

4.3 Orientation Averages.

For the conductive fibers, the first step in the analysis involves orientation averaging of the single-fiber differential scattering patterns. If $p(\alpha, \beta)$ is a unit vector along the fiber axis, with spherical angles α, β relative to a fixed cartesian coordinate system, for a linearly polarized incident wave e_{in} along the positive z direction we have $\sigma_{diff} = \sigma_{diff}(\alpha, \beta, \theta, \phi)$, and the orientation-averaged differential scattering pattern is given by

$$\bar{\sigma}_{diff}(\theta) = \left(\frac{1}{4\pi}\right) \int_0^{2\pi} d\alpha \int_0^\pi d\beta \sin\beta \sigma_{diff}(\alpha, \beta, \theta, \phi) \quad (60)$$

Note that strictly speaking it is necessary to also average over the polarization angles of the incident and scattered waves. Because we are only interested in scalar intensities, however, it suffices to choose the incident polarization in the plane of incidence (plane formed by the fiber and the direction of incidence). The scattered intensity is then taken without regard to its polarization. It is not difficult to verify that this simplification does not affect the angular dependence of the result.

The scattering patterns are actually computed in fiber coordinates, i.e., in terms of the angle $\cos \theta_f = p \cdot k_{out}$ formed by the fiber and the observation direction $k_{out}(\theta, \phi)$. The angle θ_f can be expressed in terms of the orientation angles by noting that

$$\cos \theta_f = \sin \theta \sin \beta \cos(\phi - \alpha) + \cos \theta \cos \beta. \quad (61)$$

We see that the ϕ -dependence drops out during the integration, so that the resulting pattern, Eq. (60), is rotationally symmetric.

The short-fiber limit $kh \ll 1$ (h = half-length of fiber) provides a useful check on the computation. In this limit we can assume that the axial current induced in the fiber is proportional to $e_{in} \cdot p = \sin \beta$ and that the corresponding scattered amplitude is given by $e_{in} \cdot p \sin \theta_f$, so that

$$\sigma_{\text{diff}} = \sigma_0 (\hat{e}_{\text{in}} \cdot \hat{p} \sin \theta_f)^2, \quad (62)$$

where σ_0 is the maximum cross section obtained at broadside incidence and observation. Putting this expression in Eq. (60), and dividing by a factor of 4 to correct for not averaging over incident and received polarization, gives finally

$$\bar{\sigma}_{\text{diff}}/\sigma_0 = (1/30) (3 + \cos^2 \theta). \quad (63)$$

This $3 + \cos^2 \theta$ angular dependence constitutes a new elementary scatterer for radiative transfer, which might be called the Rayleigh fiber. Note that it falls intermediate relative to the isotropic and Rayleigh sphere ($1 + \cos^2 \theta$) cases.

Numerical computations of orientation-averaged scattering from perfectly conducting fibers are shown in Fig. 32 for several values of kh (for clarity normalized to 4 in the forward direction $\mu = \cos \theta = 1$). The uppermost curve is the Rayleigh fiber pattern of Eq. (63), and one notes that the numerical results converge smoothly to this limit for $kh \ll 1$ (the $kh = 0.1$ curve, not shown, is indistinguishable). As kh becomes greater than unity a significant peak is seen to develop in the forward direction, typical behavior for scatterers when dimensions are not small compared to wavelength.

It is interesting to note that the orientation-average has been computed by Borison, but for half-wave dipoles ($kh = \pi/2$).¹⁴ Upon averaging his results over incident and received polarizations one obtains precisely Eq. (63). This does not agree with the curve of Fig. 32; we believe that Borison's assumption of simple cosine behavior of the surface current for all fiber orientations is no longer adequate at $kh = \pi/2$.

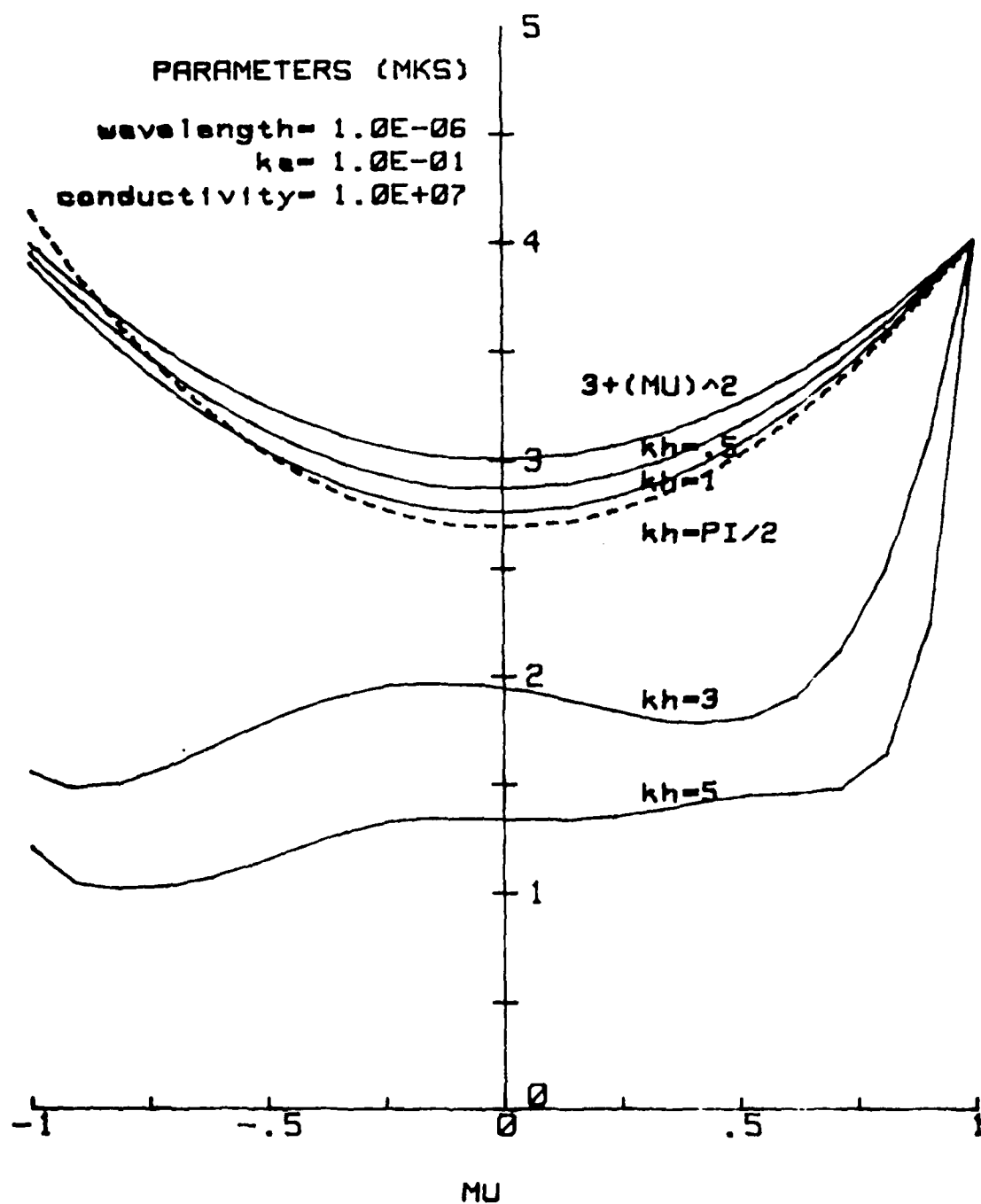


Figure 32. Orientation-Averaged Differential Cross Sections

4.4 The Thin-Layer Limit.

Now consider the slab geometry for a cloud of randomly oriented fibers, as shown in Fig. 33. The cloud has optical depth x , and one desires to compute the angular intensities transmitted and reflected, $T(\theta)$ and $R(\theta)$, respectively, as shown in the figure.

A simple check is available on numerical computations in the thin-layer limit $x \ll 1$. As shown in Fig. 34, the transmitted intensity per steradian in the direction $\mu = \cos \theta$ must originate in the differential cone of fibers indicated. But, in the thin-layer limit, the contribution from an element of the cone will be proportional to albedo a , the phase function $p(\mu)$, and exponential factors accounting for attenuation of radiation over the travel path within the slab. Thus, with $x' = x - \mu s$,

$$I(\mu) = \kappa a p(\mu) \int_0^{x/\mu} ds e^{-x'} e^{-s}, \quad \mu \geq 0. \quad (64)$$

A similar equation can be written down for the reflected intensity, and carrying out the integrations gives

$$I(\mu) = \kappa a p(\mu) \begin{cases} e^{-x} (1 - e^{-(1-\mu)x/\mu}) / (1-\mu), & \mu \geq 0 \\ (1 - e^{(1-\mu)x/\mu}) / (1-\mu), & \mu \leq 0 \end{cases} \quad (65)$$

These last formulas are given by van de Hulst¹⁵ for the isotropic case $p(\mu) = 1$; clearly, from our derivation they must continue to hold for arbitrary $p(\mu)$.

Intensity patterns have been computed numerically for an optical depth $x = 0.1$ and the three elementary scatterers, isotropic, Rayleigh sphere (dipole), and Rayleigh fiber. Results

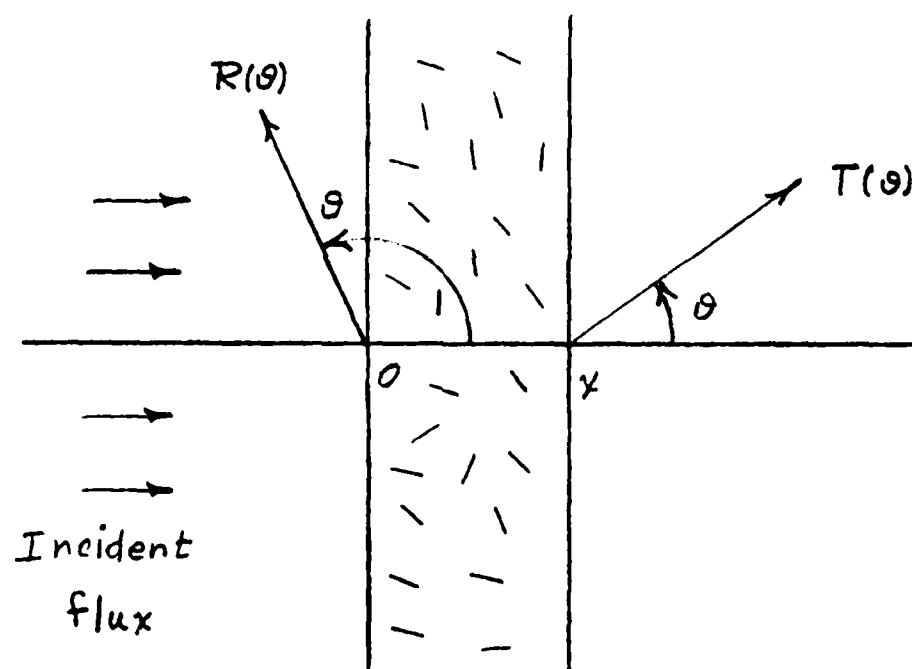


Figure 33. Slab Geometry of Fiber Cloud

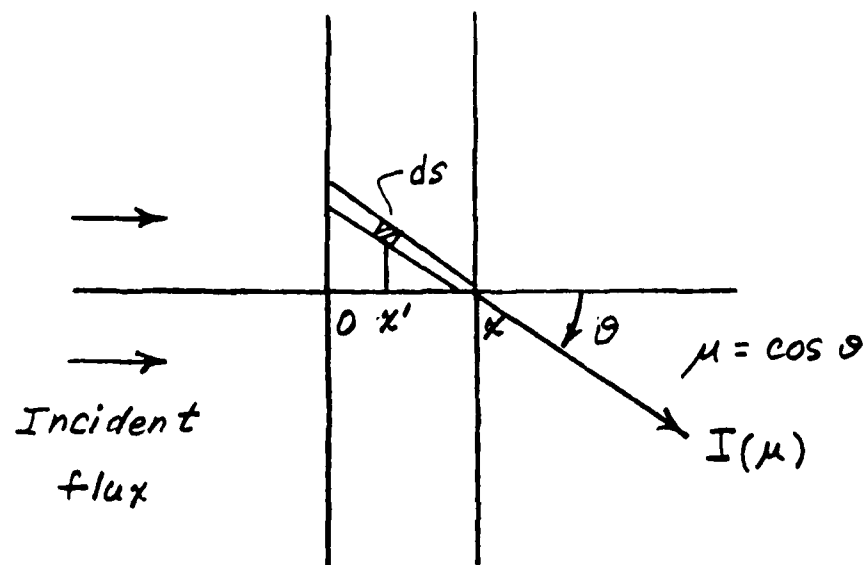


Figure 34. Geometry for Thin-Layer Approximation

are shown by the points in Fig. 35. The corresponding analytical approximations of Eq. (65) are given by the solid curves in the figure, and excellent agreement is seen throughout. Incidentally, van de Hulst gives the theoretical value $\kappa = 1/4$ for the proportionality constant of Eqs. (64) and (65). We find that much better results are obtained using a somewhat larger value obtained by matching Eq. (65) to the computed point for normal reflection for transmission ($\mu = \pm 1$). For example, for isotropic scatterers the two computations then agree to four significant figures, excepting only the point $\mu = -.04762$, where agreement is slightly poorer.

4.5 Numerical Results.

A plotter routine has been developed for the reflected and transmitted intensity patterns, and some typical results will now be shown for normal incidence on slabs of optical thickness x .

In Fig. 36 angular patterns are shown versus observation direction $\mu = \cos \theta$ for lossless isotropic scatterers. For this case $s = 9$, and R and T are of dimension 14×14 . Note that our quadrature scheme avoids the equatorial plane $\mu = 0$, where analytical difficulties arise (the curves are easily extrapolated if desired, however). In the transmitted patterns the coherent field, that portion of the originally incident beam which has survived, is represented by a discrete version of the delta function (sharply rising curves near $\mu = 1$, truncated at unit intensity for clarity). As was observed earlier¹¹ these results, including the discrete delta function contribution, exactly satisfy energy balance constraints.

The same computation is carried out in Fig. 37, but for much coarser grid spacing (matrix dimension 5×5). Aside from the obvious change in the discrete delta function contribution, these curves are seen to be effectively identical with those of Fig. 36. This demonstrates the stability of the computer

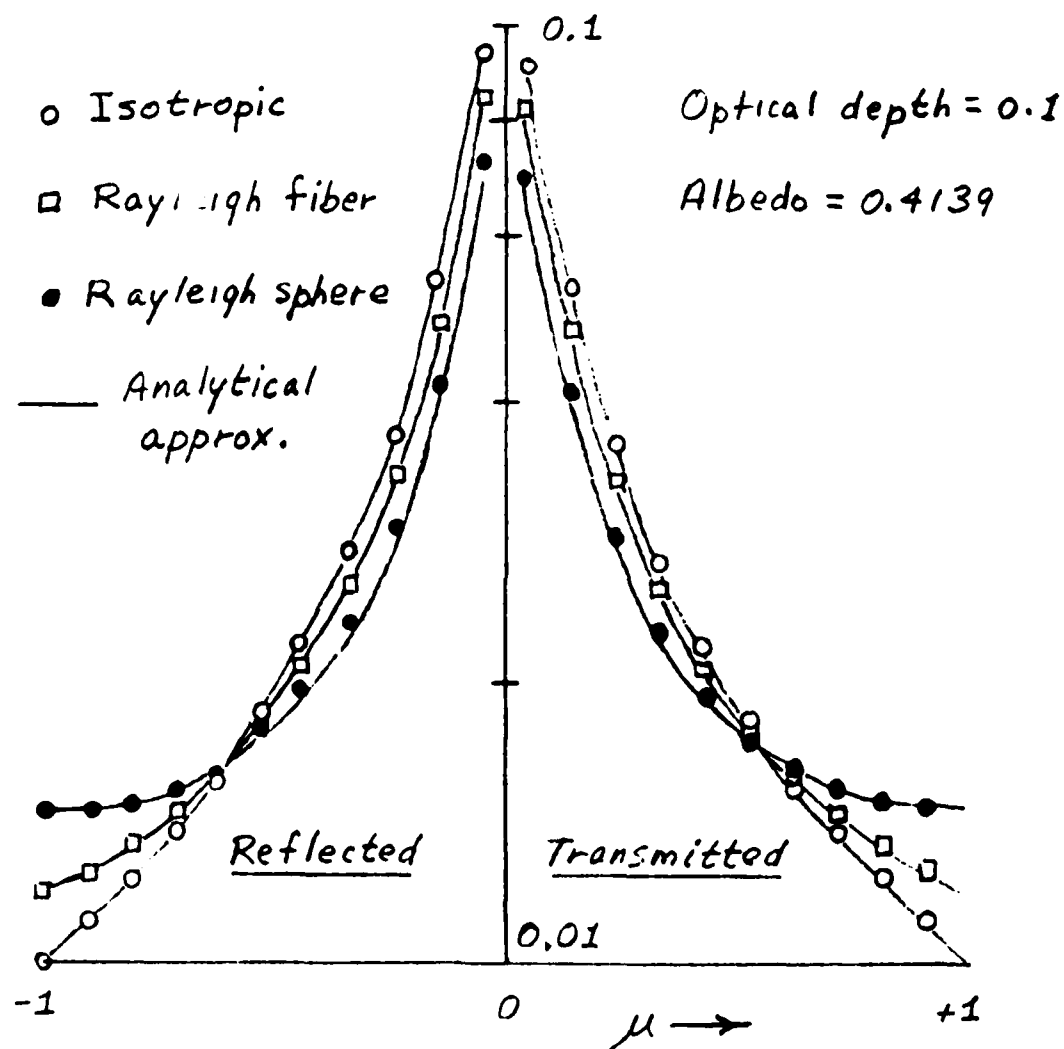


Figure 35. Thin-Layer Flux Distributions

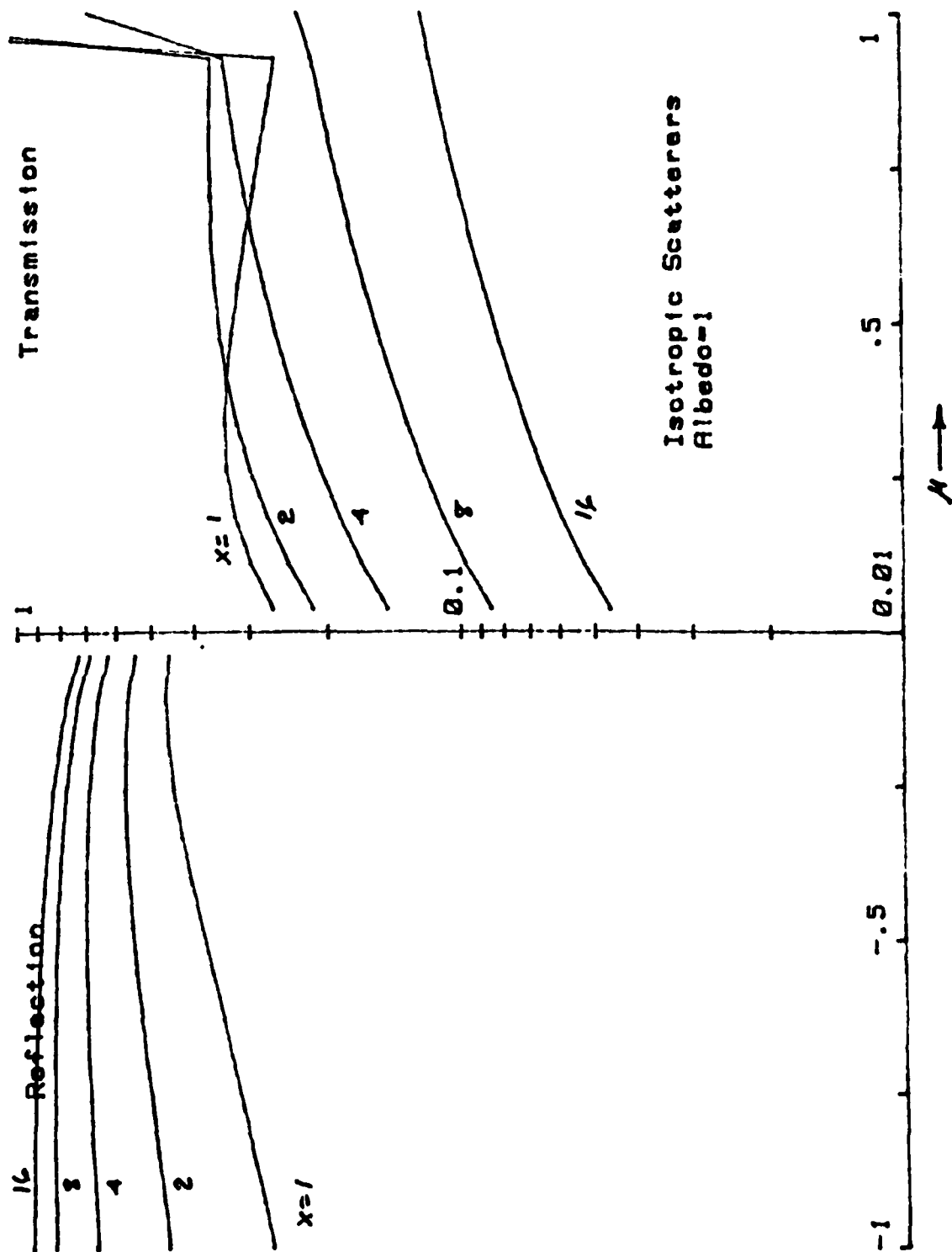


Figure 36. Angular Flux Patterns for Lossless Isotropic Scatterers

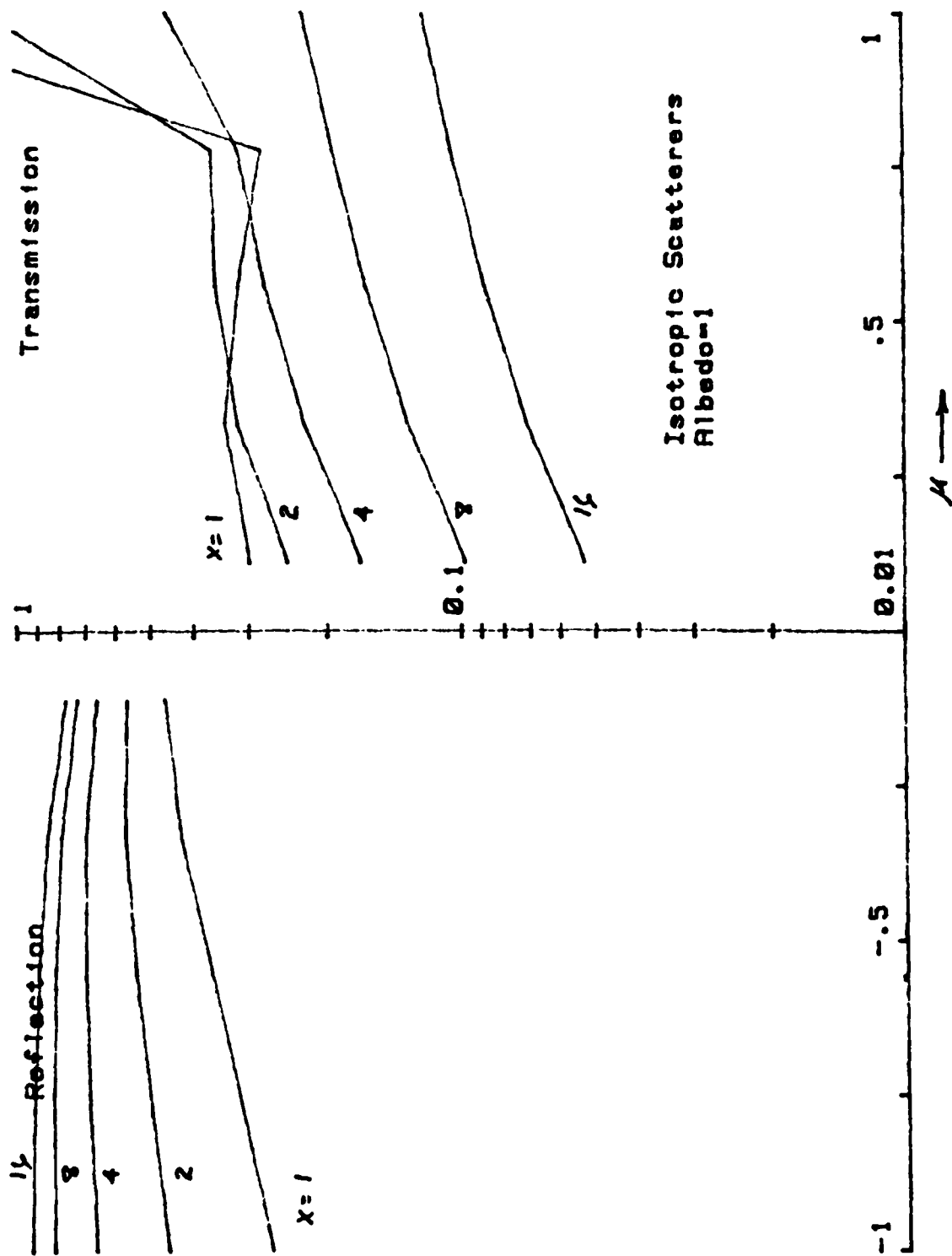


Figure 37. Angular Flux Patterns with Coarser Grid Spacing

program with respect to grid spacing at least for this simple case, and also confirms the ease with which grid spacing can be adjusted to fit the problem at hand.

In Figs. 38 and 39 (albedo = 0.8, 0.5 respectively) losses are introduced, with corresponding reduction in the intensities. For all of these results, checks with the numerical tables of van de Hulst¹⁵ give excellent agreement.

Figures 40, 41 and 42 show the intensity distributions obtained using the Rayleigh phase function of Eq. (53), and albedos of 1.0, 0.8, . 0.5. Note that there is not too much difference from the isotropic case. The Rayleigh case differs in that single particle scattering is now more concentrated in the forward and back directions. In terms of scattering angle θ , the single-particle intensity is given by¹³

$$\frac{3}{4} (1 + \cos^2 \theta) . \quad (66)$$

the effect of this is evident when one compares the reflection curves, which have become relatively somewhat larger in the back direction ($\mu = -1$), although not much change has occurred in the transmission curves.

In Fig. 43 plots of the transmitted and reflected intensities are given for an optical depth of unity, where the single scatterer is 1) isotropic, 2) Rayleigh sphere, 3) the Rayleigh fiber of Eq. (63), and 4) the short fiber (parameters as noted in the figure). Note that, just as was true for the phase functions, the radiative transfer intensities for the Rayleigh fiber fall intermediate between the isotropic and sphere case. It is also interesting that the Rayleigh fiber and short dipole ($kh = 0.5$) results are now indistinguishable, even though their phase functions are measurably different (see Fig. 32).

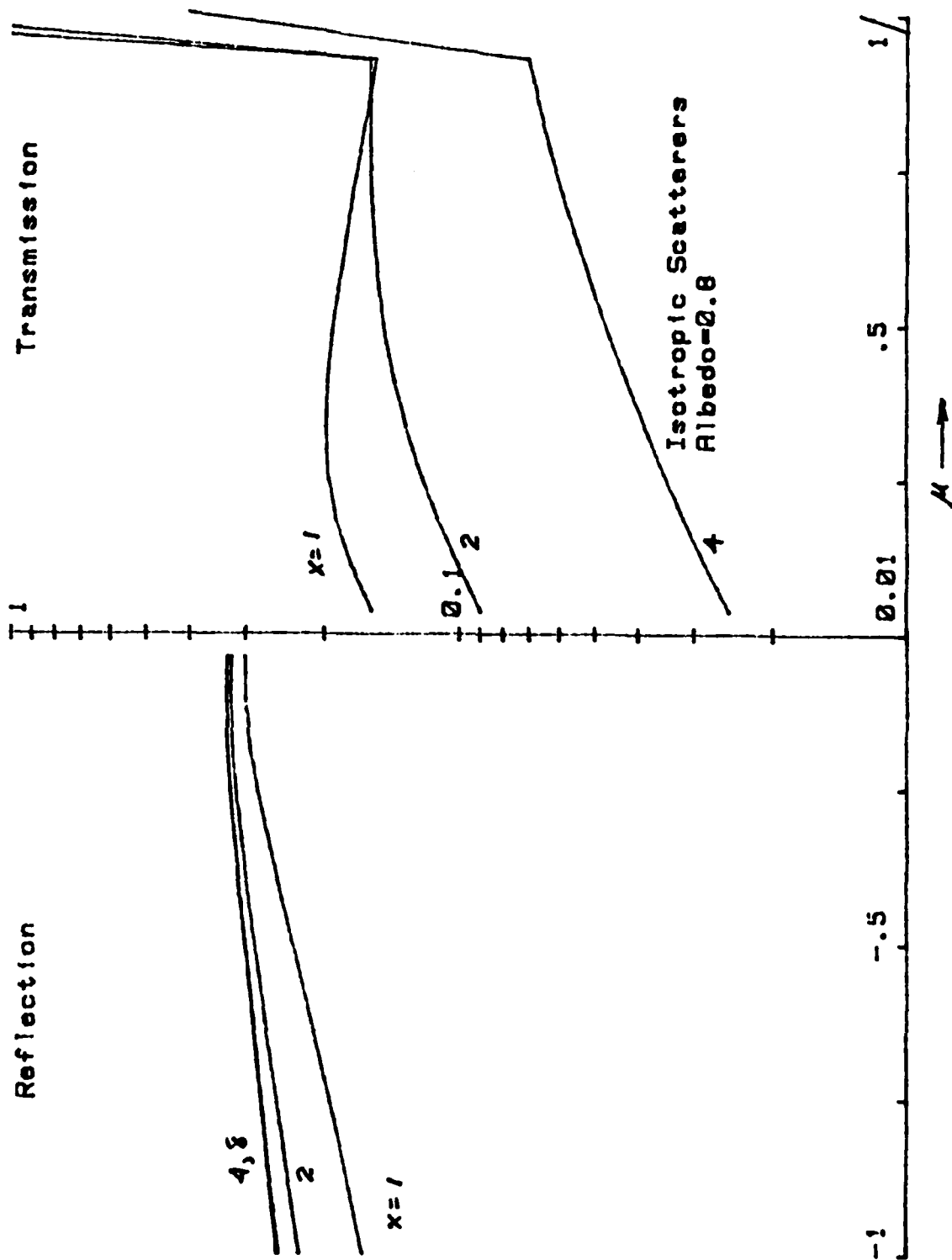


Figure 38. Angular Flux Patterns ($\alpha = 0.8$)

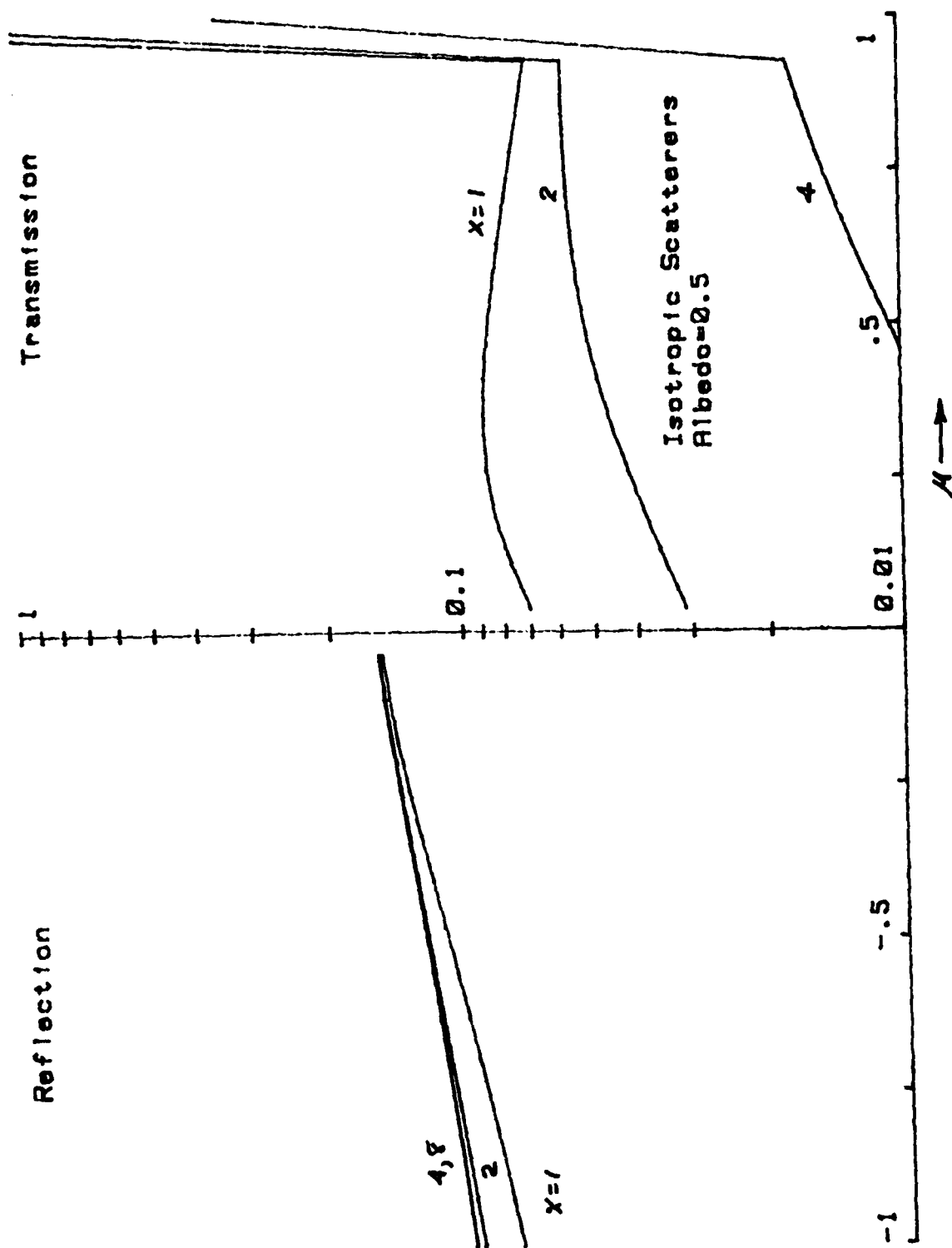


Figure 39. Angular Flux Patterns ($\alpha = 0.5$)

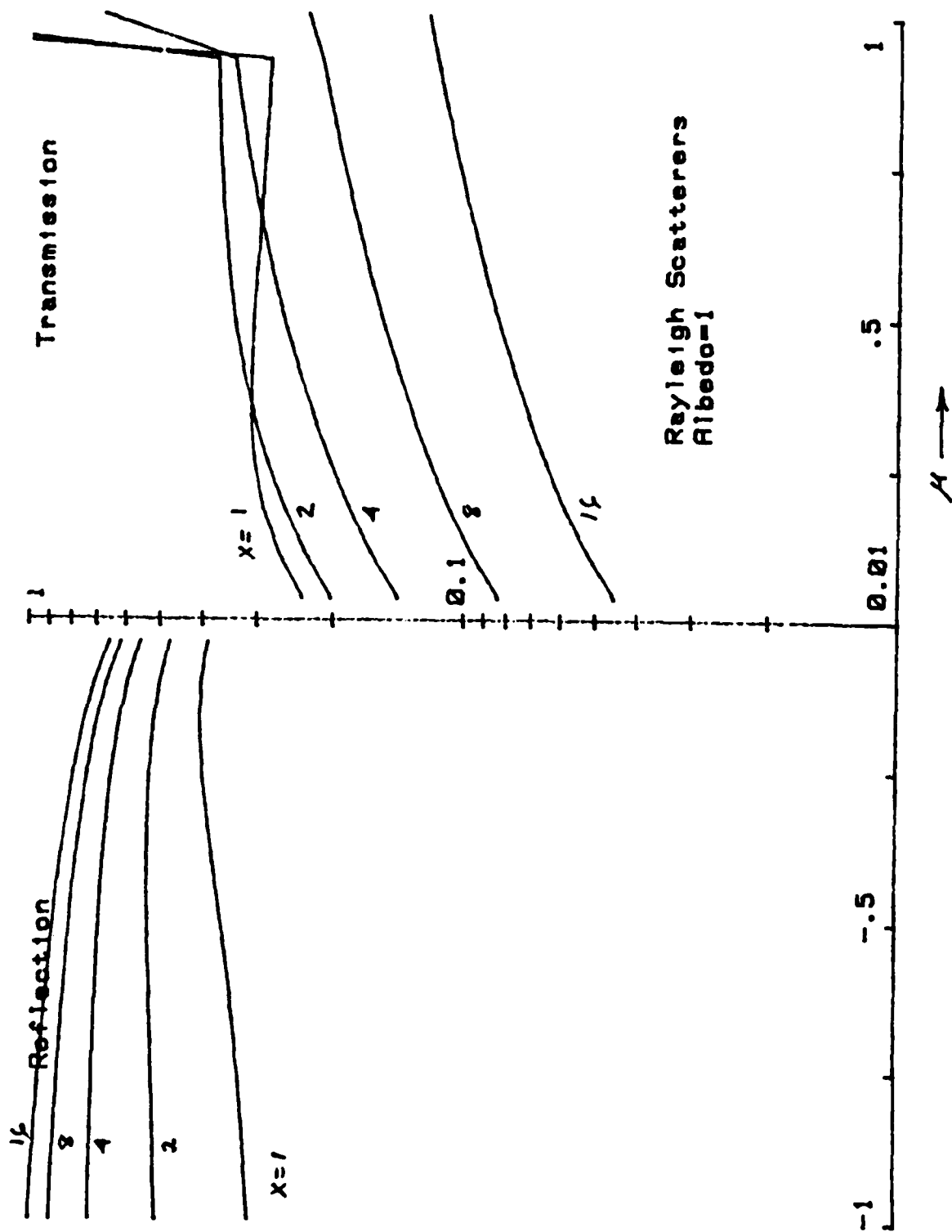


Figure 40. Angular Flux Patterns for Rayleigh Spheres ($a = 1$)

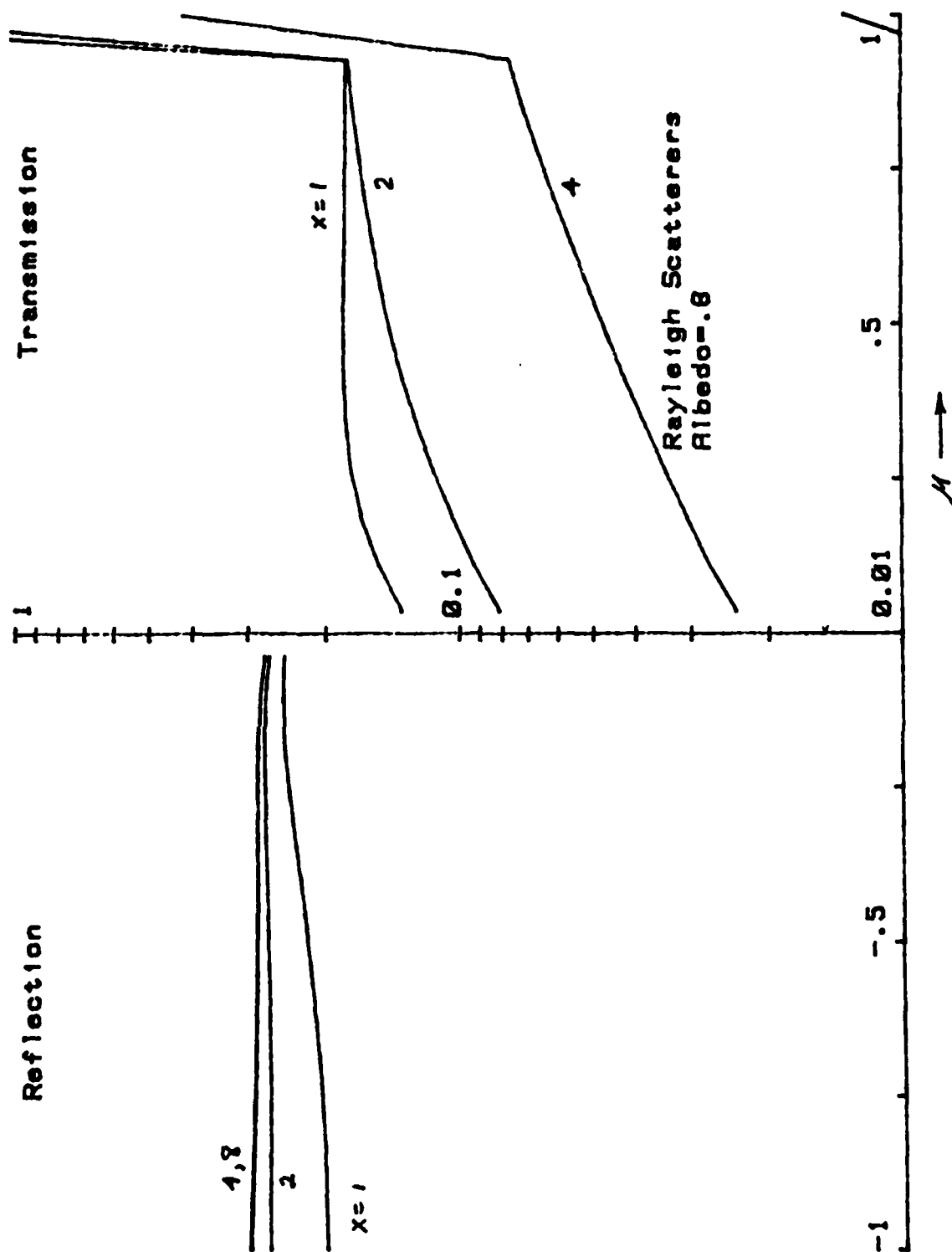


Figure 41. Angular Flux Patterns for Rayleigh Spheres ($\alpha = 0.8$)

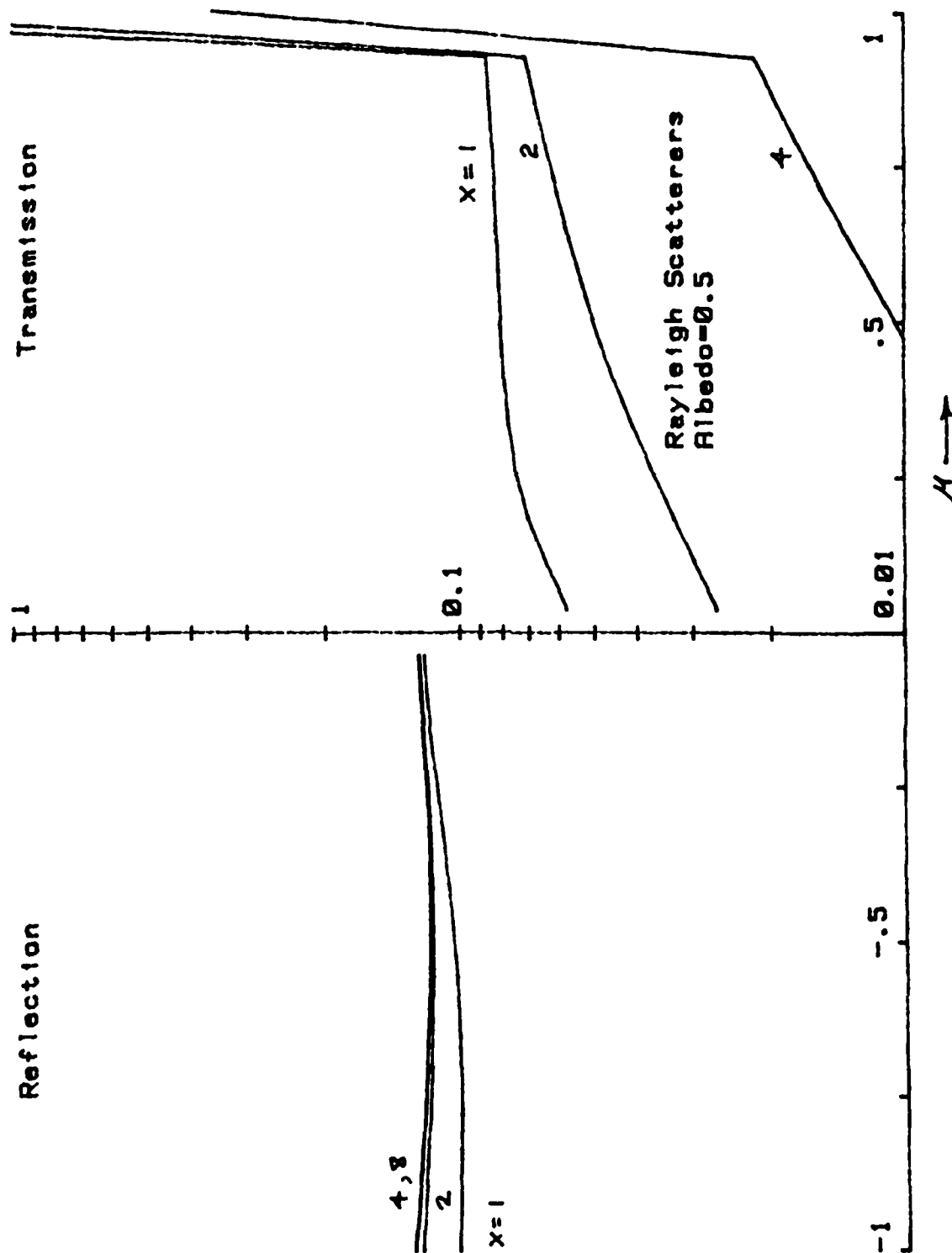


Figure 42. Angular Flux Patterns for Rayleigh Spheres ($\alpha = 0.5$)

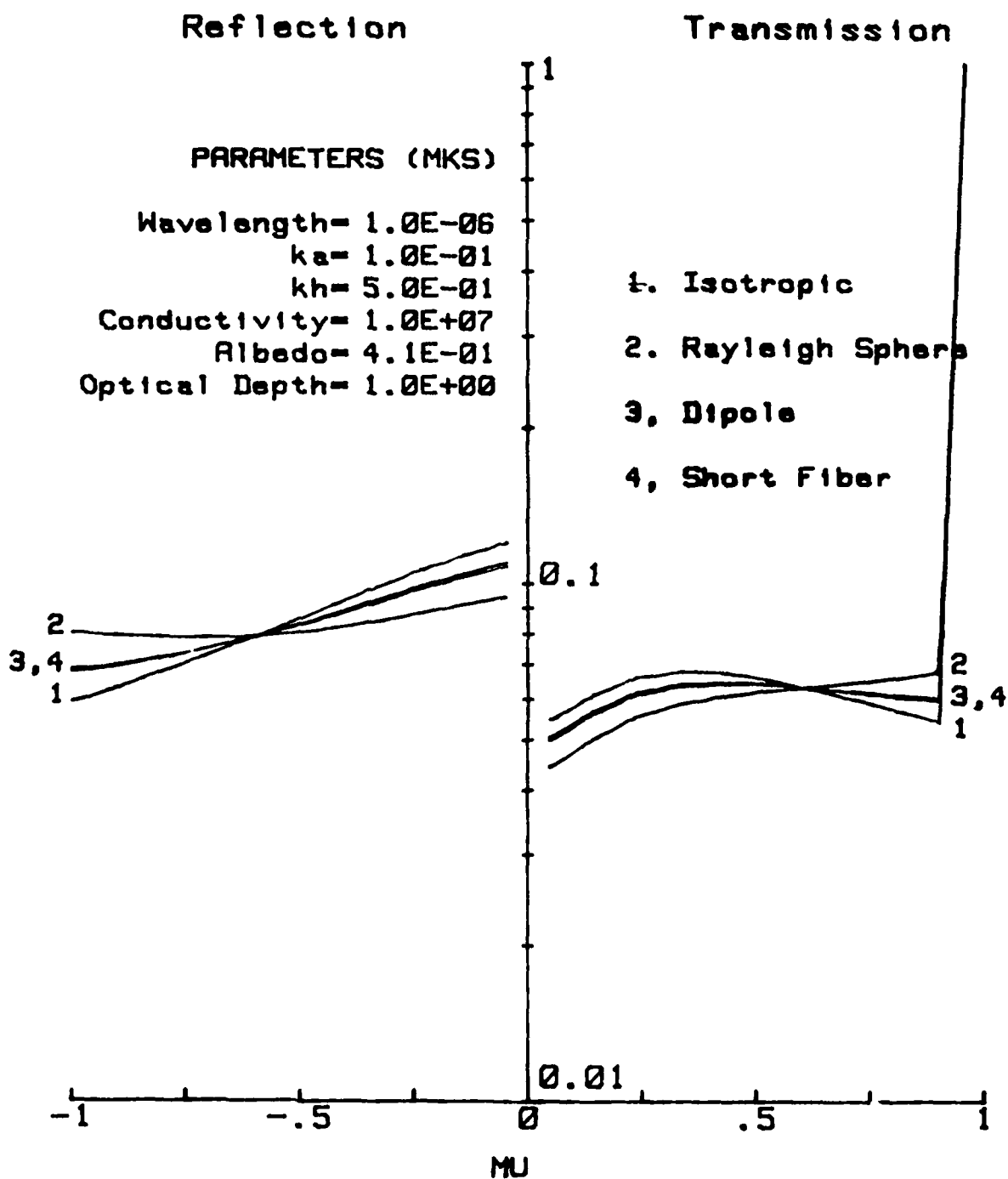


Figure 43. Angular Flux Patterns for Various Scatterers

Dependence of the RT intensities on fiber length is indicated in Fig. 44, for fairly highly conducting fibers. From the figure one can see that both the transmitted and reflected intensity, integrated over all angles as in Eq.(58), show a mild peak at about $kh = 3$, although the reason for this is not clear.

For fixed fiber length $kh = 3$, dependence of the RT intensities on optical depth x is shown in Fig. 45. As one would expect, the reflected patterns increase monotonically with x , at the same time becoming more nearly isotropic. The transmitted patterns show the same behavior in the diffusely transmitted flux up to about $x = 1$, with corresponding reductions in the coherent flux (because of truncation the latter effect is not obvious from the figure). With further increases in optical depth the transmitted flux begins to decrease, presumably because scattering and absorption mechanisms now dominate.

Finally, Fig. 46 illustrates the effect of varying the fiber conductivity, maintaining a fixed fiber length $kh = 1$ and optical depth $x = 1$. Both reflected and transmitted patterns are seen to increase monotonically with conductivity, both also showing signs of saturation for the uppermost curves, which are effectively approaching the perfectly conducting limit. Again, the curves behave qualitatively as would be expected, in view of the fact that the albedo is increasing toward unity with increasing conductivity.

The above examples illustrate the usefulness and versatility of the computer programs. These programs are now sufficiently well developed to begin running specific problems of practical interest to CRDC involving both single fiber scattering and absorption, and the radiative transfer properties of the corresponding fiber clouds.

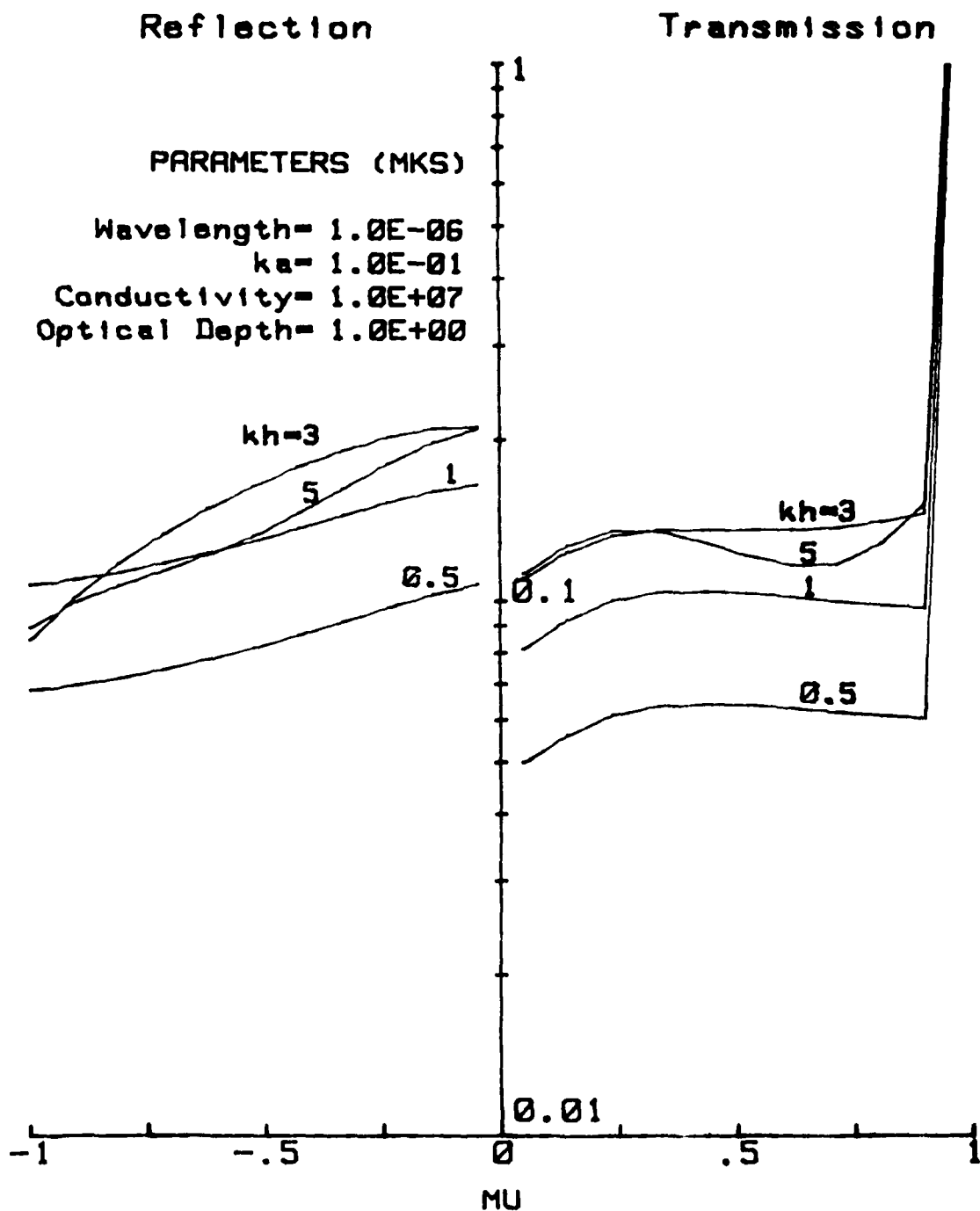


Figure 44. Angular Flux Patterns for Various Fiber Lengths

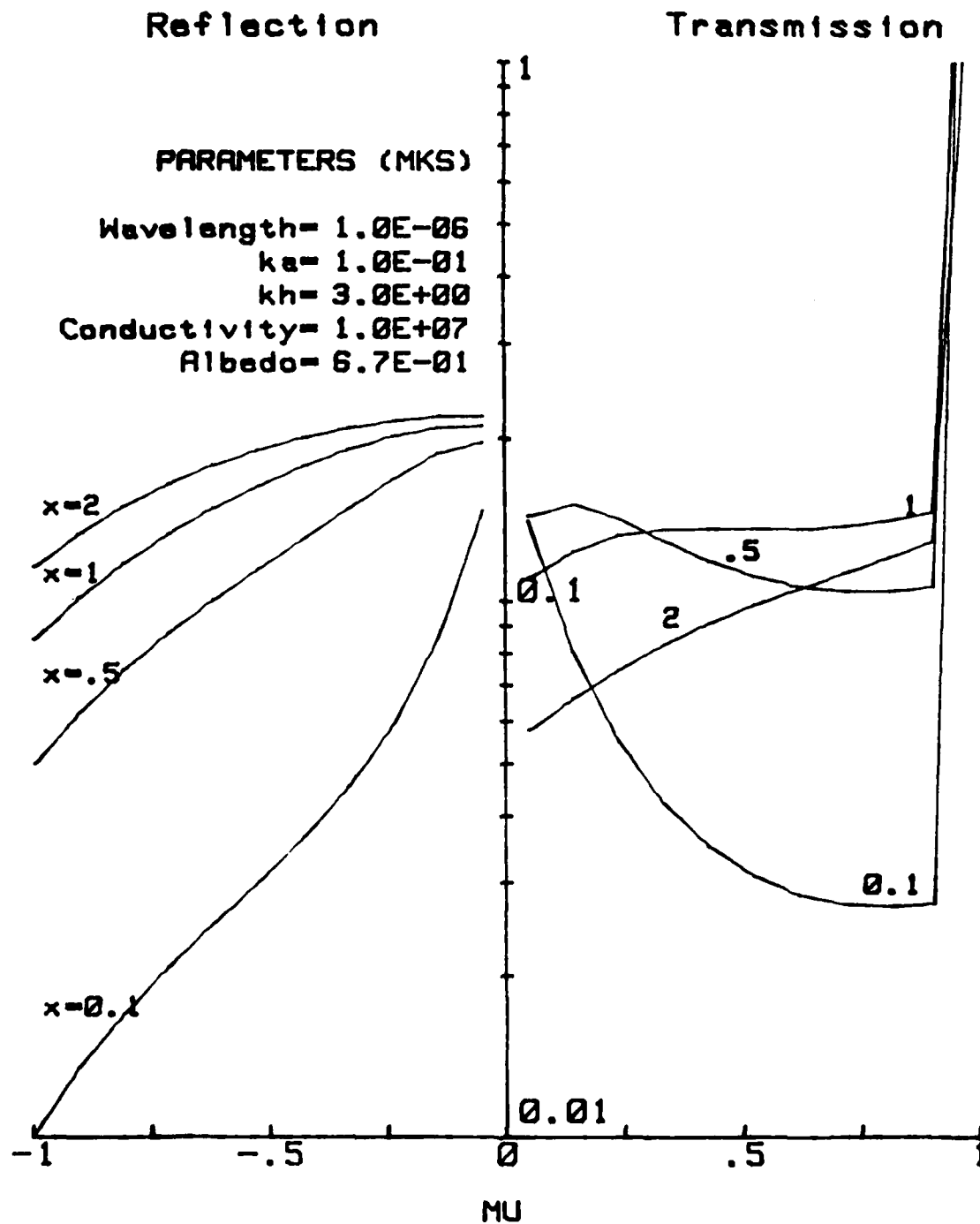


Figure 45. Angular Flux Patterns for Various Optical Depths

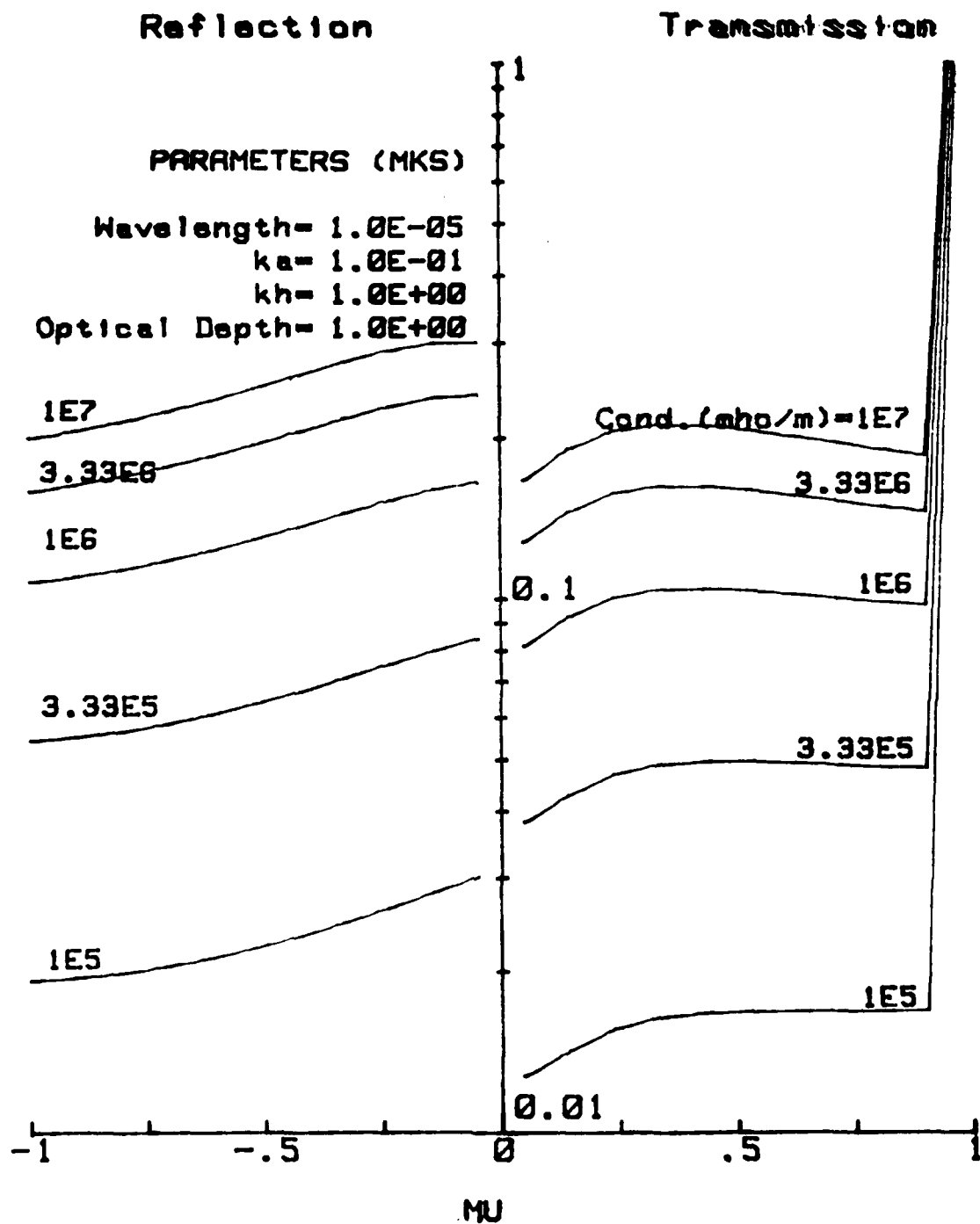


Figure 46. Angular Flux Patterns for Various Conductivities

References

1. C. T. Tai. Electromagnetic Backscattering from Cylindrical Wires. J. Appl. Phys., 23, 909-916 (August, 1952).
2. E. S. Cassedy, and J. Fainberg. Electromagnetic Cross Sections of Finite Conductivity. The Johns Hopkins Laboratory Technical Report No. AF-81. August 1960.
3. J. R. Wait. Exact Surface Impedance for a Cylindrical Conductor. Electr. Lett. 15, 659-660 (1979).
4. N. E. Pedersen, J. C. Pedersen and P. C. Waterman. Theoretical Investigation of Absorptive Processes. Final Report for Period 1 April 1979 - 1 April 1981. Prepared for Army Research Office and US Army Research and Development Command (May, 1981). DAAK11-81-C-0067.
5. J. R. Webb. Radar Backscatter Measurements for Tungsten and Copper Dipoles. Report No. ER-6984, (June 1, 1964).
6. B. O. As, and H. J. Schmitt. Back-Scattering Cross Section of Reactively Loaded Cylindrical Antennas. Scientific Report No. 18. Cruft Laboratory, Harvard University (August, 1957).
7. R. W. King, and T. T. Wu. The Scattering and Diffraction of Waves. p 161. Harvard University Press, Cambridge, MA 1959.
- 8.
- 9.
10. P. C. Waterman. Matrix-Exponential Description of Radiative Transfer. J. Opt. Soc. Am. 71, 410-422 (1981).
11. N. E. Pedersen, P. C. Waterman, and J. C. Pedersen. Final Report on Theoretical Investigation of Absorptive Properties. Panametrics, Inc. December 21, 1982.
12. M. Abramowitz, and I. A. Stegun, Eds. Handbook of Mathematical Functions. (NBS). p 886. Dover Publishing, New York, NY 1965.
13. A. Ishimaru. Wave Propagation and Scattering in Random Media. Vol. 1, p 205. Academic Press, New York, NY 1978.

References (Cont'd)

14. S. L. Borison. Bistatic Scattering Cross Section of a Randomly-Oriented Dipole. IEEE Trans. AP-15, 320-321 (1967).
15. H. C. van de Hulst. Multiple Light Scattering. p 194. Academic Press, New York, NY 1980.
16. Reference 6, Table 12.

END

FILMED

12-85

DTIC